Two is Better Than One? Investigating the Effect of Incorporating $Re(CO)_3Cl$ Side-Chains into Pt(II) Di-ynes and Poly-ynes

Ashanul Haque,[†,#] Rayya Al-Balushi,[‡] Idris Juma Al-Busaidi,[#] Nawal K. Al-Rasbi,[#] Sumayya Al-Bahri,[#] Mohammed K. Al-Suti,[#] Muhammad S. Khan,[#,*] Osama K. Abou-Zied,[#,*] Jonathan M. Skelton[§,ǁ,*] and Paul R. Raithby[§,*]

[†] Department of Chemistry, College of Science, University of Hail, Ha'il 81451, Kingdom of Saudi Arabia.

[‡] Department of Basic Sciences, College of Applied and Health Sciences, A'Sharqiyah University, Ibra 400, Sultanate of Oman.

[#] Department of Chemistry, Sultan Qaboos University, P.O. Box 36, Al Khod 123, Sultanate of Oman.

[§] Department of Chemistry, University of Bath, Claverton Down, Bath BA2 7AY, UK.

[ǁ] Department of Chemistry, University of Manchester, Oxford Road, Manchester M13 9PL, UK.

Abstract

Pt(II) di-ynes and poly-ynes incorporating 5,5'- and 6,6'-disubstituted 2,2'-bipyridines were prepared following conventional Sonogashira and Hagihara dehydrohalogenation reaction protocols. Using Pt(II) dimers and polymers as a rigid-rod backbone, four new hetero-bimetallic compounds incorporating $Re(CO)_3Cl$ as a pendant functionality in the 2,2'-bipyridine core were obtained. The new hetero-bimetallic Pt-Re compounds were characterized by analytical and spectroscopic techniques. The solid state structures of a Re(I)-coordinated diterminal alkynyl ligand and a representative model compound were determined by single-crystal X-ray diffraction. Detailed photo-physical characterization of the hetero-bimetallic Pt(II) di-ynes and poly-ynes was carried out. We find that the incorporation of the $Re(CO)_3Cl$ pendant functionality in the 2,2'-bipyridine-containing main-chain Pt(II) di-ynes and poly-ynes has a synergistic effect on the optical properties, red shifting the absorption profile and introducing strong long-wavelength absorptions. The Re(I) moiety also introduces strong emission into the monomeric Pt(II) di-yne compounds, whereas this is suppressed in the poly-ynes. The extent of the synergy depends on the topology of the ligands. Computational modelling was performed to compare the energetic stabilities of the positional isomers and to understand the microscopic nature of the major optical transitions. We find that 5,5'-disubstituted 2,2'-bipyridine systems are better candidates in terms of yield, photophysical properties and stability than their 6,6'-substituted counterparts. Overall, this work provides an additional synthetic route to control the photo-physical properties of metalla-ynes for a variety of optoelectronic applications.

Keywords: 2,2'-bipyridine hetero-bimetallic di-ynes and poly-ynes, photophysical properties, computational modelling

Introduction

Poly-ynes and poly(metalla-ynes) are widely studied materials with a diverse range of uses.[1] Enormous progress has been made in understanding the chemistry and photo-physical properties of these materials, leading to a number of applications.[2-7] It is now well established that "rigid-rod" metallated systems offer improved properties and performance over their organic counterparts.[1, 7, 8] The inclusion of a transition metal ion such as Cr(III), Mo(II), W(III), Mn(I), Fe(II), Ru(II), Co(III), Rh(III), Ni(II), Pd(II), Pt(II), Au(I), *etc*. into the organic backbone through σ-linkages drastically modulates and often improves the structural, photophysical, and redox properties.[1, 4] Insertion of a heavy metal ion into an organic backbone assists in bypassing spin-forbidden electronic transitions *via* intersystem crossing, leading to a substantial increase in the population of the emissive states and improved luminescence.[9] Based on this concept, several successful attempts have been made to combine the semiconducting properties of conjugated poly-ynes with the electronic effects induced by the presence of the heavy metal.[4, 10-13] Many of these metalla-ynes have proven to be good candidates for applications in the areas of photovoltaics[14], light-emitting diodes,[15] magnetic materials,[4] catalysts,[16] non-linear optical materials,[17] molecular electronics,[1] bio-imaging,[18] and the capture of organic and inorganic pollutants,[1] among others.

It is now well established that the optical properties of the poly(metalla-ynes) can be tuned by informed selection of the metals, spacers, and auxiliary ligands.[1, 19] Several strategies are available to improve the properties of metalla-ynes, such as introducing donor-acceptor (D-A) ligands, increasing the effective conjugation length, changing the position of ligand attachment, shielding the polymer backbone, forming supramolecular assemblies, *etc*.[1] We recently demonstrated that Pt(II) di-ynes and poly-ynes bearing 2,7- and 3-6-carbazole spacers have differing levels of conjugation and frontier orbitals, leading to substantial variation in optical properties.[20] We have also shown that the topology around the metal centers has an impact on the isomerization of photoactive cores such as azobenzenes.[21]

An additional and promising strategy to optimise the optoelectronic properties is to incorporate a second (hetero) metal ion into the main backbone or as a side-chain.[22-25] The introduction of a second metal into a metalla-yne induces donor-acceptor interactions and influences the energy levels of the frontier orbitals[26] and hence the absorption/emission wavelength,[27] conductivity,[28] and redox behavior.[24, 25] In particular, introduction of an ion such as Re(I) facilitates the movement of charges, narrows the band gap E_g and produces long-lived luminescence.[29] It is reported that Re(I)-2,2'-diimine complexes show environment-sensitive metal-to-ligand charge-transfer (MLCT) excited states, which can be exploited to develop luminescent and redox-active materials.[29] Wong and co-workers[24] found that the incorporation of Re(I) as a pendant side-chain into a bithiazole-containing poly(platina-yne) significantly modified the photophysical properties of the polymer. Such Pt(II)-Re(I) hetero-bimetallic systems are unique in allowing the effects of two different metal ions to be synergistically combined, potentially leading to new and useful physical properties.

Prompted by the exemplary features of Pt(II) di-ynes and poly-ynes and the interesting luminescence properties of the Re(I) fragment, we have synthesised and characterized two Re(I)-

coordinated diterminal alkynyl ligands, *viz.* $(CO)_3ClRe(I)$-5,5'-bis(ethynyl)-2,2'-bipyridine (**1c**) and $(CO)_3ClRe(I)$-6,6'-bis(ethynyl)-2,2'-bipyridine (**2c**), together with the corresponding Pt(II) di-ynes **M3**/**M4** and poly-ynes **P3/P4**. Based on structural characterisation, photophysical measurements and computational modelling, we show how the incorporation of Re(I) influences the optical properties of the systems and thereby provides an additional dimension for modifying the properties of these conjugated metallo-polymers.

Results and Discussion

Synthesis and Spectroscopic Characterization

A modified Pd(II)/Cu(I)-catalysed cross-coupling reaction between 5,5'- and 6,6'-dibromo-2,2'-bipyridine (**Scheme 1**) and ethynyltrimethylsilane (TMSA) was performed in $^{i}Pr_2NH$/THF to obtain 5,5'-bis(trimethylsilylethynyl)-2,2'-bipyridine **1a** and 6,6'-bis(trimethylsilylethynyl)-2,2'-bipyridine **2a** (**Scheme 1**).[15] The diterminal alkynes 5,5'-bis(ethynyl)-2,2'-bipyridine **1b** and 6,6'-bis(ethynyl)-2,2'-bipyridine **2b** were then obtained by removal of the trimethylsilyl protecting groups with aqueous KOH in MeOH/THF. The diterminal alkynes were purified by silica gel column chromatography giving **1b** and **2b** in 60-76% yield. The protected and diterminal alkynes were fully characterized by infrared (IR) spectroscopy, multi-nuclear NMR spectroscopy and electrospray ionization (ESI) mass spectrometry.[30, 31]

The diterminal alkynes **1b** and **2b** were reacted with rhenium(I) pentacarbonyl chloride in toluene at 60 °C overnight under an argon atmosphere to obtain the $Re(CO)_3Cl$-chelated 5,5'-bis(ethynyl)-2,2'-bipyridine **1c** and 6,6'-bis(ethynyl)-2,2'-bipyridine **2c** (**Scheme 1**). After purification by alumina column chromatography, the chelated diterminal alkynyl ligands were obtained in overall 49-62% yield, and were again characterized using IR, multi-nuclear NMR and mass spectrometry. The room temperature reaction of the $Re(CO)_3Cl$-incorporated diterminal alkynyl ligands **1c** and **2c** with two equivalents of *trans*-$[Pt(PEt_3)_2(Ph)Cl]$ in $^{i}Pr_2NH/CH_2Cl_2$ under an argon atmosphere in the presence of a CuI catalyst affords the Pt(II) di-ynes *trans*-$[(Et_3P)_2(Ph)Pt\text{-}C{\equiv}C\text{-}R\text{-}C{\equiv}C\text{-}Pt(Et_3P)_2(Ph)]$, with R = $(CO)_3ClRe$-2,2'-bipyridine-5,5'-diyl (**M3**) and R = $(CO)_3ClRe$-2,2'-bipyridine-6,6'-diyl (**M4**), as yellow solids in 40-45 % yield (**Scheme 1**). Similarly, the CuI catalysed dehydrohalogenation polycondensation reaction between *trans*-$[(P^{n}Bu_3)_2PtCl_2]$ and **1c** and **2c** in a 1:1 ratio under similar reaction conditions readily affords the corresponding poly-ynes **P3**/**P4** (**Scheme 1**).

All compounds were readily soluble in CH_2Cl_2. The IR spectra of the Pt(II) diynes and poly-ynes show a single sharp $\nu_{C{\equiv}C}$ absorption around 2066-2089 cm^{-1}, consistent with a *trans* configuration of the alkynyl bridging ligands around the Pt(II) center. The carbonyl groups in the $(bipy)Re(I)(CO)_3Cl$ chromophore give rise to three clearly-resolved IR bands in the range 1853-2018 cm^{-1} in CH_2Cl_2 solution.[32] The presence of the intact Re(I) chromophore in CH_2Cl_2 solutions of the poly-ynes **P3** and **P4** was confirmed from the presence of CO stretching bands between 1897-2018 cm^{-1} and 1871-2012 cm^{-1} respectively. The Pt(II) di- and poly-ynes showed lower $\nu_{C{\equiv}C}$ frequencies than the corresponding chelated diterminal alkynyl ligands **1c** and **2c**, which we attributed to charge transfer between the metal and the 2,2'-bipyridine moiety.

The ^{1}H and ^{13}C NMR spectra of all compounds exhibit the expected signals including those from the acetylenic carbons (see **Experimental**). The ^{31}P NMR spectra of the Pt(II) di-ynes and poly-ynes confirm the *trans* arrangement of the phosphine ligands, and the ^{31}P-NMR spectra of **M3** and **M4** show larger $^{1}J_{Pt\text{-}P}$ coupling constants than the poly-ynes **P3** and **P4** by about 300 Hz.

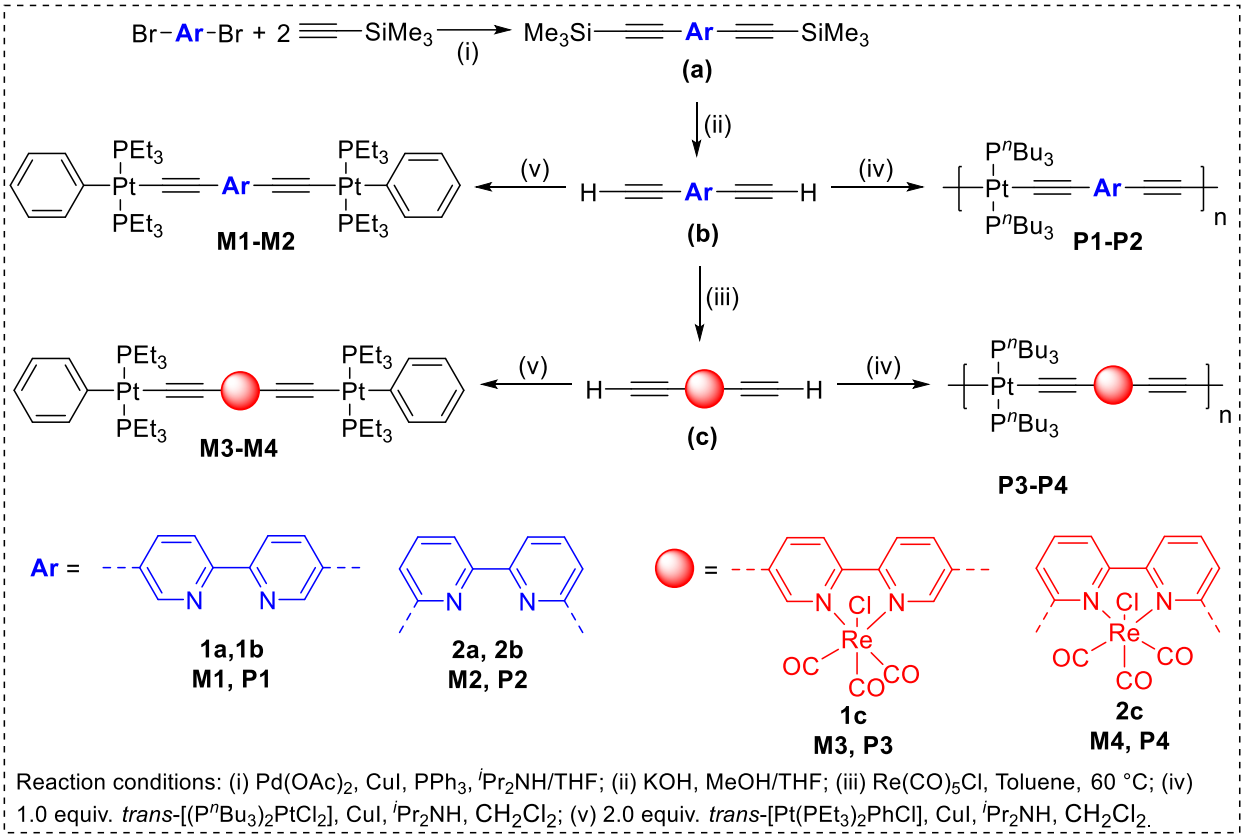

Reaction conditions: (i) $Pd(OAc)_2$, CuI, PPh_3, $^{i}Pr_2NH$/THF; (ii) KOH, MeOH/THF; (iii) $Re(CO)_5Cl$, Toluene, 60 °C; (iv) 1.0 equiv. *trans*-$[(P^{n}Bu_3)_2PtCl_2]$, CuI, $^{i}Pr_2NH$, CH_2Cl_2; (v) 2.0 equiv. *trans*-$[Pt(PEt_3)_2PhCl]$, CuI, $^{i}Pr_2NH$, CH_2Cl_2.

Scheme 1 Synthesis of the precursors **1a**-**1c**/**2a**-**2c**, the Pt(II) di-ynes **M1**-**M4** and the Pt(II) poly-ynes **P1**-**P4**.

Gel-permeation chromatography (GPC) using a polystyrene calibration gave molecular weights in the range of 90,000-100,000 g/mol for the poly-ynes **P1** and **P2**, corresponding to a degree of polymerization (DP) between 75 and 86 repeat units and a polydispersity index (PDI) between 1.3-1.7.[31] The weight-average molecular weights of **P3** and **P4** are in the range of 77,000-83,000 g/mol, corresponding to a DP between 50 and 55 and a PDI of 1.2-1.5. These molecular weights should however be treated with caution in view of the difficulties inherent in characterizing rigid-rod polymers with GPC. GPC does not give absolute molecular weights but provides a measure of the hydrodynamic volume, and rod-like polymers in solution possess very different hydrodynamic properties to more flexible systems. Calibration of the GPC with a polystyrene standard is thus likely to overestimate the molecular weights of the poly-ynes. However, the lack of discernible resonances from end groups in the NMR spectra

nonetheless points to a high degree of polymerization in these poly-ynes. ESI mass spectrometry confirmed the molecular structures of the alkynyl ligands and the dinuclear Pt(II)-Re(I) acetylide complexes.

X-ray Diffraction

To complement the spectroscopic characterization of the newly synthesized materials, we attempted to determine the crystal structure of the reported complexes by single-crystal X-ray diffraction.

Single crystals of the mononuclear Re complex **1c** were grown by slow diffusion of hexane into a solution of the complex in CH_2Cl_2. Crystallographic parameters for this structure are summarized in **Table S1**. **1c** crystallizes in the monoclinic space group $P2_1/n$. **Figure 1a** shows the molecular structure, and selected bond lengths and bond angles are given in **Table 1**. The crystal structure shows that the Re(I) centre adopts a distorted octahedral coordination environment with three carbonyl groups, a chelating bipyridine ligand and one chlorido ligand. The structure also confirms the successful attachment of the acetylene R-C≡CH groups to the bipyridine ligand. The bipyridine ligands adopt a *cis* configuration, as defined by the N atoms, with an average Re-N(Py) bond distance of 2.192(9) Å. The three carbonyl ligands are in a facial (*fac*) configuration with C-Re-C bond angles in the range of 85.3(6)-90.5(5) °, and the average Re-CO bond length is 1.90(16) Å. The Re-Cl bond is longer at 2.468(3) Å, and the Cl_1-Re-C_{15} bond angle is 174.6(4) º. These parameters are comparable to those of previously published Re(I) bipyridine systems.[33] The crystal structure consists of vertical columns of stacked complexes stabilized by C-H···Cl (2.902 Å) and C-H···O-C (2.512 Å) intermolecular interactions, with horizontal π···Cl contacts (2.877 Å) between adjacent molecules (**Figure 2a**).

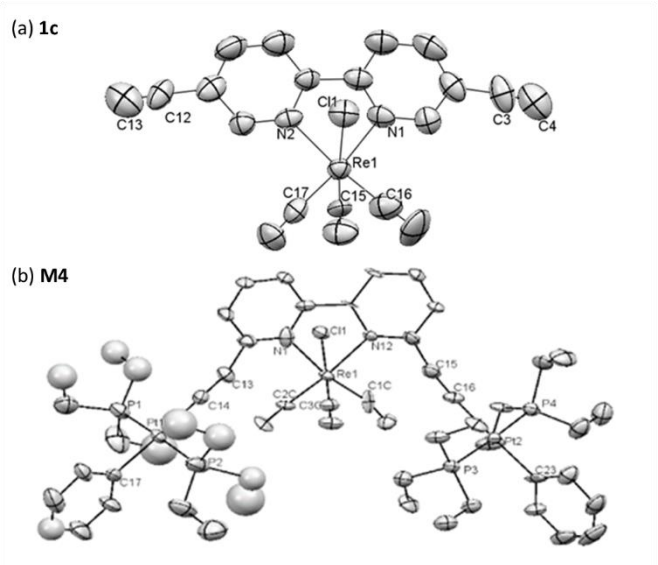

Figure 1 Crystal structures of (a) **1c** and (b) **M4** showing the atom-numbering scheme used in **Table 1**. The thermal ellipsoids are shown at 50 % probability.

Table 1 Selected bond lengths (Å) and bond angles (°) from the crystal structures of **1c** and **M4**.

Distance	[Å]	Angle	[°]
		1c	
Re(1)-C(16)	1.877(19)	C(15)-Re(1)-N(1)	90.5(4)
Re(1)-C(15)	1.908(17)	C(17)-Re(1)-N(1)	172.9(4)
Re(1)-C(17)	1.923(13)	C(16)-Re(1)-C(17)	85.3(6)
Re(1)-N(1)	2.189(8)	C(15)-Re(1)-C(17)	90.5(5)
Re(1)-N(2)	2.194(9)	C(17)-Re(1)-Cl(1)	94.9(4)
Re(1)-Cl(1)	2.468(3)	C(16)-Re(1)-N(1)	101.8(5)
		C(16)-Re(1)-N(2)	173.7(5)
		C(15)-Re(1)-N(2)	94.9(4)
		C(17)-Re(1)-N(2)	98.4(4)
		N(1)-Re(1)-N(2)	74.5(4)
		C(15)-Re(1)-Cl(1)	174.6(4)
		C(16)-Re(1)-Cl(1)	90.2(5)
		M4	
Re(1)-C(3C)	1.895(19)	C(3C)-Re(1)-C(1C)	92.7(8)
Re(1)-C(1C)	1.91(2)	C(3C)-Re(1)-C(2C)	91.2(8)
Re(1)-C(2C)	1.911(18)	C(1C)-Re(1)-C(2C)	88.9(8)
Re(1)-N(1)	2.176(17)	C(3C)-Re(1)-N(1)	92.6(7)
Re(1)-N(12)	2.204(13)	C(1C)-Re(1)-N(1)	169.8(8)
Re(1)-Cl(1)	2.514(4)	C(2C)-Re(1)-N(1)	99.7(7)
Pt(1)-C(14)	2.008(17)	C(14)-Pt(1)-C(17)	176.6(10)
Pt(1)-C(17)	2.04(4)	C(14)-Pt(1)-P(2)	88.5(6)
Pt(1)-P(2)	2.280(7)	C(17)-Pt(1)-P(2)	90.2(6)
Pt(1)-P(1)	2.293(6)	C(14)-Pt(1)-P(1)	93.3(6)
Pt(2)-C(16)	2.003(18)	P(2)-Pt(1)-P(1)	175.8(3)
Pt(2)-C(23)	2.06(2)	C(16)-Pt(2)-C(23)	177.6(8)
Pt(2)-P(4)	2.281(5)	C(16)-Pt(2)-P(4)	87.4(5)
Pt(2)-P(3)	2.292(4)	C(23)-Pt(2)-P(4)	93.0(5)

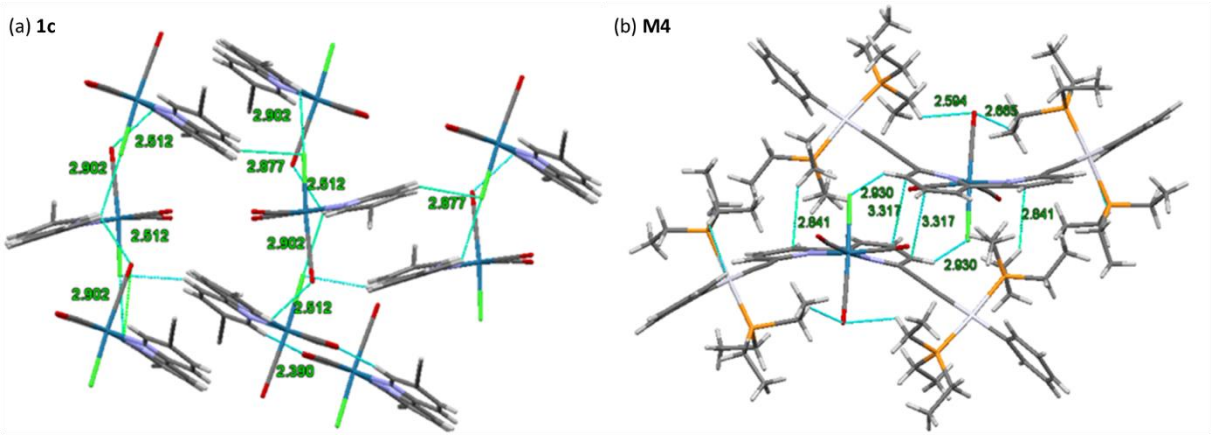

Figure 2 Crystal packing of **1c** (a), highlighting the intermolecular C-H···Cl, π···Cl and C-H···O-C interactions, and of **M4** (b), highlighting the π–π stacking and C-H···π/C-H···Cl interactions between adjacent pairs of molecules.

Attempts were also made to grow crystals of the $Re(CO)_3Cl$-incorporated model Pt(II) di-yne compounds **M3** and **M4**. Single crystals of **M4** suitable for X-ray diffraction were grown by slow diffusion of hexane to a concentrated solution of the complex in CH_2Cl_2. Crystallographic parameters for this structure are summarized in **Table S1**. Despite several attempts at doing so, we were not able to obtain crystals of **M3** that were suitable for single-crystal diffraction studies. Moreover, the crystals of **M4** were in general of poor quality and weakly diffracting, and thus while our structure is sufficient to confirm the overall molecular geometry, the bond parameters should be treated with caution.

M4 crystallizes in the triclinic space group *P*-1. The molecular structure comprises discrete trimetallic moieties defined by a central Re(2,2'-bipyridine-6,6'-diyl)$(CO)_3Cl$ unit attached to a pair of *trans*-$[(Ph)(PEt_3)_2Pt\text{-}C{\equiv}C\text{-}]$ units (**Figure 1b**). The six-coordinate Re(I) metal center adopts a distorted octahedral geometry. In general, 2,2′-bipyridine derivatives of the *fac*-$Re(CO)_3Cl$ complex adopt an almost planar geometry with respect to the basal OC-Re-CO plane.[33] However, deviation from planarity can occur due to steric hindrance between functional groups on the 2,2′-bipyridine core and the carbonyl (CO) ligands on the metal, leading to changes in the properties of the spacer group. The two rings in the bipyridine spacer are slightly twisted with respect to one another, with a torsion angle of 13 ° defined by the N(1), C(6), C(7) and N(12) atoms. This hints at a degree of strain in the bipyridine ligand, and we anticipate that the deviation from planarity would lead to some disruption of the conjugation in the ligand π system compared to a more planar geometry.

Selected bond lengths and angles from the **M4** structure are summarized in **Table 1**. The Re-CO bond distances are in the range of 1.895(19)-1.911(18) Å, the average Re-N bond distance is 2.190(15) Å and the Re-Cl bond distance is 2.514(4) Å. The N(1)-Re-N(12) bond angle is 76.4(6)°. The two Pt(II) centers adopt a distorted square planar geometry. The Pt-C≡C bond distances are 2.008(17) and 2.003(18) Å for the Pt(1) and Pt(2) centres respectively, which are consistent with related Pt(II) di-yne complexes.[31, 34] The Pt-P bond distances range from 2.280(7)- 2.293(6) Å. The C-Pt-C angle is close to linear (176.6(10) and 177.6(8) ° for Pt1 and Pt2 respectively). The presence of the Re(I) center and the *cis* configuration of the bipyridine rings of the spacer results in a Pt···Pt distance of 10.850 Å. Finally, the packing diagram of the complex (**Figure 2b**) shows a π-π stacking interaction between the pyridine rings on adjacent pairs of molecules (3.317 Å separation between ring planes), together with evidence of C-H···π and C-H···Cl interactions.

Absorption Spectroscopy

Room temperature optical absorption spectra of the bis(ethynyl)bipyridine ligands **1b** and **2b**, Re(I)$(CO)_3Cl$-chelated ligands **1c** and **2c**, and the $Re(CO)_3Cl$ incorporated Pt(II) di- and poly-ynes **M3**/**M4** and **P3/P4** were collected in 10^{-5} M CH_2Cl_2 solutions (**Figure 3**). **Table 2** compares the absorption maxima of the Pt(II) di-ynes and poly-ynes with and without the pendant Re(I) moieties, the latter taken from our previous work.[31] The absorption spectra of the ligands **1b**/**1c** and **2b**/**2c** are compared to those of the model compounds **M1**/**M2** and **M3**/**M4** in **Figure S1**.

The absorption spectra of the bis(ethynyl)-5,5'-bipyridine ligand **1b**, the $Re(CO)_3Cl$-chelated ligand **1c** and the corresponding Pt(II) di-yne **M3** and poly-yne **P3** are compared in **Figure 3a**. The spectrum of **1b** displays an intense absorption bands at λ_{max} ≈ 315 and 328 nm and a shoulder feature around 348 nm. The spectrum of **1c** displays a noticeable shift in the absorption edge relative to **1b**, with absorption bands at λ_{max} ≈ 325, 332 and 350 nm. Absorption bands at ~270 and 300-350 nm can be assigned to $\pi \rightarrow \pi^*$ transitions associated with the bipy/Ph and C≡C moieties, respectively, whereas broader bands at ~400-450 nm can be attributed to MLCT transitions.[35] This is in line with previous studies that have identified low-lying MLCT excited states involving a Re dπ donor orbital and a ligand π^* acceptor,[36, 37] with chelation to the metal serving to make the ligand a better electron acceptor and possibly also forcing it into a more planar conformation and increasing the effective conjugation in the ligand orbitals.[38] The MLCT state has been shown to be long-lived and to luminesce at longer wavelengths in the visible spectrum.[36, 37, 39] The extended tail of this ^{1}MLCT band is a signature of the extended electronic delocalization in the alkynyl bipyridine derivatives.[35] Clear effects of incorporating the Re(I) core into the Pt(II) di-yne can be seen, for example, in the extended absorption of **1c** and **M3** relative to **1b** and **M1** (**Figure 3**, **Figure S1**). The steric hindrance due to the Pt(II) fragments is expected to be higher in systems based on 6,6'-bipyridine than in the 5,5'-conunterparts, leading to different levels of conjugation. This is evidenced by the optical properties and computational modelling (*vide infra*), although ideally this should be confirmed by further structural characterization.

The Pt(II) di-yne and poly-yne systems **M3** and **P3** both display strong long-wavelength absorptions, with a broad band centered around λ_{max} ≈ 424 in **M3** and an asymmetric feature in **P3** comprising a primary peak at λ_{max} ≈ 448 nm and a secondary feature around 419 nm. Both also show weaker secondary maxima, which occur at ~339 and 343 nm in **M3** and **P3** respectively. There is thus a notable red shift in both bands and an enhancement of the extinction coefficient of the longer-wavelength bands on going from the di-yne to the poly-yne. Interestingly, calculations show that the long-wavelength transition in **M3** is not an MLCT band but is a bipyridine $\pi \rightarrow \pi^*$ transition that is highly red shifted compared to **1b**/**1c** due to a destabilised highest occupied molecular orbital (HOMO, see below). While somewhat surprising, this does account for the large enhancement of the extinction coefficient compared to the long-wavelength MLCT band in **1c**.

The spectra of the 6,6'-bis(ethynyl)bipyridine complexes in **Figure 3b** illustrate that, as for the 5,5'-functionalized systems, chelation of the ligand to $Re(CO)_3Cl$ leads to a general red shift in the absorption profile and introduces an MLCT band, again at ~410 nm. Incorporation of the chelated spacer unit into the Pt(II) di-yne and poly-yne results in a further red shift and an increase in extinction coefficient (λ_{max} ≈ 395 and 388/402 nm respectively). Comparison of the spectra of the heterometallic di-ynes and poly-ynes to the corresponding homometallic Pt(II) species (**M1**/**P1** and **M2**/**P2**) show that adding a second metal ion leads to significant changes (**Table 2**). For example, a large bathochromic shift of the lower energy bands from 398 nm in **P1** to 448 nm in **P3**, which we ascribe to stabilization of the LUMO. The 6,6'-bipyridine species generally show blue-shifted absorption maxima compared to the corresponding 5,5'-bipyridine

species, which we account for by the different positions of the alkynyl groups and the steric strain in the Pt(II) systems hindering the conjugation.

Table 2 Absorption maxima of Pt(II) di-ynes and poly-ynes with and without pendant Re(I) moieties measured at room temperature (**M1**/**M2**, **P1**/**P2** - thin films; **M3**/**M4**, **P3**/**P4** - 10^{-5} M CH_2Cl_2 solution).

Without Pendant Re(I) (Ref. [31])		With Pendant Re(I) (this Work)	
Compound	λ_{max} [nm][a]	Compound	λ_{max} [nm] (ε x 10^4 dm^3 mol^{-1} cm^{-1})
M1	269, 297, 359, 381	**M3**	339 (1.58), 424 (2.92)
M2	258, 282, 298, 334, 349	**M4**	271 (9.94), 300 (9.03), 322 (7.28), 395 (5.25)
P1	271, 295, 362, 398	**P3**	343 (1.76), 419 (3.98), 448 (6.57)
P2	233, 264, 299, 337, 352	**P4**	276 (6.97), 300 (7.50), 324 (6.15), 388 (4.94), 402 (5.21)

[a] ε was not measured in the work in Ref. [31].

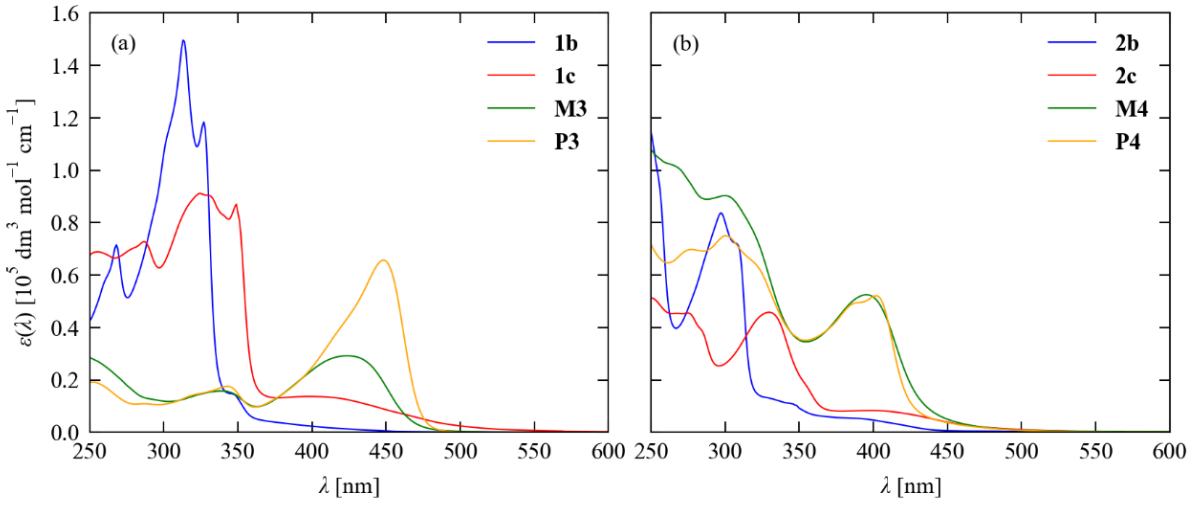

Figure 3 Comparison of the absorption spectra of the 5,5'-bis(ethynyl) bipyridine compounds **1b**, **1c**, **M3** and **P3** (a) and the 6,6'-bis(ethynyl) bipyridine compounds **2b**, **2c**, **M4** and **P4** (b). Both sets of spectra were measured in 10^{-5} M CH_2Cl_2 solutions at room temperature.

In principle, we might also expect the hindered conjugation in the 6,6'-bipyridine species to lead to lower extinction coefficients compared to the 5,5'-bipyridine analogues. While this is borne out for the **1b**/**2**b and **1c**/**2c** pairs, the **M3**/**M4** pair, and to some extent also **P3** and **P4**, show the opposite trend. As shown in **Figure 2b**, the model complex **M4** exhibits molecular stacking in the solid-state, and it is possible that aggregation in solution through a similar mechanism may alter the extinction coefficient.[40] In particular, it has been reported that "V-shaped" conjugated molecules, such as **M4**, form aggregates in halogenated solvents, leading to enhancement of the absorption cross section.[41] Measurement of the absorption spectra

of **1c**/**2c**, **M1**/**M2**, and **M3**/**M4** at solution concentrations from 1×10^{-5} to 3×10^{-5} M (**Figure S2***)* show that although the band shape and λ_{max} remain the same, the molar extinction coefficient shows some sensitivity to the concentration. This suggests that the stacking and/or C-H···π/C-H···Cl interactions visible in the X-ray structure might influence the optical properties in solution. We also measured absorption and fluorescence emission spectra at varying concentration (**Figure S2**) and found that increasing the concentration by up to 3× did not produce any major changes in spectral features, which is also in line with the results of the picosecond-nanosecond dynamics measurements presented below.

Photoluminescence Spectroscopy

Re(I) complexes are well known for their intense, unstructured emission in the orange region of the visible spectrum, which originates from ^{3}MLCT excited states.[42] The energy, the intensity and the lifetime of the emission are highly sensitive to the nature of the diimine and ancillary ligands,[43] and a large range of photoluminescence quantum yields (PLQY) have been reported for Re(I) complexes.[42] The linkage of two metal atoms to the same chromophore has been shown to increase the metal *d* character in the frontier molecular orbitals, thereby enhancing the spin-orbit coupling between the emissive triplet state and the singlet manifold.[44] Linking two heavy metals to a single heterocyclic ligand is thus an interesting potential strategy for improving the PL properties of neutral Re(I) complexes.

Room temperature emission spectra of the Re(I)-coordinated ligands **1c**/**2c**, the homometallic Pt(II) di-ynes **M1**/**M2** and the heterobimetallic Pt(II)-Re(I) di-ynes **M3**/**M4** were collected in 3 x 10^{-5} M CH_2Cl_2 solutions (**Figure 4**, **Table 3**). We also collected room-temperature solid-state emission spectra of the compounds (**Figure S3**), together with fluorescence excitation and emission spectra in CH_2Cl_2 solutions (**Figure S4**). The spectra are somewhat complex and composed of multiple maxima and/or shoulder features. The fluorescence excitation spectra of **2c**, **M1**, **M2** and **M4** are similar to the absorption spectra, providing evidence that the measured emission is from the metal complexes, whereas those of **1c** and **M3** show a significant red shift, which we tentatively ascribe to solution effects such as aggregation or ligand dissociation (**Figure S4**).

As is commonly observed in Re(I) acetylide complexes, the Re(I)-chelated bipyridine ligands **1c**/**2c** and the bimetallic di-yne model complexes **M3**/**M4** were all found to be emissive at room temperature both in solution and in the solid state. The solution spectra of all four compounds show a strong primary luminescence feature and several weaker bands at longer wavelengths. Upon excitation at 390 and 340 nm, the Pt(II) di-ynes **M1** and **M2** also show emission in solution from ~380-565 nm. The emission profiles were found to be red shifted in the solid state (**Table 3**).

At room temperature, the photo-luminescence quantum yield Φ (PLQY; **Table 3**) of **M1** and **M2** was very low and could not be reliably measured. From computational modelling studies (see below), the lowest-lying excited states of these compounds are $\pi \rightarrow \pi^*$ transitions, which are usually non-emissive at ambient temperature. On the other hand, excitation of heterobimetallic complexes **M3** and **M4** at 400 and 415 nm in solution, and 380 and 410 nm in the solid state, led to strong emission in the yellow-orange region of the spectrum as expected for diimine Re(I) tricarbonyl species. We ascribe the shorter-wavelength

emission to the reverse of the Re dπ → bipyridine π* MLCT transition as reported for other Re(I) chromophores.[29] While we were not able to assign the longer-wavelength transitions definitively, quantum-chemical calculations (see below) suggest that they may be associated with emission from formally spin-forbidden triplet states. The PLQY measured for the heterobimetallic complexes are also higher than for $Re(bpy)Cl(CO)_3$ (3.1×10^{-3} in CH_2Cl_2),[35] which indicates that the incorporation of a second metal limits non-radiative decay pathways. In general, our data indicates that incorporation of the Re(I) fragment into the heterobimetallic di-ynes improves the PLQY and leads to a red shift of emission maxima, although the emission intensity from the heterobimetallic complexes are lower than that from the homometallic Re(I) complexes at shorter wavelengths. As expected, the emission properties of the 5,5'-and 6,6'-systems differ significantly, which can be attributed to geometric constraints limiting the conjugation between the bipyridine and Pt(II) cores separated by the ethynyl units.

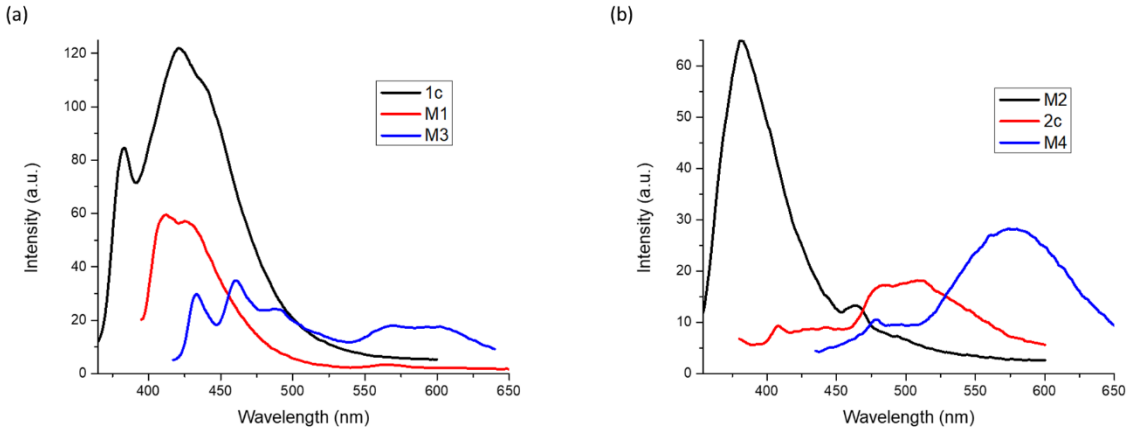

Figure 4 Room temperature emission spectra of (a) the 5,5'-bipyridine species **1c**, **M1** and **M3** and (b) the corresponding 6,6'-bipyridine species **2c**, **M2** and **M3**, measured in 3×10^{-5} M CH_2Cl_2 solutions.

Table 3 Excitation and emission wavelengths of the bis(ethynyl)bipyridine ligands **1c**/**2c** and model compounds **M1**/**M2** and **M3**/**M4** measured in 3 x 10^{-5} M CH_2Cl_2 solutions and in the solid state, together with the photoluminescence quantum yields Φ measured in solution.

	Solution (CH_2Cl_2)			Solid State	
	λ_{ex} [nm]	λ_{em} [nm]	Φ^a	λ_{ex} [nm]	λ_{em} [nm]
1c	350	382, 422	0.080	320	389, 695
2c	360	480, 514	0.13	320	388, 619
M1	390	414, 426, 565	Not detected	390	423, 561, 608
M2	340	381, 466	Not detected	340	371, 389, 693
M3	400	434, 462, 492, 568, 603	0.094	380	610, 656
M4	415	576	0.16	410	591

[a] The quantum yields are relative to coumarin 460, and the quantum yield of $Re(bpy)Cl(CO)_3$ is 0.0031 in CH_2Cl_2.[35]

In contrast to the solution spectra, the position of the band centers in the solid-state spectra of **1c** and **2c** are very similar (**Figure S3**). The emission profiles of the model compounds **M3** and **M4** are both red shifted compared to the chelated spacers, and the shift in emission wavelength of **M3** is more prominent than that of **M4**. Finally, in contrast to **M3** and **M4,** the polymers **P3** and **P4** were found to exhibit only weak emission both in solution and in the solid state at room temperature (**Figure S5**). The same was found for **P1** and **P2**.[31] The solution emission profiles of **P3** and **P4** are very similar to those of 5,5'-dibromobipyridine and 6,6'-dibromoipyridine, respectively, suggesting a dominant bipyridine-centered emission and suppression of the reverse MLCT transition seen in the chelated spacers **1c**/**2c** and the model compounds **M3**/**M4**.

Picosecond-Nanosecond Dynamics

Time-resolved fluorescence spectra of **1c**, **2c**, **M3** and **M4** in CH_2Cl_2 were measured at room temperature close to the emission maxima in **Table 3**. The transients are shown in **Figure 5** and parameters from a series of multi-exponential fits are summarized in **Table 4**. Decay transients measured over a longer observation window, in order to accurately characterise longer-lived components, are shown in **Figure S6**.

Two components with lifetimes τ = 684 ps and 2.43 ns were obtained for **1c**. The shorter-lived component can be assigned to the relaxation of the MLCT state, whereas the nanosecond lifetime of the other component is typical of $\pi \leftarrow \pi^*$ decay and can thus be ascribed to the bipyridine ligand. In **2c**, the 6,6' substitution pattern reduces the lifetime of the MLCT state to 597 ps compared to the 5,5'-substituted **1c** but raises the lifetime of the π^* decay to 2.74 ns and introduces a new, long-lived state with a lifetime of 20-23 ns. The latter are indicative of improved conjugation increasing the local heterogeneity of the system.

The presence of the Pt(II) fragments in **M3** further reduces the lifetime of the MLCT state to 200 ps but slightly increases the π^* lifetime to 3.14 ns. This can be accounted for through increased stability of the π^* state due to the more extended conjugation in the planar structure. **M3** also exhibits a very small contribution from the longer-lived component (20-23 ns) seen in **2c**. In **M4**, the steric effects due to the Pt(II) fragments in the 6,6' positions lead to an increased contribution from the long-lived state (20-23 ns) at the expense of the MLCT state, as indicated by the fitting weights in **Table 4**. These effects also increase the π^* lifetime to 5.66 ns.

Increasing the concentration of the four species from 1×10^{-5} to 3×10^{-5} M did not produce any notable changes to the measured fluorescence decay transients (**Figure S7**). This indicates that increasing the concentration does not lead to excimer formation, as this would typically cause a buildup of signal (rise time) in the transients similar to that found in other systems such as pyrenes.[45] The increase in concentration may however still lead to aggregation in the ground state, which explains the increase in the extinction coefficient observed in the absorption spectroscopy measurements.

Table 4 Parameters for the fits in **Figure 5** listing the excited state lifetime components τ_n (n = 2-3) and their corresponding contributions α_n to the overall decay transients.

	λ_{ex} [nm]	λ_{det} [nm]	τ_1 [ps]	α_1	τ_2 [ns]	α_2	τ_3 [ns]	α_3
1c	350	420	684 ± 51	0.75	2.43 ± 0.09	0.25		
2c	350	500	597 ± 55	0.61	2.74 ± 0.16	0.34	20–23*	0.05
M3	380	580	200 ± 30	0.79	3.14 ± 0.22	0.20	20–23*	0.01
M4	380	580	359 ± 51	0.38	5.66 ± 0.38	0.21	22.2 ± 0.7	0.41

* Large uncertainty due to small contribution.

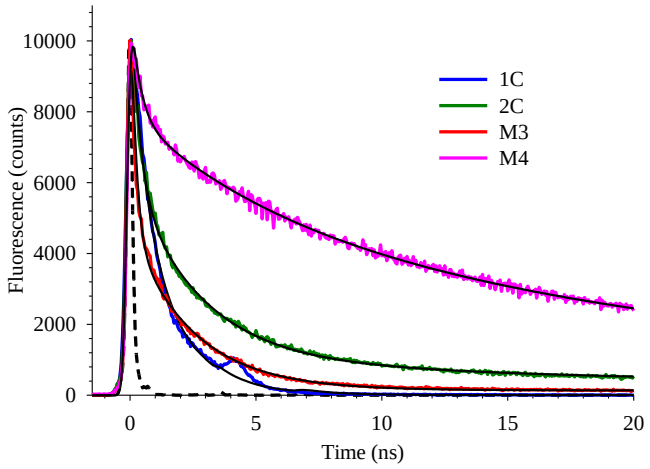

Figure 5 Room temperature fluorescence decay transients of **1c**/**2c** and **M3**/**M4** in CH_2Cl_2 (1×10^{-5} M). The instrument response function (IRF) is shown as a dashed black line. The black solid lines show fits of the measured transients to multi-exponential functions. The excitation and detection wavelengths and the fit parameters are given in **Table 4**. Note that the artefact at ~4 ns in the **1c** decay transient is due to "afterpulsing" in the photomultiplier tube detector and is excluded from the fitting, so does not affect the values reported in **Table 4**.

Computational Modelling

To better understand the changes in optical properties on chelating the bipyridine units to the Re(I) centres and subsequently incorporating the chelated spacers into the Pt(II) model complexes, we carried out molecular quantum-chemical calculations using density-functional theory (DFT) on the bipyridine-based diterminal alkynyl ligands **1b** and **2b**, chelated diterminal alkynyl ligands **1c** and **2c**, and the Pt(II) di-ynes **M3** and **M4**. To match the conditions of the solution measurements as closely as possible, the calculations were performed with an implicit solvent of CH_2Cl_2.

Images of the optimised structures are given in **Figures S8-S13** and the Cartesian coordinates are provided in **Listings S1**-**S6**. For all three pairs, we found that the 5,5'-bis(acetylide) bipyridine compounds were more energetically favourable (in CH_2Cl_2) than the 6,6'- analogues, with **1b**, **1c** and **M3** calculated to be 7.44, 30.3 and 7.97 kJ mol^{-1} lower in energy than the corresponding **2b**, **2c** and **M4** compounds, respectively.

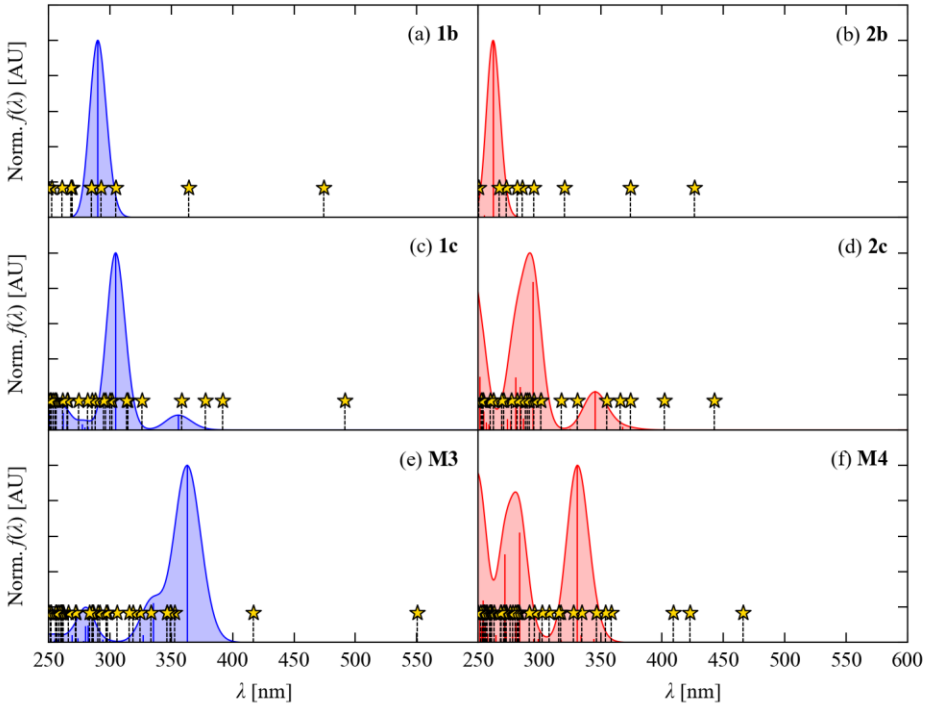

Figure 6 Simulated optical absorption spectra of the bis(ethynyl) bipyridine ligands **1b** and **2b** (a, b), $Re(CO)_3Cl$-chelated ligands **1c** and **2c** (c, d) and Pt(II) di-ynes **M3** and **M4** (e, f) obtained from time-dependent density-functional theory (TD-DFT) with an implicit CH_2Cl_2 solvent. In each subplot, the simulated spectra (blue/red shaded regions) are generated from the singlet (spin-allowed) excitations as a sum of Gaussian functions with a nominal linewidth σ of 0.1 eV. The wavelengths and relative oscillator strengths of individual transitions are marked by solid vertical lines of the same colour as the spectrum. The wavelengths of triplet (forbidden) transitions are shown as dashed vertical lines and gold stars.

Table 5 Transition wavelengths λ, oscillator strengths f and assignments of the brightest singlet (spin-allowed) transitions in the bipyridine spacers **1b**/**2b**, $Re(CO)_3Cl$-chelated bipyridine spacers **1c**/**2c** and model Pt-incorporated di-yne compounds **M3**/**M4**.

λ [nm]	f	Assignment	λ [nm]	f	Assignment
1b			**2b**		
290	1.294	$\pi \rightarrow \pi^*$	262	0.566	$\pi \rightarrow \pi^*$
1c			**2c**		
355	0.078	MLCT	345	0.066	MLCT
305	0.937	$\pi \rightarrow \pi^*$	295	0.256	Dominant $\pi \rightarrow \pi^*$
			284	0.073	Dominant MLCT
			280	0.090	Dominant MLCT
M3			**M4**		
363	1.635	$\pi \rightarrow \pi^*$ + MLCT (Pt)	331	0.595	$\pi \rightarrow \pi^*$ + MLCT (Pt)
335	0.356	MLCT (Re)	284	0.368	Mixed
327	0.063	MLCT (Re)	281	0.063	Mixed

Table 6 Transition wavelengths λ and assignments of the low-lying triplet (spin-forbidden) transitions in the bipyridine spacers **1b**/**2b**, $Re(CO)_3Cl$-chelated bipyridine spacers **1c**/**2c** and model Pt-incorporated di-yne compounds **M3**/**M4**.

λ [nm]	Assignment	λ [nm]	Assignment
1b		**2b**	
474	$\pi \rightarrow \pi^*$	426	$\pi \rightarrow \pi^*$
364	$\pi \rightarrow \pi^*$	374	$\pi \rightarrow \pi^*$
305	$\pi \rightarrow \pi^*$	320	$\pi \rightarrow \pi^*$
1c		**2c**	
492	$\pi \rightarrow \pi^*$	443	Mixed
391	Dominant MLCT	402	Mixed
377	MLCT	374	Dominant MLCT
M3		**M4**	
550	$\pi \rightarrow \pi^*$	466	Dominant $\pi \rightarrow \pi^*$
417	$\pi \rightarrow \pi^*$	423	Dominant $\pi \rightarrow \pi^*$
		409	$\pi \rightarrow \pi^*$

Simulated optical absorption spectra obtained using time-dependent DFT (TD-DFT; **Figure 6**) reproduce the key trends in the measured spectra in **Figure 3**. For both bipyridine ligands, the calculations predict a red shift in the absorption profile and the appearance of new longer-wavelength absorption bands upon chelation with $Re(CO)_3Cl$, followed by a further red shift and enhancement of the oscillator strengths of the long-wavelength bands on incorporation of the chelated spacer units into Pt(II) di-ynes. Bearing in mind the use of a uniform linewidth when simulating the spectra and the fact that we only calculated the lowest-lying excited states of the larger complexes, the positions and intensities of the bands in the simulated spectra are a reasonable qualitative match to the measured absorption profiles.

The calculations also predict that all six compounds possess low-lying triplet (spin-forbidden) excited states 100-150 nm below the onset of the absorption from the lowest-energy singlet states (marked by stars and dashed lines in **Figure 6**). The density of these triplet states generally increases on going from the spacer ligands **1b**/**2b** to the chelated spacers **1c**/**2c** to the model compounds **M3**/**M4**. As noted in the previous section, these states may be associated with the weaker long-wavelength features in the solution emission spectra in **Figure 4**. Although it is in principle possible to model emission processes using TD-DFT, the procedure is considerably more involved than calculating the transition wavelengths and oscillator strengths to model absorption spectra, and we do not consider it feasible to do so for the six compounds being examined in this work.

The brightest singlet (spin-allowed) transitions and the 2-3 lowest-lying triplet (spin-forbidden) transitions in the simulated spectra in **Figure 6** were analysed by inspecting the molecular orbitals involved and, for transitions comprising more than one significant excitation between occupied and virtual states, by using the method of natural transition orbitals (NTOs) to visualise the composite occupied "particle" and unoccupied "hole" states.[41] **Table 5** lists the calculated wavelengths, oscillator strengths and our assignments of the brightest singlet (spin-allowed) transitions in each of the six complexes, while **Table 6** lists the wavelengths and the assignments of the low-lying triplet (spin-forbidden) states. A full breakdown

of the states listed in **Tables 5** and **6** into transitions between pairs of occupied and virtual orbitals, and isosurfaces showing the NTOs, are given in **Tables S2**-**S13** and **Figures S14**-**S27**/**S31-S47** respectively.

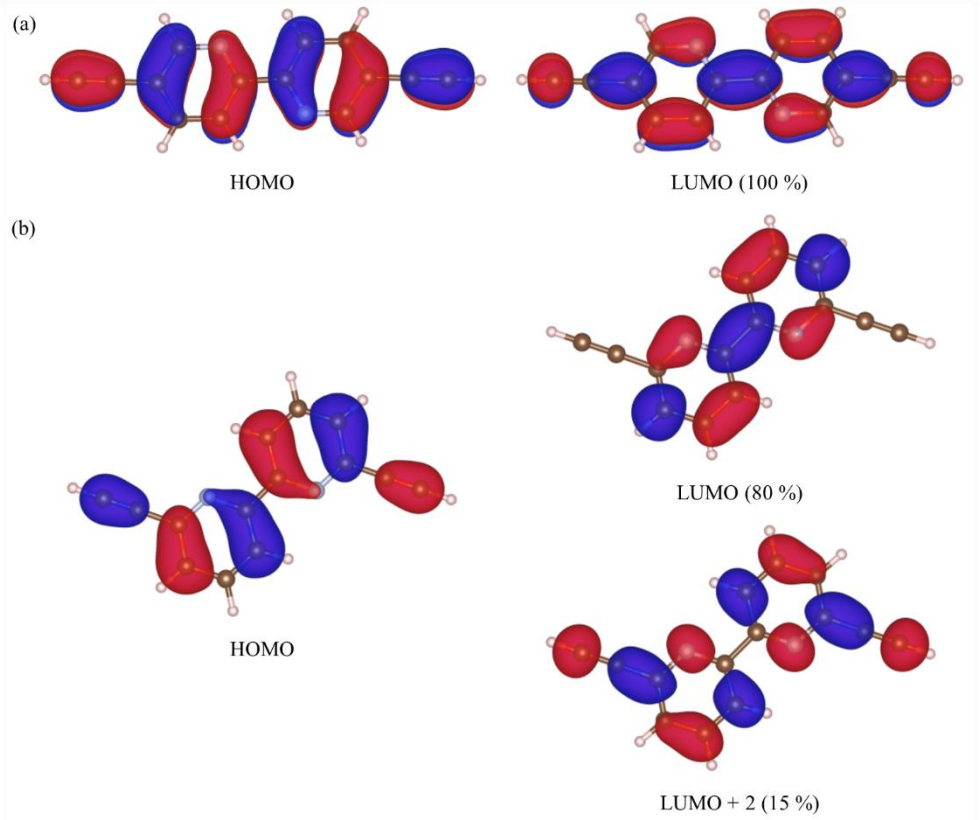

Figure 7 (a) Images of the highest-occupied and lowest-unoccupied molecular orbitals (HOMO/LUMO) in **1b**, which account for the bright $\pi \rightarrow \pi^*$ electronic excitation. (b) Images of the HOMO, LUMO and LUMO + 2 orbital in **2b** with the percentage contribution of the latter virtual orbitals to the electronic transition as marked. The isosurfaces are drawn to a contour value of 2.5×10^{-2} *e* bohr^{-3}.

A comparison of the oscillator strengths of the spin-allowed transitions in the 5,5'-bis(acetylide) bipyridine compounds to those of the 6,6'-bipyridine analogues shows that the latter are in general significantly weaker. The simulated spectrum of the (bisethynyl)bipyridine ligand **1b** (**Figure 6a**) shows a single prominent peak at 290 nm corresponding to the $\pi \rightarrow \pi^*$ electronic transition between the highest-occupied and lowest-unoccupied molecular orbitals (HOMO/LUMO; **Figure 7a**). The lowest-energy transition in the 6,6'-bis(ethynyl)bipyridine analogue **2b** occurs at a shorter wavelength of 262 nm and a has a much lower oscillator strength of $f = 0.57$ vs. 1.29 (**Figure 6b**). As in **1b**, the major component of the transition is the HOMO → LUMO excitation, but there is a substantial minor component associated with the HOMO → LUMO + 2 excitation (**Figure 7b**). Comparison of the LUMOs of **1b** and **2b** shows that the different substitution pattern in **2b** lowers the degree of conjugation in the LUMO, and comparison of the orbital energies in **1b** and **2b** (**Figure S28**) indicates that the higher energy (shorter wavelength) transition in **2b**

is most likely due to destabilisation of the LUMO. The lower degree of conjugation also leads to poorer spatial overlap with the HOMO, which explains the mixing of the LUMO + 2 orbital into the $\pi \rightarrow \pi^*$ excited state. This would further raise the transition energy, and the poorer spatial overlap between the HOMO and LUMO may explain the lower oscillator strength of the transition compared to the 5,5'-bipyridine analogue **1b**.

Chelation of **1b** results in new frontier Re-based orbitals, of which the HOMO - 1 orbital has the best spatial overlap with the bipyridine-based LUMO and gives rise to a weak MLCT band at 355 nm (**Figure 6c**). The HOMO - 3 orbital remains similar in form to the HOMO in **1b**, and the much stronger $\pi \rightarrow \pi^*$ transition occurs at 305 nm. The particle and hole states obtained from the NTO analysis of the two transitions are shown in **Figure 8**. The spectrum of **2c** also shows a weak MLCT band with a comparable, if slightly lower, oscillator strength, which again occurs between a Re-based HOMO - 1 and the bipyridine ligand-based LUMO (**Figure 6d**, **Figure S18**). As for **1b**/**2b**, this transition is blue shifted compared to that in **1c** due to the higher-energy LUMO (**Figure S29**). The strong shorter-wavelength feature in **Figure 6d** is a combination of three bands at 295, 284 and 280 nm. The longer-wavelength band at 295 nm was assigned as predominantly a $\pi \rightarrow \pi^*$ transition based on the NTOs but with some MLCT character (**Figure S19**), the latter of which may explain its ~3× smaller oscillator strength than the corresponding $\pi \rightarrow \pi^*$ transition in **1c**, relative to the smaller ~2× difference in oscillator strengths of the electronic transitions in **1b**/**2b** (c.f. **Table 5**). This reduction in oscillator strength can also be seen in the measured spectra in **Figure 3**. The two higher-energy transitions at 284 and 280 nm were assigned as predominantly MLCT, which is consistent with their weak oscillator strengths (**Figures S20**/**S21**).

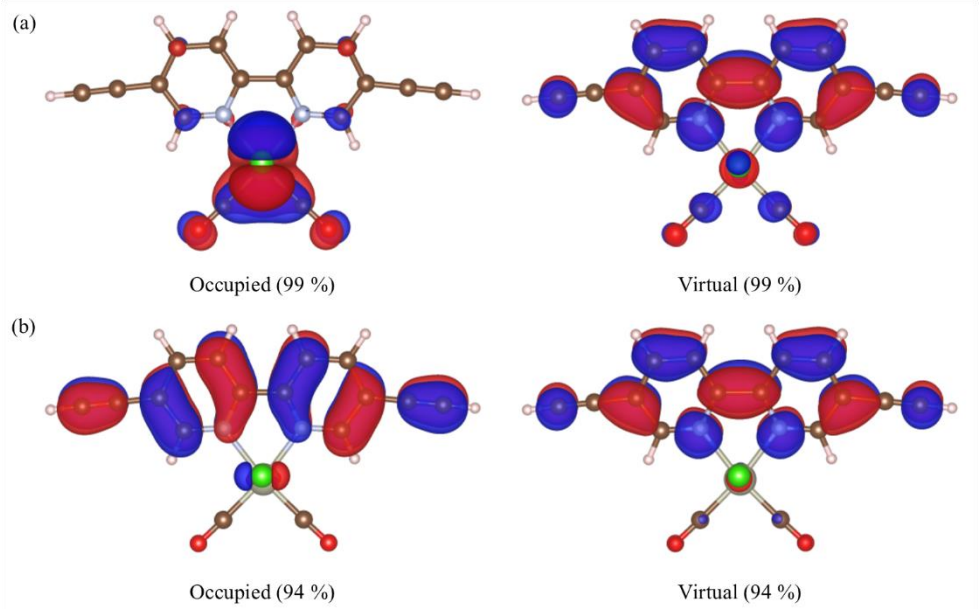

Figure 8 Occupied particle and virtual hole states obtained from natural transition orbitals (NTOs) analyses[46] of the dominant optical absorptions of **1c** at 355 (a) and 305 nm (b) identified in **Figure 6**/**Table 5**. The isosurfaces are drawn to a contour value of 2.5 × 10^{-2} *e* $bohr^{-3}$.

The simulated spectrum of **M3** (**Figure 6e**) shows a major peak comprising a single bright state at 363 nm and a shoulder feature composed of two transitions at 335 and 327 nm. The long-wavelength transition mostly comprises a HOMO → LUMO excitation and was assigned as a $\pi \rightarrow \pi^*$ with some MLCT character from participation of the Pt d orbitals in the HOMO (**Figure 9a**). The ligand-based HOMO is therefore destabilised and raised above the equivalent Re-based orbitals that form the HOMO in **1c**. The extended conjugation in the HOMO due to incorporation into the di-yne may also explain the enhanced oscillator strength of the transition relative to **1b** and **1c**. The two shoulder features can both be assigned, based on the NTOs, as MLCT transitions from the Re moiety (**Figure 9b**, **Figures S23/24**). The two prominent peaks in the spectrum of **M4** (**Figure 6f**) arise from three transitions at 331, 284 and 281 nm which, as for **M3**, can again be assigned as a long-wavelength $\pi \rightarrow \pi^*$ and two shorter-wavelength MLCT bands (**Figures S25-27**). All three are blue-shifted with respect to the corresponding transitions in **M3**, which can be ascribed to the destabilisation of the LUMO as seen in the **1b**/**2b** and **1c**/**2c** pairs (**Figures S28-S30**).

The low-lying triplet states in **1b** and **2b** were assigned based on the NTOs as $\pi \rightarrow \pi^*$ excitations (**Table 6**; **Figures S31**-**S36**). The lowest-lying triplet excitation in **1c** is predicted to occur at 492 nm and was also characterised as a $\pi \rightarrow \pi^*$ (**Figure S37**), whereas the next-highest triplet excitations at 391 and 377 nm are primarily MLCT bands (**Figures S38**/**S39**). In **2c**, on the other hand, the lowest-lying triplet states at 443 and 402 nm are of mixed MLCT and $\pi \rightarrow \pi^*$ character (**Figures S40**/**S41**), while the higher-lying state at 374 nm is predominantly an MLCT excitation (**Figure S42**). The simulated spectrum of **M3** in **Figure 6e** shows two triplet states below the bright, long-wavelength singlet excitation, which were both characterised as a $\pi \rightarrow \pi^*$ transitions (**Figures S43**/**S44**). In **M4**, there are three triplet states at notably longer wavelengths than the absorption onset, and these were again characterised as $\pi \rightarrow \pi^*$ transitions (**Figures S45**-**S47**). The change in the nature of the triplet states on going from the chelated spacers to the heterobimetallic di-ynes is consistent with the shortening of the MLCT state lifetime and lengthening of the π^* lifetime observed in the picosecond-nanosecond dynamics measurements (c.f. **Table 4**). The mixed character of the triplet states in the 6,6'-bipyridine species may also explain the larger contribution of the longer-lived $\pi \rightarrow \pi^*$ states to the transients in **Figure 5**.

In summary, for the 5,5'-bipyridine series these electronic-structure calculations show that chelation of the bipyridine spacer ligand **1b** with $Re(CO)_3Cl$ in **1c** leads to a red shift of the optically-bright $\pi \rightarrow \pi^*$ electronic transition in **1b** and introduces a weaker low-lying MLCT band. Subsequent incorporation of the chelated bipyridine into the Pt(II) di-yne **M3** destabilises the highest-lying bipyridine-based π orbital, red shifts the $\pi \rightarrow \pi^*$ transition to lower energy than the Re-bipyridine MLCT state in **1c** and enhances its oscillator strength, and also red-shifts and enhances the MLCT state in the chelated spacer precursor. The destabilisation of the HOMO and red shift of the $\pi \rightarrow \pi^*$ transition represents an interesting effect of incorporating the spacer into the di-yne. The higher energy and lower oscillator strength of the $\pi \rightarrow \pi^*$ transition in the 6,6'-bipyridine ligand **2b** can be ascribed to destabilisation of the LUMO and poorer spatial overlap with the HOMO resulting in higher-energy virtual orbitals being involved in the transition. This

highlights the sensitivity of the optical properties to the topology of the bipyridine spacer group, as observed in the absorption and emission measurements. As for **1b**, chelation of **2b** with $Re(CO)_3Cl$ introduces a weak low-lying MLCT band but also introduces some MLCT character into the higher-energy $\pi \rightarrow \pi^*$ transition, which may again serve to reduce its oscillator strength. The Pt(II) di-yne **M4** shows similar spectral features to **M3**, with the destabilisation of the bipyridine-based LUMO in the former resulting in a general predicted blue shift of the electronic transitions. Finally, analysis of the spin-forbidden triplet excitations also shows that the spacer topology, the chelation of the spacer with Re(I) and the incorporation of the chelated spacers into Pt(II) di-ynes has a substantial effect on the nature of the emissive states.

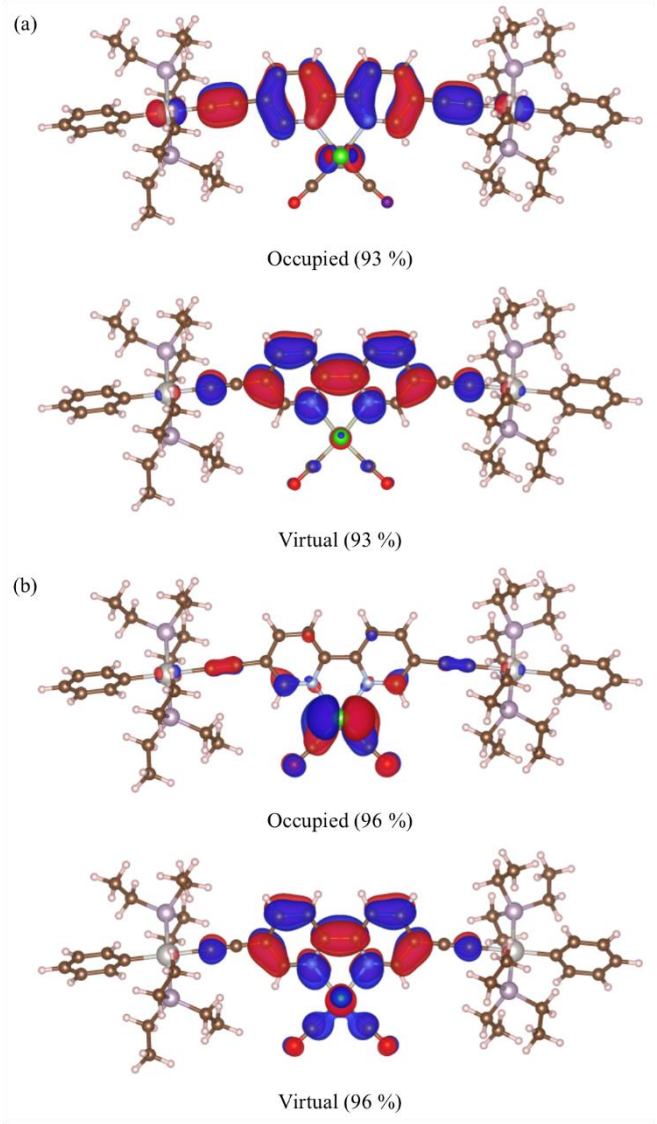

Figure 9 Occupied particle and virtual hole states obtained from natural transition orbitals (NTO) analyses[46] of the optical absorptions of **M3** at 363 (a) and 335 nm (b) identified in **Figure 6/Table 5**. The NTOs associated with the second MLCT transition at 327 nm are substantially similar to those in (b) and are therefore not shown (c.f. **Figure S24**). The isosurfaces are drawn to a contour value of 2.5×10^{-2} *e* $bohr^{-3}$.

Conclusions

We have synthesized and characterized two Re(I)-coordinated diterminal alkynyl ligands, *viz.* $Re(CO)_3Cl$-5,5'-diethynyl-2,2'-bipyridine and $Re(CO)_3Cl$-6,6'-diethynyl-2,2'-bipyridine, which we have subsequently incorporated as spacer groups into Pt(II) di-ynes and poly-ynes. Structural characterization of a Pt(II) di-yne model complex reveals π stacking and a variety of weak intermolecular/interchain interactions in the solid state. As evidenced by optical absorption and emission spectroscopy and computational modelling, the photophysical properties of the Pt(II) di-ynes and poly-ynes show a high sensitivity to the topology of the bipyridine spacer group. Optical spectroscopy shows that chelation of the bipyridine ligands produces a red shift in the $\pi \rightarrow \pi^*$ transition and introduces weak, long-wavelength MLCT bands, both of which are further red-shifted in the Pt(II) di-ynes and poly-ynes. The metallated species appear to show aggregation in solution, leading to substantial enhancement of the extinction coefficient with concentration. Emission spectroscopy reveals prominent blue/green emission associated with the Re(I) chromophore in the chelated bipyridines and Pt(II) di-ynes, whereas the Pt(II) poly-ynes only show shorter-wavelength bipyridine-centered emission. Picosecond-nanosecond dynamics measurements identify short-lived MLCT excited states and 1-2 long-lived π^* states in the chelated spacers, and incorporation of the spacers into the model Pt(II) di-ynes suppresses the MLCT state and significantly shortens its lifetime. Computational modelling confirmed the higher energetic stability of the 5,5'-bipyridine species compared to the 6,6'-bipyrdine analogues and allowed us to establish the nature of the brightest electronic transitions and low-lying triplet states in the optical absorption spectra. These calculations also reveal a remarkable destabilisation of the bipyridine-based π orbital in the model di-ynes due to interaction with the Pt d orbitals, which results in the optically bright $\pi \rightarrow \pi^*$ transitions being lowered in energy compared to the long-wavelength Re $d\pi \rightarrow \pi^*$ MLCT transition in the chelated spacer precursors. In summary, our systematic studies have elucidated the effect of introducing a second metal ion into rigid-rod Pt(II) poly-ynes by chelation of the main-chain spacer groups, and thus highlighted the potential utility of this strategy for fine-tuning the optoelectronic properties of these materials for future technological applications.

Experimental Section

General Procedures

All reactions were performed in a dry argon atmosphere using standard Schlenk techniques. Solvents were distilled and pre-dried before being used according to standard procedures.[42] Unless stated otherwise, all chemicals were obtained from Sigma Aldrich and used without further purification. *trans*-$[Pt(Ph)Cl(PEt_3)_2]$ and *trans*-$[(P^nBu_3)_2PtCl_2]$ were prepared following reported procedures.[43,44] Column chromatography was performed using either Kieselgel 60 (70-230) silica gel or Brockman Grade II-III alumina. NMR spectra were recorded on Bruker MM-250 and WM-400 spectrometers in $CDCl_3$. ^1H and ^{13}C NMR spectra were referenced to solvent resonances and ^{31}P NMR spectra were referenced to an external

phosphoric acid standard (85 % H_3PO_4). Mass spectra were acquired using a Kratos MS 890 spectrometer using electrospray ionization (ESI). CH_2Cl_2 solutions of the ligand precursors, di-ynes, and poly-ynes were prepared at concentrations of 10^{-5}-10^{-4} M. IR spectra of 10^{-4} M solutions were recorded using a Cary 630 FT-IR spectrometer. Absorption spectra were recorded at solution concentrations of 1×10^{-5} - 3×10^{-5} M on a Varian-Cary 50 UV-visible spectrophotometer in a 1 cm quartz cuvette. Solution emission spectra were recorded from 10^{-5} M solutions using a Shimadzu RF-5301 PC spectrofluorophotometer. Solid-state emission spectra were recorded using a PerkinElmer LS 55 fluorescence spectrometer. Lifetime measurements were performed using the time-correlated single photon counting (TCSPC) setup described elsewhere.[47] Microanalyses were performed using a PerkinElmer 2400 Series II CHNS/O elemental analyzer. Molar masses of the Pt(II) poly-ynes were determined by gel-permeation chromatography/light-scattering (GPC/LS) analysis. GPC was carried out using two PL Gel 30 cm, 5 µm mixed C columns at 30 ^oC running in THF at 1 mL min^{-1} with a Roth Model 200 high-precision pump. This was coupled to a DAWN DSP Wyatt Technology multiangle laser light-scattering (MALLS) apparatus with 18 detectors and auxiliary Viscotek Model 200 differential refractometer/viscometers, which were used to calculate the molecular weights.

Synthesis and Characterization of precursors, dimers and polymers

The precursors (**1a-1b, 2a-2b**), dimers (**M1**-**M2**), and polymers (**P1**-**P2**) were prepared and characterized according to previously reported procedures.[30, 31]

Rhenium(I) tricarbonyl chloride-5,5'-bis(ethynyl)-2,2'-bipyridine (**1c**)

A mixture of **1b** (0.050 g, 0.24 mmol) with Rhenium(I) pentacarbonyl chloride (0.18 g, 0.50 mmol) was dissolved in toluene (20 mL). The solution was stirred at 60 °C overnight. After cooling to room temperature, the solvent was removed under reduced pressure. The mixture was purified by passing it through an alumina column using hexane/CH_2Cl_2 (1:2) as the eluent, and further purification by preparative alumina thin layer chromatography yielded **1c** as an orange solid (0.064 g, 0.13 mmol, 49% yield, decomposition temp. 250 °C). IR (CH_2Cl_2): ν/cm^{-1} 1896, 1905, 2015 (C=O), 2120 (C≡C), 3296 (C≡CH). ^{1}H NMR (250 MHz, $CDCl_3$): δ/ppm 9.11 (dd, *J* = 2.0, 0.78 Hz, 2H, $H_{6,6'}$), 8.13 (d, *J* = 7.9 Hz, 2H, $H_{3,3'}$), 8.11 (dd, *J* = 8.1, 2.0 Hz, 2H, $H_{4,4'}$), 3.50 (s, 2H, C≡C-H). ^{13}C NMR (100 MHz, $CDCl_3$): δ/ppm 155.32 ($C_{2,2'}$), 149.64 ($C_{6,6'}$), 137.75 ($C_{3,3'}$), 124.66 ($C_{4,4'}$), 119.30 ($C_{5,5'}$), 88.46, 79.90 (C≡C). ESI-MS: *m*/*z* 511 $[M + 2]^+$. Anal. calc. for $C_{17}H_8N_2O_3ClRe$: C - 38.81; H - 2.16; N - 5.28 %, found: C - 38.78; H - 2.15; N - 5.25 %.

Rhenium(I) tricarbonyl chloride-6,6'-bis(ethynyl)-2,2'-bipyridine (**2c)**

Similar procedures to those used to obtain **1c** were followed starting from **2b** (0.13 g, 0.63 mmol)**. 2c** was obtained as an orange solid after purification (0.080 g, 0.39 mmol, 62 % yield; decomposition temp. 149 °C). IR (CH_2Cl_2): ν/cm^{-1} 1853, 1907, 2017 (C=O), 2115 (C≡C), 3291 (C≡CH). ^{1}H-NMR (250 MHz $CDCl_3$): δ/ppm 8.11 (d, 2H, *J* = 7.6 Hz, $H_{3,3'}$), 7.82 (t, *J* = 7.9 Hz, 2H, $H_{4,4'}$), 7.54 (d, *J* = 7.7 Hz, 2H, $H_{5,5'}$),

3.9 (s, 2H, C≡NC-H). ^{13}C NMR (100 MHz, $CDCl_3$): δ/ppm 157.41 ($C_{2,2'}$), 146.12 ($C_{6,6'}$), 138.53 ($C_{3,3'}$), 130.71 ($C_{4,4'}$), 122.68 ($C_{5,5'}$), 89.75, 81.70 (C≡C). ESI-MS: *m*/*z* 516 $[M]^+$. Anal. calc. for $C_{17}H_8N_2O_3ClRe$: C - 38.81; H - 2.16; N - 5.28 %, found: C - 38.79; H - 2.14; N - 5.26 %.

***trans*-[(Ph)(Et$_3$P)$_2$Pt-C≡C-R-C≡C-Pt-(PEt$_3$)$_2$(Ph)] (R = (CO)$_3$ClRe(I)-2,2'-Bipyridine-5,5'-diyl)** (**M3**)

To a stirred solution of *trans*-[$(PEt_3)_2$(Ph)PtCl] (0.85 g, 0.16 mmol) and **1c** (0.40 g, 0. 78 mmol) in CH_2Cl_2/^{i}Pr$_2$NH (50 mL 1:1 v/v) under argon was added a catalytic amount (~5 mg, 0.0026 mmol) of CuI. The yellow solution was stirred at room temperature for 15 h, after which all volatile components were removed under reduced pressure. The residue was dissolved in CH_2Cl_2 and passed through a silica column eluting with hexane/CH_2Cl_2 (1:1, v/v). Removal of the solvents under vacuum gave the title complex as a yellow/orange solid (0.044 g, 0.029 mmol, 40% yield, decomposition temperature 198.5 °C). IR (CH_2Cl_2): ν/cm^{-1} 1885, 1909, 2016 (C=O), 2085 (C≡C). **^{1}**H NMR (250 MHz, $CDCl_3$): δ/ppm 8.82 (s, 2H, $H_{6,6}$), 7.76 (dd, *J* = 6.9, 1.6 Hz, 2H, $H_{3,3}$), 7.41 (s, 2H, $H_{4,4}$), 7.26 (d, *J* = 7.2, 4H, H_{ortho} Ph), 6.94 (t, *J* = 7.6 Hz, 4H, H_{meta} Ph), 6.83 (t, *J* = 7.5 Hz, 2H, H_{para} Ph), 1.75 (m, 24H, PCH_2), 1.12 (t, 36H, *J* = 6.4 Hz, P(CH_2CH_3)). ^{13}C NMR (100 MHz, $CDCl_3$): δ/ppm 150.47 ($C_{2,2}$), 144.22 ($C_{6,6}$), 138.86($C_{3,3}$), 127.1 (C Ph), 121.2 ($C_{4,4}$), 115.3 ($C_{5,5}$), 110.4 (C≡C), 15.09 (P(CH_2CH_3)), 8.05 (CH_3). ^{31}P{^{1}H} NMR (162 MHz, $CDCl_3$): δ 10.02 ($^1J_{Pt-P}$ = 2649.47 Hz). ESI-MS: *m*/*z* 1525 $[M]^+$. Anal. calc. for $C_{53}H_{76}N_2O_3P_4Pt_2ReCl$: C - 41.74; H - 5.02; N - 1.84 %, found: C - 41.23; H - 5.27; N - 1.98 %.

***trans*-[(Ph)(Et$_3$P)$_2$Pt-C≡C-R-C≡C-Pt-(PEt$_3$)$_2$(Ph)](R = (CO)$_3$ClRe-6,6'-bis(ethynyl)-2,2'-bipyridine)** (**M4**)

M4 was prepared following a similar procedure as for **M3** starting from *trans*-[$(PEt_3)_2$(Ph)PtCl] (0.079 g, 0.15 mmol) and **2c** (0.037 g, 0.073 mmol**)**. A yellow solid was obtained after purification (0.050 g, 0.033 mmol, 45%; decomposition temp. 255.5 ^{o}C). IR (CH_2Cl_2): ν/cm^{-1} 1875, 1910, 2013 (C=O), 2066 (C≡C) .**^{1}**H NMR (250 MHz, $CDCl_3$): δ/ppm 7.73 (d, *J* = 7.7 Hz, 2H, $H_{5,5}$), 7.63 (t, *J* = 7.9 Hz, 2H, $H_{3,3}$), 7.42 (dd, *J* = 7.9, 2.0 Hz, 2H, $H_{4,4}$), 7.32 (d, *J* = 7.5 Hz, 4H, H_{ortho} Ph), 7.05 (t, *J* = 7.7 Hz, 4H, H_{meta} Ph), 6.84 (t, *J* = 7.3 Hz, 2H, H_{para} Ph), 1.75 (m, 24H, PCH_2), 1.10 (m, 36H, P(CH_2CH_3). ^{13}C NMR (100 MHz, $CDCl_3$): δ/ppm 156.88 ($C_{2,2}$), 151.15 ($C_{6,6}$), 136.07 ($C_{3,3}$), 130.89-127.80 (C Ph), 121.43 ($C_{4,4}$), 117.75 ($C_{5,5}$), 112.66 (C≡C), 15.09 (PCH_2CH_3), 7.97 (CH_3). ^{31}P{^{1}H} NMR (162 MHz, $CDCl_3$): δ 9.92 ($^1J_{Pt-P}$ = 2650.25 Hz). ESI-MS: *m*/*z* 1528 $[M + 4]^+$. Anal. calc. for $C_{53}H_{76}N_2O_3P_4Pt_2ReCl$: C - 41.74; H - 5.02; N - 1.84 %, found: C - 41.89; H - 5.19; N - 1.90%.

***trans*-[(^{n}Bu$_3$P)$_2$Pt-C≡C-R-C≡C-]$_n$ (R = Re(CO)$_3$Cl-2,2'-Bipyridine-5,5'-diyl)** (**P3**)

CuI (0.015 g, .0079 mmol) was added to a mixture of *trans*-[$Pt(P^nBu_3)_2Cl_2$] (0.040 g, 0.0060 mmol) and **1c** (0.030 g, 0.0060 mmol) in ^{i}Pr$_2$NH/CH_2Cl_2 (50 mL, 1:1 v/v). The solution was stirred at room temperature for 15 h, after which all volatile components were removed under reduced pressure. The residue was dissolved in CH_2Cl_2 and purified through a short alumina column. After removal of the solvent under reduced pressure, a yellow film was obtained and then washed with methanol to give **P3** (0.0054 g,

82% yield). Further purification could be performed by precipitation from CH_2Cl_2 in MeOH. IR (CH_2Cl_2): ν/cm^{-1} 1897, 1920, 2018 (C=O), 2089 (C≡C). ^{1}H NMR (250 MHz, $CDCl_3$): δ/ppm 7.94 (d, 2H, *J* = 7.0 Hz, $H_{3,3'}$), 7.17 (t, 2H, *J* = 7.0 Hz, $H_{4,4'}$), 6.86 (d, 2H, *J* = 7.6 Hz, $H_{5,5'}$), 2.11 (m, 12H, $PCH_2(CH_2)_2(CH_3)$), 1.49 (m, 12H, $PCH_2(CH_2)_2(CH_3)$), 1.41 (m, 12H, $PCH_2(CH_2)_2(CH_3)$), 0.92 (t, *J* = 7.2 Hz, 18H, $P(CH_2)_3CH_3$)). ^{13}C NMR (100 MHz, $CDCl_3$): δ/ppm 156.72 ($C_{2,\ 2'}$), 145.28 ($C_{6,6'}$), 136.27 ($C_{3,3'}$), 126.15 ($C_{4,4'}$), 122.10 ($C_{5,5'}$), 115.98, 109.32 (C≡C), 29.72-23.18 ($PCH_2CH_2CH_2CH_3$), 14.35 (CH_3). ^{31}P{^{1}H} NMR (162 MHz, $CDCl_3$): δ/ppm 3.29 ($^1J_{Pt-P}$ = 2340.25 Hz). Anal. calc. for $(C_{41}H_{60}N_2P_2O_3ClRePt)_n$: C - 44.47; H - 5.46; N - 2.53 %, found: C - 44.61; H - 5.51; N - 2.59 %. GPC (THF): M_n = 61,000 g mol^{-1} (n = 55), M_w = 77,000 g mol^{-1}, polydispersity index = 1.26.

***trans*-[(^{n}Bu$_3$P)$_2$Pt-C≡C-R-C≡C-]$_n$ (R = Re(CO)$_3$Cl-2,2'-Bipyridine-6,6'-diyl)** (**P4**)

P4 was prepared as described above for **P3** starting from *trans*-[Pt(P^nBu_3)$_2$$Cl_2$] (0.040 g, 0.0060 mmol) and **2c** (0.030 g, .0060 mmol) in CH_2Cl_2/^{i}Pr$_2$NH (40 mL, 1:1, v/v) with catalytic CuI (0.011 g, 0.0058 mmol). After purification, the product was obtained as a bright yellow solid (0.0046g, 70% yield, decomposition temp. 256 ^{o}C). IR (CH_2Cl_2): ν/cm^{-11} 1871,1911, 2012 cm^{-1} (C=O) 2068 cm^{-1} (C≡C). ^{1}H NMR (250 MHz, $CDCl_3$): δ/ppm 8.10 (m, 2H, $H_{3,3'}$), 7.32 (t, 2H, *J* = 7.2 Hz, $H_{4,4'}$), 6.24 (d, 2H, *J* = 7.0 Hz, $H_{5,5'}$), 1.56 (m, 14H, $PCH_2(CH_2)_2(CH_3)$), 1.47-1.29 (m, 22H, $PCH_2(CH_2)_2(CH_3)$), 0.88 (t, *J* = 7.0 Hz, 18H, $P(CH_2)_3CH_3$). ^{13}C NMR (100 MHz, $CDCl_3$): δ/ppm 156.23 ($C_{2,\ 2'}$), 145.21 ($C_{6,6'}$), 136.32 ($C_{3,3'}$), 126.08 ($C_{4,4'}$), 120.79 ($C_{5,5'}$), 115.32, 112.54 (C≡C), 30.13-23.68 ($PCH_2CH_2CH_2CH_3$), 14.37 (CH_3). ^{31}P{^{1}H} NMR (162 MHz, $CDCl_3$): δ/ppm 3.32 ($^1J_{Pt-P}$ = 2339.18). Anal. calc. for $(C_{41}H_{60}N_2P_2O_3ClRePt)_n$: C - 44.47; H - 5.46; N - 2.53 %, found: C - 44.55; H - 5.50; N - 2.56 %. GPC (THF): M_n = 55,000 g mol^{-1} (n = 50), M_w = 83,000 g mol^{-1}, PDI = 1.51.

X-ray Crystallography

Single-crystal X-ray diffraction experiments were performed at 150 K on a STOE IPDS (II) diffractometer using monochromatic Mo-K_α radiation (λ = 0.71073 Å) with the sample temperature controlled using an Oxford Diffraction Cryojet. The X-Area software was used for data collection and indexing. The structure was solved and refined using full-matrix least squares on F^2 in SHELX2014[45] from the WinGX suite.[48] A multi-scan absorption correction was applied. There was extensive disorder in the alkyl groups of the phosphine ligands, which were modelled over two or three sites using partial occupancies, constrained to sum to unity, and with additional constraints placed on the bond parameters to maintain reasonable bond lengths and angles. With the exception of some of the disordered carbon atoms in the alkyl chains of the phosphine ligands, all non-hydrogen atoms were refined anisotropically. Hydrogen atoms were included using rigid methyl groups or a riding model, with partial occupancies used as appropriate. Refinement was continued until convergence, and in the final cycles of refinement a weighting scheme was used that gave a relatively flat analysis of variance.

Time-Resolved Fluorescence

Lifetime measurements were performed using time-correlated single photon counting (TCSPC). The TCSPC setup, described elsewhere,[47] is part of an ultrafast spectrometer (Halcyone, Ultrafast Systems, LLC) used to measure femtosecond fluorescence upconversion. Briefly, an excitation is obtained using a regenerative amplified Ti:Sapphire laser (Libra, Coherent), which generates compressed laser pulses centered on 800 nm with a 70 fs FWHM, 4.26 W power and a 5 kHz repetition rate. 90% of the output pulse is used to pump a Coherent OPerA Solo optical parametric amplifier (Light Conversion Ltd.) to generate spectrally tunable light from 240−2600 nm. For the current measurements, the OperA was adjusted at 350 and 380 nm (~ 20 nJ) and used as the excitation beam after passing through a depolarizer to cancel any contributions from rotational dynamics (DPU-25, Thorlabs). A photomultiplier tube with an instrument response function (IRF) of ~250 ps, measured from scattered excitation light, was used as the detector. Fluorescence was attenuated and directed to the detector, and a monochromator was used to adjust the detection wavelength. Decays were recorded to ~ 10,000 counts in the peak channel. The decay transients were fitted to multi-exponential functions convolved with the IRF.

Computational Modelling

Molecular quantum-chemical calculations were carried out using the density-functional theory (DFT) formalism as implemented in the Gaussian09 software.[49] The CAM-B3LYP hybrid functional[50] was used in conjunction with Pople split-valence basis sets[51] of 6-31g and 6-31g** quality for the H and non-H atoms, respectively. The LANL2DZ pseudopotential[52] and corresponding double-zeta basis sets were used to describe the Pt and Re atoms. Initial models of **1b**/**2b**, **1c**/**2c** and **M3**/**M4** were prepared from X-ray structures or using the Avogadro software.[53] The molecular structures were optimised in the gas phase and the minima confirmed to be stationary points from the absence of imaginary modes in the vibrational Hessian matrix. Time-dependent DFT (TD-DFT) calculations were carried out on the optimized models using adiabatic B3LYP to identify the 50 lowest-energy singlet and triplet states, a subset of which were characterized using natural transition orbitals.[41] Visualisation of the frontier orbitals was performed using VESTA.[54]

ASSOCIATED CONTENT

Supporting Information

Crystal structure data for **1c** and **M4** is available under the CCDC reference numbers **2009579** and **1964156**. A supporting information file is available including: crystallographic data for **1c** and **M4**; additional spectroscopic data; images and Cartesian coordinates of the optimized structures of **1b**, **2b**, **1c**, **2c**, **M3** and **M4**; and characterization of optical transitions identified from the TD-DFT calculations on **1b**, **2b**, **1c**, **2c**, **M3** and **M4** including breakdowns of the transitions into orbital components, images of the NTOs, and orbital energy-level spectra. This data is available online at [URL to be added by publisher].

Data-Access Statement

The crystal structures of **1c** and **M4** are available under the CCDC reference numbers **2009579** and **1964156**. Raw data from the spectroscopic characterization and computational modelling is available from the authors on request.

AUTHOR INFORMATION

Corresponding Authors

* E-Mail: msk@squ.edu.om (MSK), p.r.raithby@bath.ac.uk (PRR), jonathan.skelton@manchester.ac.uk (JMS), abouzied@squ.edu.om (OKAZ)

Notes

The authors declare no competing financial interests.

Acknowledgements

MSK thanks The BP Oman (Grant: EG/SQU-BP/SCI/CHEM/19/01) and The Ministry of Higher Education (MoHE), Oman (Grant: RC/RG-SCI/CHEM/20/01) for funding. PRR is grateful to the Engineering and Physical Sciences Research Council (UK) for support (EP/K004956/1). RAA gratefully acknowledges The Research Council (TRC), Oman (Project No. BFP/RGP/EI/18/076) for funding and A'Sharqiyah University, Oman for a research grant (ASU-FSFR/CAS/FSHN-01/2019). JMS is currently supported by a UK Research and Innovation Future Leaders Fellowship (MR/T043121/1), and is also grateful to the UK Engineering and Physical Sciences Research Council for funding (EP/K004956/1 and EP/P007821/1) and to the University of Manchester for the award of a Presidential Fellowship. The authors acknowledge Dr Rashid Ilmi, Department of Chemistry, Sultan Qaboos University, Oman for helpful discussions.

References

1. Haque, A.; Al-Balushi, R. A.; Al-Busaidi, I. J.; Khan, M. S.; Raithby, P. R. Rise of conjugated poly-ynes and poly(metalla-ynes): From design through synthesis to structure-property relationships and applications. *Chem. Rev.* **2018,** 118, 8474-8597.

2. Haque, A.; Al-Balushi, R. A.; Khan, M. S. σ-Acetylide complexes for biomedical applications: Features, challenges and future directions. *J. Organomet. Chem.* **2019,** 897, 95-106.

3. Haque, A.; Al Balushi, R. A.; Al-Busaidi, I. J.; Ilmi, R.; Al Rasbi, N.; Jayapal, M.; Khan, M. S.; Raithby, P. R. Synthesis, optical spectroscopy, structural, and DFT studies on dimeric iodo-bridged copper(I) complexes. *J. Organomet. Chem.* **2019,** 892, 75-82.

4. Ho, C. L.; Yu, Z. Q.; Wong, W. Y. Multifunctional polymetallaynes: properties, functions and applications. *Chem. Soc. Rev.* **2016,** 45 (19), 5264-95.

5. Cheng, Y. J.; Yang, S. H.; Hsu, C. S. Synthesis of conjugated polymers for organic solar cell applications. *Chem. Rev.* **2009,** 109, 5868-5923.

6. Bunz, U. H. Poly(aryleneethynylene)s: Syntheses, properties, structures, and applications. *Chem. Rev.* **2000,** 100, 1605-1644.

7. Nguyen, P.; Gomez-Elipe, P.; Manners, I. Organometallic polymers with transition metals in the main chain. *Chem. Rev.* **1999,** 99, 1515-1548.

8. Long, N. J.; Williams, C. K. Metal alkynyl sigma complexes: Synthesis and materials. *Angew. Chem.* **2003,** 42, 2586-2617.

9. Wilson, J. S.; Köhler, A.; Friend, R. H.; Al-Suti, M. K.; Al-Mandhary, M. R. A.; Khan, M. S.; Raithby, P. R. Triplet states in a series of Pt-containing ethynylenes. *J. Chem. Phys.* **2000,** 113, 7627-7634.

10. Wong, W.-Y.; Ho, C.-L. Organometallic photovoltaics: A new and versatile approach for harvesting solar energy using conjugated polymetallaynes. *Acc. Chem. Res.* **2010,** 43, 1246-1256.

11. Wong, W. Y.; Harvey, P. D. Recent progress on the photonic properties of conjugated organometallic polymers built upon the trans-bis (para-ethynylbenzene) bis (phosphine) platinum (II) chromophore and related derivatives. *Macromol. Rapid Commun.* **2010,** 31, 671-713.

12. Wong, W.-Y. Challenges in organometallic research–Great opportunity for solar cells and OLEDs. *J. Organomet. Chem.* **2009,** 694 (17), 2644-2647.

13. Wong, W.-Y.; Ho, C.-L. Di-, oligo-and polymetallaynes: Syntheses, photophysics, structures and applications. *Coord. Chem. Rev.* **2006,** 250, 2627-2690.

14. Khan, M. S.; Al-Suti, M. K.; Maharaja, J.; Haque, A.; Al-Balushi, R. A.; Raithby, P. R. Conjugated poly-ynes and poly (metalla-ynes) incorporating thiophene-based spacers for solar cell (SC) applications. *J. Organomet. Chem.* **2016,** 812, 13-33.

15. Yam, V. W.; Au, V. K.; Leung, S. Y. Light-emitting self-assembled materials based on d(8) and d(10) transition metal complexes. *Chem. Rev.* **2015,** 115 (15), 7589-728.

16. Wei, K.; Gao, Z.; Liu, H.; Wu, X.; Wang, F.; Xu, H. Mechanical activation of platinum–acetylide complex for olefin hydrosilylation. *ACS Macro Lett.* **2017,** 6, 1146-1150.

17. Green, K. A.; Cifuentes, M. P.; Samoc, M.; Humphrey, M. G. Syntheses and NLO properties of metal alkynyl dendrimers. *Coord. Chem. Rev.* **2011,** 255, 2025-2038.

18. Lima, J. C.; Rodriguez, L. Applications of gold(I) alkynyl systems: a growing field to explore. *Chem. Soc. Rev.* **2011,** 40, 5442-5456.

19. Al-Busaidi, I. J.; Haque, A.; Al Rasbi, N. K.; Khan, M. S. Phenothiazine-based derivatives for optoelectronic applications: A review. *Synth. Met.* **2019,** 257, 116189.

20. Al-Balushi, R. A.; Haque, A.; Jayapal, M.; Al-Suti, M. K.; Husband, J.; Khan, M. S.; Koentjoro, O. F.; Molloy, K. C.; Skelton, J. M.; Raithby, P. R. Experimental and theoretical investigation for the level of conjugation in carbazole-based precursors and their mono-, di-, and polynuclear Pt (II) complexes. *Inorg. Chem.* **2016,** 55, 6465-6480.

21. Al-Balushi, R. A.; Haque, A.; Jayapal, M.; Al-Suti, M. K.; Husband, J.; Khan, M. S.; Skelton, J. M.; Molloy, K. C.; Raithby, P. R. Impact of the alkyne substitution pattern and metalation on the

photoisomerization of azobenzene-based platinum(II) diynes and polyynes. *Inorg. Chem.* **2016,** 55, 10955-10967.

22. Shah, H. H.; Al-Balushi, R. A.; Al-Suti, M. K.; Khan, M. S.; Marken, F.; Sudlow, A. L.; Kociok-Kohn, G.; Woodall, C. H.; Raithby, P. R.; Molloy, K. C. New di-ferrocenyl-ethynylpyridinyl triphenylphosphine copper halide complexes and related di-ferricenyl electro-crystallized materials. *Dalton Trans.* **2014,** 43, 9497-9507.

23. Shah, H. H.; Al-Balushi, R. A.; Al-Suti, M. K.; Khan, M. S.; Woodall, C. H.; Sudlow, A. L.; Raithby, P. R.; Kociok-Kohn, G.; Molloy, K. C.; Marken, F. New multi-ferrocenyl- and multi-ferricenyl- materials via coordination-driven self-assembly and via charge-driven electro-crystallization. *Inorg. Chem.* **2013,** 52, 12012-12022.

24. Li, L.; Ho, C.-L.; Wong, W.-Y. Versatile control of the optical bandgap in heterobimetallic polymers through complexation of bithiazole-containing polyplatinynes with $ReCl(CO)_5$. *J. Organomet. Chem.* **2012,** 703, 43-50.

25. Wong, W.-Y.; Wong, W.-K.; Raithby, P. R. Synthesis, characterisation and properties of platinum (II) acetylide complexes of ferrocenylfluorene: Novel soluble donor–acceptor heterometallic materials. *Dalton Trans.* **1998,** (16), 2761-2766.

26. Patil, A.; Heeger, A.; Wudl, F. Optical properties of conducting polymers. *Chem. Rev.* **1988,** 88 (1), 183-200.

27. Brédas, J. L.; Silbey, R. *Conjugated polymers: the novel science and technology of highly conducting and nonlinear optically active materials*. Springer Science & Business Media: 2012.

28. Lee, C.; Yu, G.; Pakbaz, K.; Moses, D.; Sariciftci, N.; Wudl, F.; Heeger, A. Large enhancement of the transient and steady-state photoconductivity of conducting polymer/C60 composite films. *Synth. Met.* **1995,** 70 (1-3), 1353-1356.

29. Yam, V. W.-W.; Lo, K. K.-W.; Wong, K. M.-C. Luminescent polynuclear metal acetylides. *J. Organomet. Chem.* **1999,** 578, 3-30.

30. Khan, M. S.; Al-Suti, M. K.; Ahrens, B.; Raithby, P. R.; Teat, S. J. Trans-(5,5'-Diethynyl-2, 2'-bipyridine) bis[phenylbis (triethylphosphine) platinum(II)]. *Acta Crystallogr. E.* **2004,** 60 (6), m735-m737.

31. Khan, M. S.; Al-Mandhary, M. R. A.; Al-Suti, M. K.; Hisahm, A. K.; Raithby, P. R.; Ahrens, B.; Mahon, M. F.; Male, L.; Marseglia, E. A.; Tedesco, E.; Friend, R. H.; Kohler, A.; Feeder, N.; Teat, S. J. Structural characterisation of a series of acetylide-functionalised oligopyridines and the synthesis, characterisation and optical spectroscopy of platinum di-ynes and Ppoly-ynes containing oligopyridyl linker groups in the backbone. *Dalton Trans.* **2002,** 0, 1358-1368.

32. Gamelin, D. R.; George, M. W.; Glyn, P.; Grevels, F.-W.; Johnson, F. P. A.; Klotzbuecher, W.; Morrison, S. L.; Russell, G.; Schaffner, K.; Turner, J. J. Structural investigation of the ground and excited states of $ClRe(CO)_3(4, 4'\text{-bipyridyl})_2$ using vibrational spectroscopy. *Inorg. Chem.* **1994,** 33, 3246-3250.

33. Rotundo, L.; Azzi, E.; Deagostino, A.; Garino, C.; Nencini, L.; Priola, E.; Quagliotto, P.; Rocca, R.; Gobetto, R.; Nervi, C. Electronic effects of substituents on *fac*-M(bpy-R)$(CO)_3$ (M = Mn, Re) complexes for homogeneous CO2 electroreduction. *Front. Chem.* **2019,** 7, 417.

34. Lewis, J.; Long, N. J.; Raithby, P. R.; Shields, G. P.; Wong, W.-Y.; Younus, M. Synthesis and characterisation of new acetylide-functionalised oligothiophenes and their dinuclear platinum complexes. *Dalton Trans.* **1997,** (22), 4283-4288.

35. Yamamoto, Y.; Shiotsuka, M.; Onaka, S. Luminescent rhenium (I)–gold (I) hetero organometallics linked by ethynylphenanthrolines. *J. Organomet. Chem.* **2004,** 689, 2905-2911.

36. Schanze, K. S.; Macqueen, B. D.; Perkins, T. A.; Cabana, L. A. Studies of intramolecular electron and energy transfer using the *fac*-(diimine) $Re^1(CO)_3$ chromophore. *Coord. Chem. Rev.* **1993,** 122, 63-89.

37. Worl, L. A.; Duesing, R.; Chen, P.; Meyer, T. J. Photophysical properties of polypyridyl carbonyl complexes of rhenium (I). *J. Chem. Soc., Dalton Trans.* **1991,** 849-858.

38. Wang, B.; Wasielewski, M. R. Design and synthesis of metal ion-recognition-induced conjugated polymers: an approach to metal ion sensory materials. *J. Am. Chem. Soc.* **1997,** 119, 12-21.

39. Sacksteder, L.; Lee, M.; Demas, J.; DeGraff, B. Long-lived, highly luminescent rhenium (I) complexes as molecular probes: intra-and intermolecular excited-state interactions. *J. Am. Chem. Soc.* **1993,** 115, 8230-8238.

40. Liu, Y.; Liu, H.; Yan, H.; Liu, Y.; Zhang, J.; Shan, W.; Lai, P.; Li, H.; Ren, L.; Li, Z. Aggregation-induced absorption enhancement for deep near-infrared II photoacoustic imaging of brain gliomas in vivo. *Adv. Sci.* **2019,** 6, 1801615.

41. Liu, Z.; Shao, P.; Huang, Z.; Liu, B.; Chen, T.; Qin, J. Two-photon absorption enhancement induced by aggregation due to intermolecular hydrogen bonding in V-shaped 2-hydroxypyrimidine derivatives. *Chem. Comm.* **2008,** (19), 2260-2262.

42. Kumar, A.; Sun, S.-S.; Lees, A. J. In *Photophysics of Organometallics*; Springer: 2009; pp 37-71.

43. Lees, A. J. Luminescence properties of organometallic complexes. *Chem. Rev.* **1987,** 87 (4), 711-743.

44. Baková, R.; Chergui, M.; Daniel, C.; Vlček Jr, A.; Záliš, S. Relativistic effects in spectroscopy and photophysics of heavy-metal complexes illustrated by spin–orbit calculations of [Re(imidazole)$(CO)_3$(phen)]$^+$. *Coord. Chem. Rev.* **2011,** 255 (7-8), 975-989.

45. Zahid, N. I.; Ji, L.; Khyasudeen, M. F.; Friedrich, A.; Hashim, R.; Marder, T. B.; Abou-Zied, O. K. Evidence of increased hydrophobicity and dynamics inside the tail region of glycolipid self-assemblies using 2-n-alkyl-pyrene derivatives to probe different locations. *Langmuir* **2019,** 35, 9584-9592.

46. Martin, R. L. Natural transition orbitals. *J. Chem. Phy.* **2003,** 118, 4775-4777.

47. Zahid, N. I.; Mahmood, M. S.; Subramanian, B.; Mohd Said, S.; Abou-Zied, O. K. New insight into the origin of the red/near-infrared intense fluorescence of a crystalline 2-hydroxychalcone derivative: A comprehensive picture from the excited-state femtosecond dynamics. *J. Phys. Chem. Lett.* **2017,** 8 (22), 5603-5608.

48. Farrugia, L. J. WinGX suite for small-molecule single-crystal crystallography. *J. Appl. Crystallogr.* **1999,** 32, 837-838.

49. Frisch, M.; Trucks, G.; Schlegel, H.; Scuseria, G.; Robb, M.; Cheeseman, J.; Scalmani, G.; Barone, V.; Petersson, G.; Nakatsuji, H. Gaussian 09, Revision E. 01, Gaussian. *Inc., Wallingford CT* **2016**.

50. Becke, A. D. Density-functional thermochemistry. III. The role of exact exchange. *J. Chem. Phy.* **1993,** 98 (7), 5648-5652.

51. Ditchfield, R.; Hehre, W. J.; Pople, J. A. Self-consistent molecular-orbital methods. IX. An extended Gaussian-type basis for molecular-orbital studies of organic molecules. *J. Chem. Phys.* **1971,** 54, 724-728.

52. Hay, P. J.; Wadt, W. R. Ab initio effective core potentials for molecular calculations. Potentials for the transition metal atoms Sc to Hg. *J. Chem. Phys.* **1985,** 82, 270-283.

53. Hanwell, M. D.; Curtis, D. E.; Lonie, D. C.; Vandermeersch, T.; Zurek, E.; Hutchison, G. R. Avogadro: an advanced semantic chemical editor, visualization, and analysis platform. *J. Cheminform.* **2012,** 4, 17.

54. Momma, K.; Izumi, F. VESTA 3 for three-dimensional visualization of crystal, volumetric and morphology data. *J. Appl. Crystallogr.* **2011,** 44 (6), 1272-1276.

Table of Contents Graphic

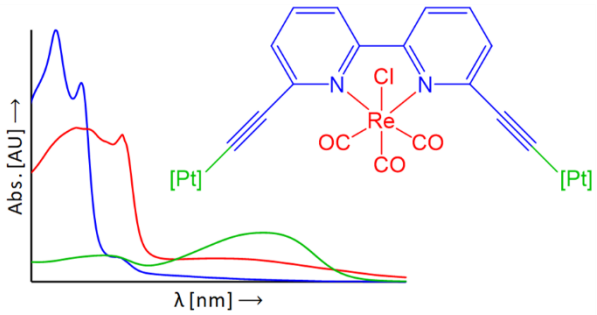

Two new heterobimetallic Pt(II) di-ynes and poly-ynes are prepared by incorporating $Re(CO)_3Cl$ moieties *via* chelation of the bipyridine spacer group. A chelated spacer and model di-yne are crystallised and studied by X-ray difraction, and the photophysical properties of the chelated spacers, di-ynes and poly-ynes are examined using absorption and emission spectroscopy and quantum-chemical modelling. The synergistic effect of the two metals on the optical properties highlights a novel route to fine-tuning the opto-electronic properties of these organometallic poly-ynes.

Supporting Information: Two is Better Than One? Investigating the Effect of Incorporating $Re(CO)_3Cl$ Side-Chains into Pt(II) Di-ynes and Poly-ynes

Ashanul Haque,[†,#] Rayya Al-Balushi,[‡] Idris Juma Al-Busaidi,[#] Nawal K. Al-Rasbi,[#] Sumayya Al-Bahri,[#] Mohammed K. Al-Suti,[#] Muhammad S. Khan,[#,*] Osama K. Abou-Zied,[#,*] Jonathan M. Skelton[§,ǁ,*] and Paul R. Raithby[§,*]

[†] Department of Chemistry, College of Science, University of Hail, Ha'il 81451, Kingdom of Saudi Arabia.

[‡] Department of Basic Sciences, College of Applied and Health Sciences, A'Sharqiyah University, Ibra 400, Sultanate of Oman.

[#] Department of Chemistry, Sultan Qaboos University, P.O. Box 36, Al Khod 123, Sultanate of Oman.

[§] Department of Chemistry, University of Bath, Claverton Down, Bath BA2 7AY, UK.

[ǁ] Department of Chemistry, University of Manchester, Oxford Road, Manchester M13 9PL, UK.

* Corresponding authors: msk@squ.edu.om (MSK) p.r.raithby@bath.ac.uk (PRR), jonathan.skelton@manchester.ac.uk (JMS) and abouzied@squ.edu.om (OKAZ).

Table S1 Crystallographic parameters for the refined **1c** and **M4** structures.

	1c	**M4**
Formula	$C_{17}H_8ClN_2O_3Re$	$C_{53}H_{76}ClN_2O_3P_4Pt_2Re$
M [g mol^{-1}]	509.90	1540.86
T [K]	293(2)	150(2)
Wavelength [Å]	0.71073	0.71073
Crystal system	Monoclinic	Triclinic
Space group	$P2_1/n$	P-1
a [Å]	12.420(3)	9.0435(6)
b [Å]	10.100(2)	17.6543(11)
c [Å]	13.860(3)	19.8468(13)
α [°]	90	78.318(5)
β [°]	105.20(3)	80.733(5)
γ [°]	90	85.391(5)
V [Å^3] (Z)	1677.8(6) (4)	3058.8 (2)
ρ_{calc} [mg m^{-3}]	2.019	1.673
μ [mm^{-1}]	7.418	6.724
F(000)	960	1496
Crystal size [mm^3]	0.200 × 0.200 × 0.150	0.30 × 0.20 × 0.20
θ range for data collection [°]	2.527-26.499°	3.563-27.500
Index ranges for data collection	$-15 \leq h \leq 15$, $-12 \leq k \leq 12$, $-17 \leq l \leq 17$	$-12 \leq h \leq 12$, $-24 \leq k \leq 22$, $-28 \leq l \leq 27$
Reflections collected (independent)	12806 (3484)	21746 (12973)
R_{Int} [%]	12.9	8.64
Completeness to θ = 23.00 ° [%]	100.0	93.4
Data / restraints / parameters	3484 / 0 / 218	12973 / 244 / 556
Goodness-of-fit on F^2	1.048	1.154
Final R indices [$I > 2\sigma(I)$]	R1 = 0.0637 wR2 = 0.1656	R1 = 0.0949 wR2 = 0.2549
R indices (all data)	R1 = 0.0753 wR2 = 0.1812	R1 = 0.1084 wR2 = 0.2636
Largest peak and deepest hole [e Å^{-3}]	2.846, -1.798	4.744, -3.606

Table S2 Characterisation of the brightest spin-allowed (singlet) transitions in the simulated absorption spectrum of **1b**. The table gives for each state the transition wavelength λ, the oscillator strength f, and a breakdown of the excited state into transitions between pairs of occupied and virtual orbitals with the corresponding percentage of the sum of squared coefficients c^2. Occupied and virtual orbitals are labelled relative to the highest-occupied and lowest-unoccupied molecular orbitals (HOMO/LUMO) respectively.

State #	**λ [nm]**	**f**	**Occ. Orb.**	**Virt. Orb.**	**% c^2**
5	290	1.294	HOMO - 1	LUMO + 3	2.66
			HOMO	LUMO	97.34

Table S3 Characterisation of the brightest spin-allowed (singlet) transitions in the simulated absorption spectrum of **2b**. The table gives for each state the transition wavelength λ, the oscillator strength f, and a breakdown of the excited state into transitions between pairs of occupied and virtual orbitals with the corresponding percentage of the sum of squared coefficients c^2. Occupied and virtual orbitals are labelled relative to the highest-occupied and lowest-unoccupied molecular orbitals (HOMO/LUMO) respectively.

State #	λ [nm]	f	Occ. Orb.	Virt. Orb.	% c^2
9	262	0.566	HOMO - 8	LUMO	2.59
			HOMO - 7	LUMO + 1	2.56
			HOMO	LUMO	80.28
			HOMO	LUMO + 2	14.56

Table S4 Characterisation of the brightest spin-allowed (singlet) transitions in the simulated absorption spectrum of **1c**. The table gives for each state the transition wavelength λ, the oscillator strength f, and a breakdown of the excited state into transitions between pairs of occupied and virtual orbitals with the corresponding percentage of the sum of squared coefficients c^2. Occupied and virtual orbitals are labelled relative to the highest-occupied and lowest-unoccupied molecular orbitals (HOMO/LUMO) respectively.

State #	λ [nm]	f	Occ. Orb.	Virt. Orb.	% c^2
6	355	0.078	HOMO - 1	LUMO	100.00
11	305	0.937	HOMO - 10	LUMO	2.19
			HOMO - 3	LUMO	97.81

Table S5 Characterisation of the brightest spin-allowed (singlet) transitions in the simulated absorption spectrum of **2c**. The table gives for each state the transition wavelength λ, the oscillator strength f, and a breakdown of the excited state into transitions between pairs of occupied and virtual orbitals with the corresponding percentage of the sum of squared coefficients c^2. Occupied and virtual orbitals are labelled relative to the highest-occupied and lowest-unoccupied molecular orbitals (HOMO/LUMO) respectively.

State #	λ [nm]	f	Occ. Orb.	Virt. Orb.	% c^2
7	345	0.066	HOMO - 1	LUMO	100.00
14	295	0.256	HOMO - 6	LUMO + 2	2.96
			HOMO - 3	LUMO	79.30
			HOMO	LUMO + 1	17.74
20	284	0.073	HOMO -3	LUMO	13.27
			HOMO -1	LUMO + 2	9.42
			HOMO -1	LUMO + 3	6.56
			HOMO	LUMO + 1	67.28
			HOMO	LUMO + 4	3.46
22	280	0.090	HOMO -3	LUMO	3.56
			HOMO -1	LUMO + 2	30.31
			HOMO -1	LUMO + 3	29.16
			HOMO -1	LUMO + 5	2.19
			HOMO	LUMO + 1	17.96
			HOMO	LUMO + 4	16.81

Table S6 Characterisation of the brightest spin-allowed (singlet) transitions in the simulated absorption spectrum of **M3**. The table gives for each state the transition wavelength λ, the oscillator strength f, and a breakdown of the excited state into transitions between pairs of occupied and virtual orbitals with the corresponding percentage of the sum of squared coefficients c^2. Occupied and virtual orbitals are labelled relative to the highest-occupied and lowest-unoccupied molecular orbitals (HOMO/LUMO) respectively.

State #	λ [nm]	f	Occ. Orb.	Virt. Orb.	% c^2
3	363	1.635	HOMO - 5	LUMO + 3	2.23
			HOMO - 3	LUMO	3.85
			HOMO - 1	LUMO	2.87
			HOMO	LUMO	91.04
9	335	0.356	HOMO - 3	LUMO	90.23
			HOMO - 3	LUMO + 1	3.81
			HOMO - 3	LUMO + 5	2.50
			HOMO	LUMO	3.46
11	327	0.063	HOMO - 4	LUMO	96.82
			HOMO - 4	LUMO + 1	3.18

Table S7 Characterisation of the brightest spin-allowed (singlet) transitions in the simulated absorption spectrum of **M4**. The table gives for each state the transition wavelength λ, the oscillator strength f, and a breakdown of the excited state into transitions between pairs of occupied and virtual orbitals with the corresponding percentage of the sum of squared coefficients c^2. Occupied and virtual orbitals are labelled relative to the highest-occupied and lowest-unoccupied molecular orbitals (HOMO/LUMO) respectively.

State #	λ [nm]	f	Occ. Orb.	Virt. Orb.	% c^2
11	331	0.595	HOMO - 15	LUMO	2.93
			HOMO - 5	LUMO	4.32
			HOMO - 4	LUMO	10.95
			HOMO - 3	LUMO	8.33
			HOMO - 1	LUMO	2.43
			HOMO - 1	LUMO + 2	2.98
			HOMO	LUMO	68.06
22	284	0.368	HOMO - 12	LUMO	10.60
			HOMO - 7	LUMO	14.31
			HOMO - 6	LUMO	37.19
			HOMO - 4	LUMO	4.05
			HOMO - 3	LUMO	7.09
			HOMO - 1	LUMO + 1	4.13
			HOMO	LUMO + 1	5.04
			HOMO	LUMO + 2	17.58
26	281	0.063	HOMO - 6	LUMO	3.51
			HOMO - 4	LUMO	2.81
			HOMO - 4	LUMO + 1	4.48
			HOMO - 3	LUMO + 1	5.68
			HOMO - 3	LUMO + 2	3.25
			HOMO - 1	LUMO + 1	4.95
			HOMO - 1	LUMO + 2	18.97
			HOMO	LUMO	5.28
			HOMO	LUMO + 1	47.49
			HOMO	LUMO + 2	3.58

Table S8 Characterisation of the low-lying spin-forbidden (triplet) transitions in the simulated absorption spectrum of **1b**. The table gives for each state the transition wavelength λ and a breakdown of the excited state into transitions between pairs of occupied and virtual orbitals with the corresponding percentage of the sum of squared coefficients c^2. Occupied and virtual orbitals are labelled relative to the highest-occupied and lowest-unoccupied molecular orbitals (HOMO/LUMO) respectively.

State #	λ [nm]	Occ. Orb.	Virt. Orb.	% c^2
1	474	HOMO - 5	LUMO + 2	3.12
		HOMO - 4	LUMO + 1	4.98
		HOMO - 1	LUMO + 1	11.07
		HOMO	LUMO	80.83
2	364	HOMO - 9	LUMO	2.97
		HOMO - 5	LUMO + 1	7.18
		HOMO - 4	LUMO + 2	7.25
		HOMO - 1	LUMO	47.74
		HOMO	LUMO + 3	34.87
3	305	HOMO - 7	LUMO + 1	3.01
		HOMO - 6	LUMO	3.37
		HOMO - 3	LUMO + 1	7.26
		HOMO - 3	LUMO + 3	2.38
		HOMO - 2	LUMO	74.99
		HOMO - 2	LUMO + 2	6.82
		HOMO - 2	LUMO + 6	2.16

Table S9 Characterisation of the low-lying spin-forbidden (triplet) transitions in the simulated absorption spectrum of **2b**. The table gives for each state the transition wavelength λ and a breakdown of the excited state into transitions between pairs of occupied and virtual orbitals with the corresponding percentage of the sum of squared coefficients c^2. Occupied and virtual orbitals are labelled relative to the highest-occupied and lowest-unoccupied molecular orbitals (HOMO/LUMO) respectively.

State #	λ [nm]	Occ. Orb.	Virt. Orb.	% c^2
1	426	HOMO - 7	LUMO + 3	4.56
		HOMO - 3	LUMO	7.65
		HOMO - 3	LUMO + 2	5.19
		HOMO - 1	LUMO + 1	18.75
		HOMO - 1	LUMO + 3	2.16
		HOMO	LUMO	49.54
		HOMO	LUMO + 2	12.15
2	374	HOMO - 7	LUMO	4.09
		HOMO - 3	LUMO + 1	6.32
		HOMO - 1	LUMO	3.49
		HOMO - 1	LUMO + 2	32.33
		HOMO	LUMO + 1	49.27
		HOMO	LUMO + 3	4.51
3	320	HOMO - 1	LUMO + 1	28.36
		HOMO	LUMO	34.36
		HOMO	LUMO + 2	37.28

Table S10 Characterisation of the low-lying spin-forbidden (triplet) transitions in the simulated absorption spectrum of **1c**. The table gives for each state the transition wavelength λ and a breakdown of the excited state into transitions between pairs of occupied and virtual orbitals with the corresponding percentage of the sum of squared coefficients c^2. Occupied and virtual orbitals are labelled relative to the highest-occupied and lowest-unoccupied molecular orbitals (HOMO/LUMO) respectively.

State #	λ [nm]	Occ. Orb.	Virt. Orb.	% c^2
1	492	HOMO - 6	LUMO + 3	5.73
		HOMO - 4	LUMO + 3	3.48
		HOMO - 3	LUMO	76.16
		HOMO - 3	LUMO + 1	4.19
		HOMO	LUMO	10.45
2	391	HOMO - 11	LUMO + 1	2.32
		HOMO - 10	LUMO + 2	2.86
		HOMO - 6	LUMO	6.23
		HOMO - 4	LUMO	15.73
		HOMO - 3	LUMO + 3	10.81
		HOMO - 1	LUMO	56.64
		HOMO - 1	LUMO + 1	5.40
3	377	HOMO - 3	LUMO	10.29
		HOMO	LUMO	80.82
		HOMO	LUMO + 1	4.68
		HOMO	LUMO + 5	4.20

Table S11 Characterisation of the low-lying spin-forbidden (triplet) transitions in the simulated absorption spectrum of **2c**. The table gives for each state the transition wavelength λ and a breakdown of the excited state into transitions between pairs of occupied and virtual orbitals with the corresponding percentage of the sum of squared coefficients c^2. Occupied and virtual orbitals are labelled relative to the highest-occupied and lowest-unoccupied molecular orbitals (HOMO/LUMO) respectively.

State #	λ [nm]	Occ. Orb.	Virt. Orb.	% c^2
1	443	HOMO - 10	LUMO	10.12
		HOMO - 6	LUMO + 2	4.83
		HOMO - 6	LUMO + 5	2.71
		HOMO - 5	LUMO	3.90
		HOMO - 4	LUMO + 2	4.28
		HOMO - 3	LUMO	14.29
		HOMO - 3	LUMO + 1	40.22
		HOMO - 1	LUMO + 2	4.58
		HOMO	LUMO	15.06
2	402	HOMO - 12	LUMO	3.12
		HOMO - 10	LUMO + 2	2.45
		HOMO - 6	LUMO + 1	12.34
		HOMO - 4	LUMO	4.80
		HOMO - 4	LUMO + 1	4.07
		HOMO - 3	LUMO + 2	27.71
		HOMO - 1	LUMO	39.12
		HOMO - 1	LUMO + 1	6.39
3	374	HOMO - 6	LUMO + 2	3.10
		HOMO - 3	LUMO + 1	13.80
		HOMO	LUMO	78.15
		HOMO	LUMO + 4	4.95

Table S12 Characterisation of the low-lying spin-forbidden (triplet) transitions in the simulated absorption spectrum of **M3**. The table gives for each state the transition wavelength λ and a breakdown of the excited state into transitions between pairs of occupied and virtual orbitals with the corresponding percentage of the sum of squared coefficients c^2. Occupied and virtual orbitals are labelled relative to the highest-occupied and lowest-unoccupied molecular orbitals (HOMO/LUMO) respectively.

State #	λ [nm]	Occ. Orb.	Virt. Orb.	% c^2
1	550	HOMO - 15	LUMO	4.55
		HOMO - 5	LUMO + 3	3.88
		HOMO - 5	LUMO + 7	2.92
		HOMO - 1	LUMO	3.17
		HOMO	LUMO	85.48
2	417	HOMO - 22	LUMO	4.23
		HOMO - 18	LUMO	3.18
		HOMO - 9	LUMO	4.80
		HOMO - 5	LUMO	53.98
		HOMO - 1	LUMO	3.92
		HOMO	LUMO + 3	17.30
		HOMO	LUMO + 7	12.59

Table S13 Characterisation of the low-lying spin-forbidden (triplet) transitions in the simulated absorption spectrum of **M4**. The table gives for each state the transition wavelength λ and a breakdown of the excited state into transitions between pairs of occupied and virtual orbitals with the corresponding percentage of the sum of squared coefficients c^2. Occupied and virtual orbitals are labelled relative to the highest-occupied and lowest-unoccupied molecular orbitals (HOMO/LUMO) respectively.

State #	λ [nm]	Occ. Orb.	Virt. Orb.	% c^2
1	466	HOMO - 26	LUMO	4.75
		HOMO - 21	LUMO	3.07
		HOMO - 19	LUMO	3.12
		HOMO - 15	LUMO	8.27
		HOMO - 15	LUMO + 1	4.28
		HOMO - 4	LUMO	5.38
		HOMO - 4	LUMO + 1	8.81
		HOMO - 3	LUMO + 1	3.81
		HOMO - 2	LUMO	8.68
		HOMO - 1	LUMO +	8.06
		HOMO	LUMO	7.53
		HOMO	LUMO + 1	34.23
2	423	HOMO - 7	LUMO + 1	3.35
		HOMO - 6	LUMO + 1	6.61
		HOMO - 4	LUMO + 2	7.56
		HOMO - 3	LUMO	5.30
		HOMO - 3	LUMO + 1	5.06
		HOMO - 1	LUMO	13.18
		HOMO - 1	LUMO + 1	19.60
		HOMO	LUMO + 2	39.35
3	409	HOMO - 15	LUMO	4.21
		HOMO - 6	LUMO + 2	4.91
		HOMO - 5	LUMO	3.18
		HOMO - 4	LUMO	12.12
		HOMO - 3	LUMO	3.66
		HOMO - 1	LUMO + 2	9.95
		HOMO	LUMO	53.28
		HOMO	LUMO + 1	8.69

Listing S1 Cartesian coordinates of the optimized structure of **1b**.

H	0.13315	-7.19687	-0.37868
H	0.15071	7.16940	-0.20191
C	0.16512	-6.12977	-0.36140
C	0.20145	-4.92608	-0.34051
N	-0.96670	-1.42403	-0.46572
C	-0.93414	-2.74893	-0.47674
H	-1.88253	-3.26080	-0.61902
C	0.23954	-3.49740	-0.31734
C	1.43321	-2.79177	-0.13731
H	2.36710	-3.32824	-0.00966
C	1.40380	-1.40862	-0.12498
H	2.30377	-0.82379	0.01159
C	0.18161	-0.75603	-0.29319
N	1.25099	1.39652	-0.11489
C	0.10273	0.72852	-0.28764
C	-1.11947	1.38110	-0.45592
H	-2.01939	0.79625	-0.59269
C	-1.14889	2.76423	-0.44359
H	-2.08273	3.30073	-0.57150
C	0.04477	3.46989	-0.26344
C	1.21842	2.72144	-0.10390
H	2.16682	3.23330	0.03830
C	0.08283	4.89859	-0.24041
C	0.11902	6.10230	-0.22013

Listing S2 Cartesian coordinates of the optimized structure of **2b**.

N	-0.14962	1.80614	-0.01097
H	0.15271	6.28498	-0.02593
C	-0.19631	5.27579	-0.02104
C	-0.58240	4.13578	-0.01556
C	-1.06694	2.78062	-0.00886
C	-0.56811	0.53899	-0.00489
C	-1.92088	0.19319	0.00357
C	-2.86610	1.20735	0.00573
H	-3.92526	0.97223	0.01222
C	-2.44101	2.52835	-0.00056
H	-3.14454	3.35239	0.00085
C	0.48758	-0.51433	-0.00758
H	-2.20163	-0.85176	0.00825
N	0.06909	-1.78148	-0.00108
C	1.84035	-0.16853	-0.01645
C	0.98641	-2.75595	-0.00318
H	2.12110	0.87641	-0.02143
C	2.78557	-1.18269	-0.01862
C	0.50188	-4.11112	0.00390
C	2.36048	-2.50370	-0.01192
H	3.84473	-0.94758	-0.02547
C	0.11579	-5.25113	0.00974
H	3.06401	-3.32773	-0.01333
H	-0.23325	-6.26031	0.01493

Listing S3 Cartesian coordinates of the optimized structure of **1c**.

Re	0.32191	0.06203	-2.08817
Cl	-2.20715	0.10552	-1.96969
C	0.33216	1.41245	-3.45768
O	0.32127	2.24928	-4.25366
C	2.22926	0.02978	-2.03535
O	3.38717	0.01030	-1.99718
C	0.28679	-1.30281	-3.44280
O	0.24801	-2.14758	-4.22948
H	0.26316	7.24244	0.25643
H	-0.06590	-7.08639	0.31927
C	0.21456	6.18213	0.37631
C	0.15832	4.98750	0.50999
N	0.17845	1.40313	-0.35387
C	0.23258	2.73328	-0.43906
H	0.39245	3.15282	-1.42348
C	0.09161	3.57012	0.66835
C	-0.11313	2.97094	1.91291
H	-0.22619	3.58279	2.80005
C	-0.16836	1.59171	1.99845
H	-0.32313	1.12488	2.96145
C	-0.02321	0.82142	0.84871
N	0.12642	-1.25500	-0.34088
C	-0.06433	-0.65394	0.85398
C	-0.27731	-1.40618	2.00507
H	-0.43900	-0.92417	2.95947
C	-0.28768	-2.78717	1.93102
H	-0.45297	-3.38515	2.81941
C	-0.08202	-3.40635	0.69648
C	0.11866	-2.58687	-0.41472
H	0.27468	-3.02215	-1.39290
C	-0.07638	-4.82671	0.55130
C	-0.07020	-6.02387	0.42903

Listing S4 Cartesian coordinates of the optimized structure of **2c**.

Re	12.89654	17.76831	16.54479
Cl	13.58173	17.47973	18.97362
N	10.85009	17.62466	17.39871
C	12.30459	18.03993	14.75423
C	10.01423	16.56745	17.31495
C	8.87685	16.45958	18.11538
H	8.24494	15.58632	18.01732
C	8.58507	17.47184	19.01064
H	7.71516	17.40818	19.65418
C	9.40791	18.58526	19.05110
C	10.52543	18.64151	18.22480
C	11.37060	19.85593	18.13208
C	11.09457	21.00252	18.86974
C	10.26432	15.53426	16.35793
C	10.35396	14.63077	15.56845
C	13.24835	15.90604	16.22378
C	14.73464	18.04853	16.05693
H	9.17073	19.40082	19.71901
H	10.30157	21.01244	19.60367
C	11.84278	22.14816	18.65479
O	13.51736	14.79658	16.05271
O	15.85208	18.16187	15.79041
C	12.82177	22.13181	17.67874
H	11.64641	23.04772	19.22682
H	13.40761	23.01140	17.44485
H	10.47260	13.83661	14.86369
O	11.94410	18.20491	13.66470
N	12.37225	19.81679	17.22827
C	13.05957	20.95117	16.97489
C	14.03869	20.97391	15.93248
C	14.85281	21.11787	15.05837
H	15.58144	21.20705	14.28211

Listing S5 Cartesian coordinates of the optimized structure of **M3**.

Re	-1.37949	-0.05656	-1.14454
Cl	-3.14330	-0.07873	0.68083
C	-2.33929	1.29431	-2.11762
O	-2.91275	2.13270	-2.67092
C	0.04072	-0.04008	-2.41606
O	0.90881	-0.03010	-3.18466
C	-2.30960	-1.42660	-2.12237
O	-2.86154	-2.27601	-2.67906
Pt	-0.04346	8.10925	0.53548
Pt	0.17877	-8.20804	0.58008
C	0.09461	6.08881	0.76699
C	0.18168	4.87794	0.91613
N	-0.31843	1.28440	0.22990
C	-0.36298	2.61544	0.15137
H	-0.92241	3.03395	-0.67501
C	0.26546	3.46717	1.06770
C	0.96188	2.85133	2.11591
H	1.46140	3.46090	2.86033
C	1.01013	1.47241	2.19625
H	1.55073	1.00502	3.00859
C	0.36506	0.69633	1.23669
N	-0.28995	-1.37759	0.22874
C	0.38613	-0.77549	1.23221
C	1.06469	-1.53765	2.17976
H	1.60854	-1.05917	2.98342
C	1.04866	-2.91687	2.09632
H	1.57450	-3.51575	2.83121
C	0.35158	-3.54738	1.05713
C	-0.30465	-2.70946	0.14795
H	-0.86215	-3.13850	-0.67449
C	0.29953	-4.96090	0.91140
C	0.25420	-6.17719	0.78501
C	-0.18072	10.17218	0.32993
C	0.26778	10.84394	-0.81985
H	0.70973	10.27300	-1.63400
C	0.16472	12.22685	-0.96301
H	0.52366	12.70360	-1.87191
C	-0.39648	12.99830	0.05048
H	-0.47941	14.07599	-0.05702
C	-0.84899	12.36505	1.20344
H	-1.28880	12.95005	2.00745
C	-0.74025	10.98070	1.33371
H	-1.10267	10.51959	2.25054
C	0.10141	-10.26696	0.37347
C	-0.10967	-11.11727	1.47122
H	-0.23802	-10.68711	2.46277
C	-0.16259	-12.50432	1.33917
H	-0.32852	-13.12455	2.21676
C	-0.00397	-13.09704	0.09013
H	-0.04429	-14.17716	-0.01802
C	0.20657	-12.28207	-1.01807
H	0.33218	-12.72673	-2.00238
C	0.25688	-10.89626	-0.87253
H	0.42262	-10.28925	-1.76063
P	-2.30255	7.98482	-0.09218
C	-2.92243	6.31062	-0.54128
H	-2.68206	5.65274	0.29795
H	-4.01387	6.35619	-0.62077
C	-2.30803	5.75338	-1.82552
H	-2.56144	6.36391	-2.69766
H	-2.67731	4.74092	-2.01504
H	-1.21889	5.70667	-1.74364
C	-3.43691	8.53640	1.24968
H	-3.26847	9.61078	1.37444
H	-4.46997	8.40691	0.91087
C	-3.21361	7.80943	2.57612
H	-2.19048	7.95560	2.93508
H	-3.38539	6.73289	2.48266
H	-3.90078	8.18968	3.33770
C	-2.74531	9.04960	-1.52970
H	-2.47371	10.06935	-1.24472
H	-2.06457	8.77644	-2.34282
C	-4.19796	8.98487	-2.00207
H	-4.47893	7.98022	-2.33060
H	-4.34274	9.66048	-2.85046
H	-4.89571	9.29019	-1.21734
P	2.23880	8.20833	1.06510
C	3.23587	7.37038	-0.23806
H	4.28031	7.34239	0.09390
H	2.87470	6.33826	-0.27700
C	3.12324	8.01837	-1.61773
H	2.08293	8.03453	-1.95726
H	3.70970	7.45613	-2.35034
H	3.49447	9.04758	-1.61659
C	3.07307	9.84492	1.22307
H	4.15127	9.66691	1.13385
H	2.76612	10.43700	0.35676
C	2.77040	10.61561	2.50792
H	1.69656	10.77583	2.63176
H	3.25280	11.59712	2.47451
H	3.14910	10.09412	3.39126
C	2.71511	7.27043	2.58119
H	2.74323	6.21866	2.28060
H	3.73832	7.55673	2.85034
C	1.76331	7.43163	3.76674
H	1.68650	8.47016	4.09819
H	2.11302	6.83562	4.61554
H	0.76134	7.08829	3.49718
P	2.49362	-8.27353	0.92774
C	3.40764	-7.25770	-0.30446
H	3.01141	-6.24295	-0.20114
H	4.46665	-7.22409	-0.02728
C	3.23623	-7.74629	-1.74273
H	3.64575	-8.75150	-1.88253
H	3.75494	-7.07835	-2.43647
H	2.17855	-7.77141	-2.02304
C	2.97754	-7.51750	2.53388
H	4.06981	-7.46098	2.58889
H	2.59897	-6.49135	2.50051
C	2.40826	-8.25061	3.74839
H	1.31608	-8.30011	3.69810
H	2.68203	-7.73016	4.67078
H	2.78883	-9.27411	3.82093
C	3.30118	-9.92744	0.89855
H	2.78783	-10.53544	1.64948
H	3.04144	-10.38082	-0.06267
C	4.81304	-9.94698	1.12065
H	5.08919	-9.53406	2.09530
H	5.34679	-9.38049	0.35198
H	5.18174	-10.97646	1.08443
P	-2.13088	-8.03025	0.23287
C	-3.06387	-9.59609	-0.02200
H	-2.59648	-10.09867	-0.87394
H	-2.84450	-10.23137	0.84127
C	-4.57159	-9.45744	-0.22950
H	-5.06296	-9.00033	0.63430
H	-5.01992	-10.44443	-0.37776
H	-4.80975	-8.85337	-1.10983
C	-2.97974	-7.17181	1.62075
H	-2.49977	-6.19164	1.69858
H	-4.02676	-7.00094	1.34908
C	-2.87652	-7.91778	2.95091
H	-3.37344	-8.89210	2.91060
H	-3.34825	-7.33861	3.74995
H	-1.83007	-8.08452	3.22499
C	-2.53067	-6.97527	-1.22026
H	-3.61406	-6.82213	-1.26449
H	-2.07397	-6.00286	-1.01234
C	-2.00540	-7.53394	-2.54252
H	-0.92207	-7.68435	-2.50050
H	-2.22049	-6.84058	-3.36069
H	-2.46896	-8.49356	-2.79138

Listing S6 Cartesian coordinates of the optimized structure of **M4**.

Re	12.57637	17.96184	16.49429
Cl	13.34714	17.75853	18.91682
P	14.63923	20.78577	11.82097
P	17.28551	22.54694	15.26341
P	11.20333	11.62884	16.53874
P	9.29008	14.00277	12.97335
N	10.56477	17.76618	17.41122
C	11.93110	18.20819	14.72989
C	10.07671	10.30052	17.13427
H	10.59047	9.72315	17.91019
H	9.92396	9.63079	16.28252
C	8.73303	10.82083	17.64413
H	8.85382	11.46884	18.51775
H	8.21680	11.39616	16.86926
H	8.08731	9.98771	17.93697
C	10.22226	15.52109	12.52806
H	10.20553	16.15086	13.42080
H	9.68034	16.05824	11.74242
C	11.62565	12.61880	18.03182
H	10.71078	13.14195	18.32423
H	12.31047	13.40110	17.69306
C	12.73908	10.70398	16.12525
H	12.47856	10.03673	15.29901
H	13.00467	10.07346	16.98044
C	9.07182	13.07363	11.39884
H	8.49737	12.17557	11.64446
H	10.06386	12.71023	11.11449
C	8.42131	13.83885	10.24692
H	9.00647	14.71607	9.95615
H	8.34146	13.19191	9.36815
H	7.41157	14.17657	10.49820
C	7.61987	14.64970	13.39600
H	7.26573	15.28530	12.57744
H	7.76653	15.29526	14.26742
C	6.60120	13.55539	13.71372
H	6.41476	12.91042	12.84947
H	6.94961	12.92316	14.53642
H	5.64515	13.99822	14.00787
C	9.78739	16.65502	17.41709
C	8.68346	16.56008	18.28178
H	8.09482	15.65173	18.26803
C	8.37513	17.60631	19.12179
H	7.53531	17.53944	19.80486
C	9.14212	18.76291	19.06405
C	10.21664	18.81904	18.18897
C	10.99521	20.06730	17.99558
C	10.64582	21.24797	18.63554
C	10.04526	15.56380	16.54657
C	10.12591	14.54765	15.86835
C	12.98222	16.10744	16.18657
C	14.39920	18.27989	15.96863
C	11.66730	15.25347	12.10985
C	12.21511	11.84908	19.21296
C	13.91154	11.59999	15.72763
H	8.89334	19.60301	19.69596
H	9.83822	21.27592	19.35243
C	11.33790	22.41307	18.33287
O	13.32179	15.01658	16.00800
O	15.51652	18.38349	15.69159
C	12.32831	22.37116	17.37661
H	12.20816	14.72375	12.90032
H	11.72501	14.65172	11.19728
H	12.18351	16.19929	11.92202
H	11.52967	11.08266	19.58691
H	13.15794	11.35928	18.95260
H	12.42111	12.53673	20.03866
H	14.77509	10.98953	15.44723
H	14.21865	12.25739	16.54577
H	13.65170	12.23411	14.87539
H	11.08432	23.34470	18.82695
H	12.86927	23.26166	17.08295
C	14.55726	18.95568	11.99815
C	12.87159	21.29056	11.87687
C	15.17404	21.08503	10.08395
C	16.43049	23.79414	16.31128
C	17.69648	21.20859	16.45722
C	18.89572	23.31619	14.81053
H	13.87951	18.55711	11.23536
H	14.08689	18.76994	12.96680
C	15.91874	18.26483	11.93467
H	12.31185	20.70576	11.13945
H	12.50765	20.99566	12.86487
C	12.66230	22.78856	11.65763
C	14.30368	20.46611	8.99077
H	16.20418	20.72466	10.01304
H	15.23993	22.17038	9.96065
C	16.03180	25.05941	15.55224
H	17.06886	24.03716	17.16713
H	15.54159	23.29058	16.70208
H	16.73697	20.79565	16.78251
C	18.56517	20.10218	15.85952
H	18.17787	21.65079	17.33608
H	18.66729	24.13456	14.12106
H	19.43321	22.57682	14.20985
C	19.75913	23.80681	15.97223
H	15.80049	17.18465	12.06156
H	16.57627	18.62891	12.72917
H	16.41978	18.43379	10.97655
H	11.60254	23.04339	11.75064
H	12.99212	23.10467	10.66294
H	13.21739	23.37280	12.39810
H	14.72377	20.69475	8.00668
H	13.28205	20.85639	9.01003
H	14.24914	19.37709	9.07851
H	15.38373	24.81821	14.70390
H	15.48893	25.74438	16.21022
H	16.90530	25.59473	15.16719
H	18.07886	19.65074	14.99016
H	18.73235	19.31282	16.59786
H	19.54455	20.47719	15.54647
H	19.25722	24.58344	16.55660
H	20.02737	22.99409	16.65365
H	20.69045	24.23490	15.58943
Pt	10.26844	12.84649	14.76110
O	11.53218	18.38555	13.65118
N	12.00790	20.01218	17.09989
C	10.39162	11.11179	13.62448
C	12.65014	21.15467	16.75277
H	12.33752	11.52611	12.78779
C	13.64366	21.16585	15.73747
C	14.49925	21.35375	14.88209
Pt	15.95447	21.74208	13.50758
C	17.42702	22.21382	12.12797
C	17.45729	23.46807	11.49635
C	18.44686	21.31786	11.76867
H	16.69312	24.20522	11.73648
C	18.43709	23.80938	10.56535
H	18.47638	20.33055	12.22474
C	19.43250	21.64688	10.83856
C	19.43357	22.89782	10.22912
H	18.42151	24.79225	10.10044
H	20.20331	20.92150	10.58944
H	20.19919	23.15853	9.50397
C	11.50355	10.82763	12.81411
C	11.58127	9.67507	12.03367
C	10.53703	8.75491	12.03403
H	10.59272	7.85595	11.42685
C	9.42084	9.00628	12.82558
H	8.59468	8.29951	12.83930
C	9.35627	10.16272	13.60250
H	8.46661	10.32907	14.20719
H	12.46181	9.49605	11.42147

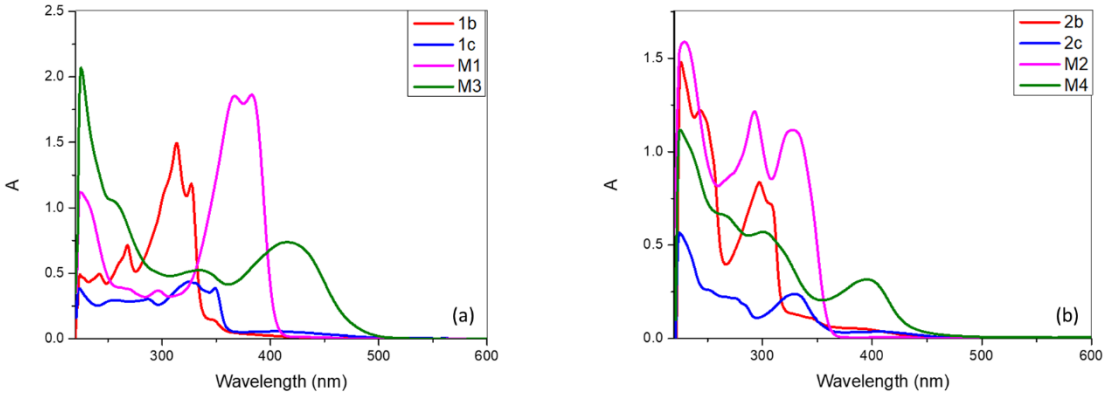

Figure S1 Absorption spectra of the 5,5'-bipyridine compounds **1b**, **1c**, **M1** and **M3** (a) and the analogous 6,6'-bipyridine compounds **2b**, **2c**, **M2** and **M4** (b) in 1×10^{-5} M CH_2Cl_2 solution at room temperature.

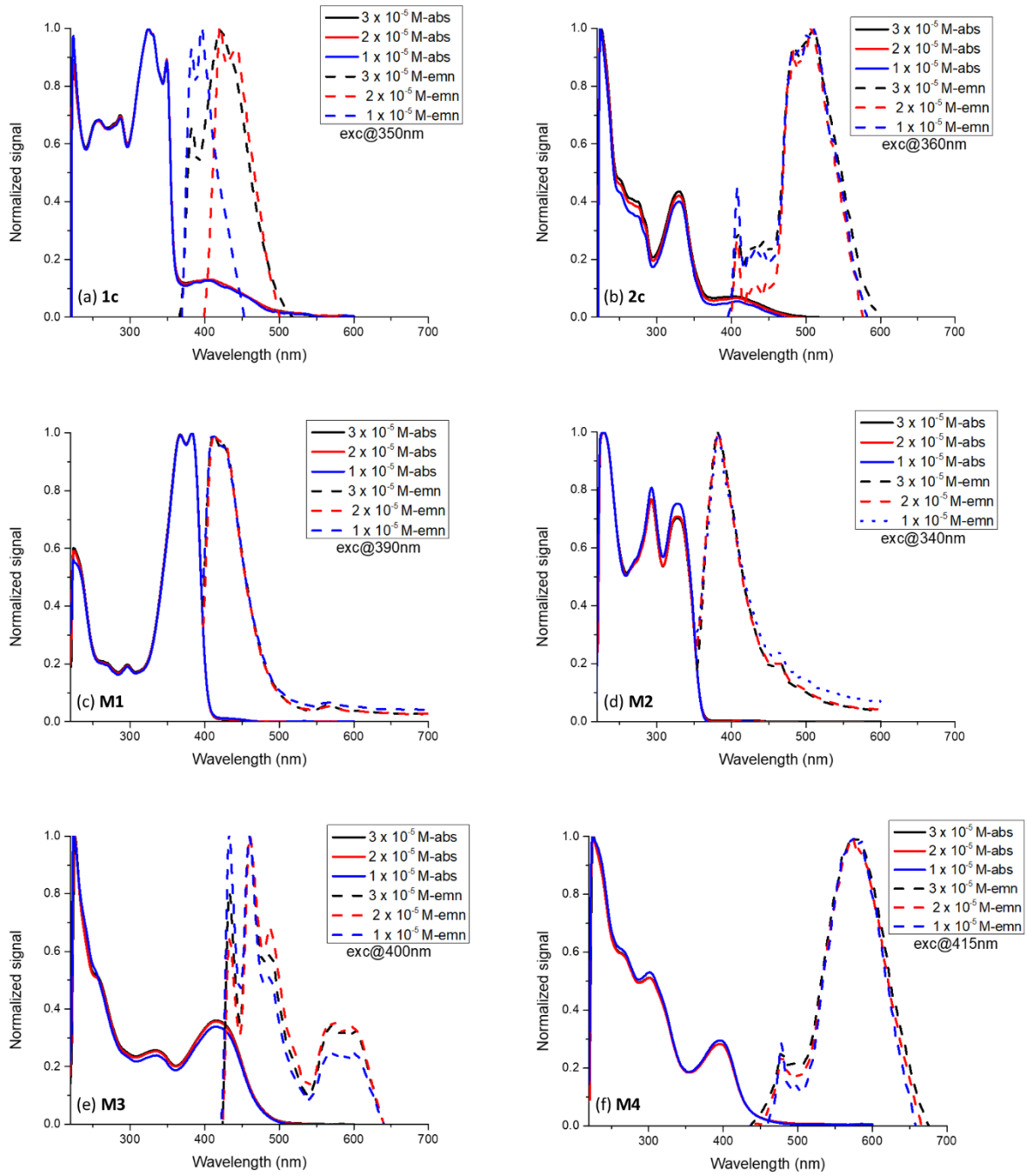

Figure S2 UV/visible absorption and emission spectra of **1c** (a), **2c** (b), **M1** (c), **M2** (d), **M3** (e) and **M4** (f) in CH_2Cl_2 solution at concentrations from 1×10^{-5} to 3×10^{-5} M. Emission spectra were recorded at the excitation wavelengths marked on the individual plots.

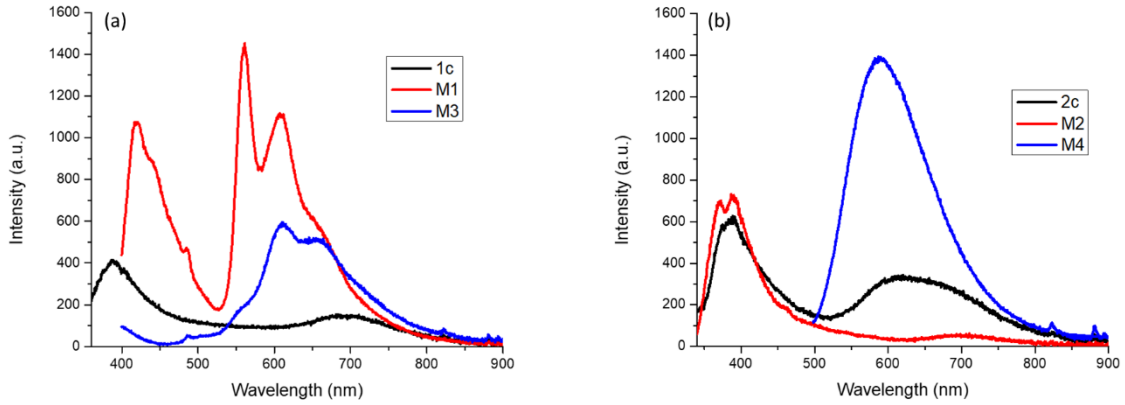

Figure S3 Solid-state emission spectra of the 5,5-bipyridine compounds **1c**, **M1** and **M3** (a) and the analogous 6,6-bipyridine compounds **2c**, **M2** and **M4** (b).

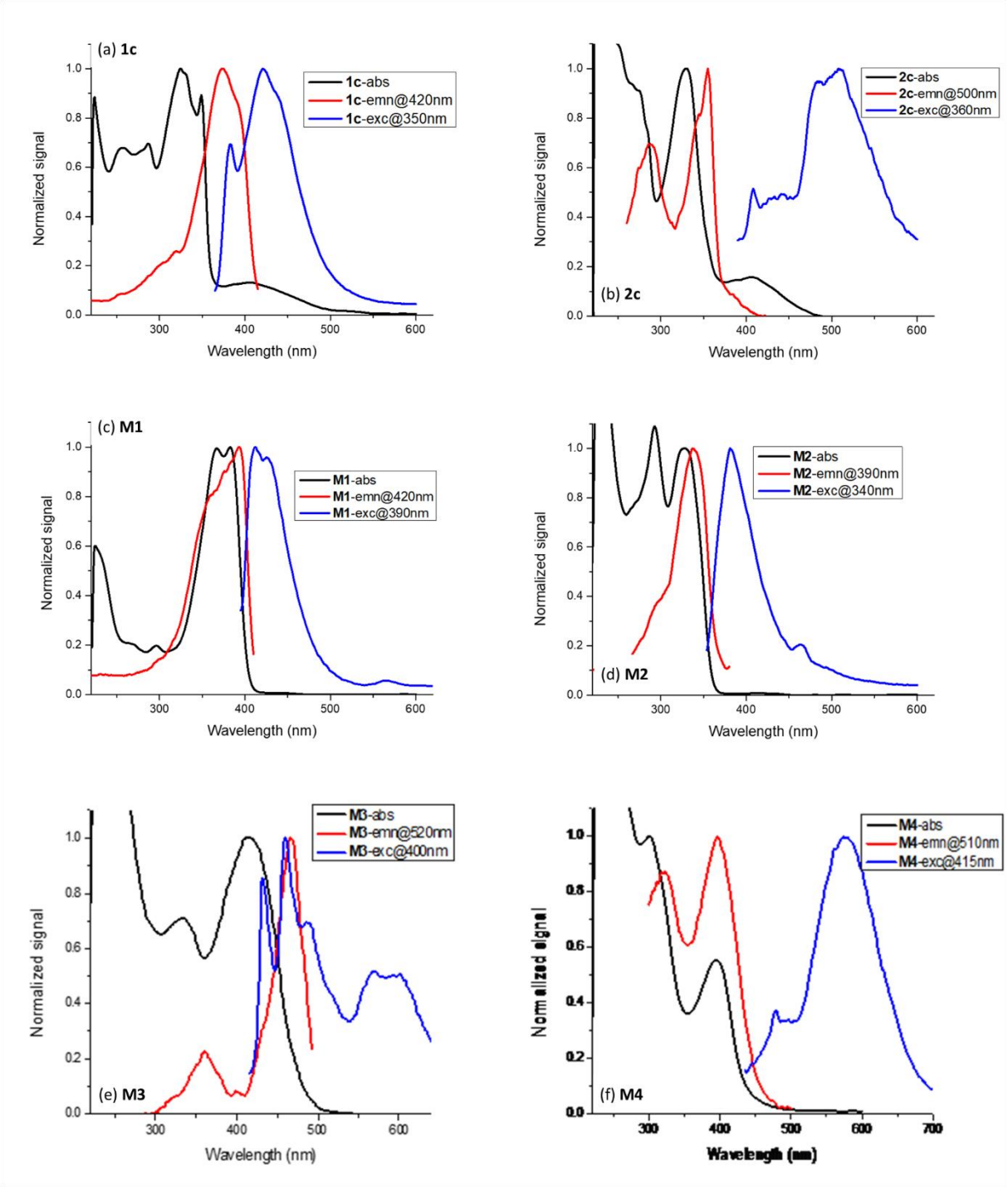

Figure S4 Absorption, fluorescence excitation and fluorescence emission spectra of **1c**, **2c**, **M1**, **M2**, **M3** and **M4** in 3×10^{-5} M CH_2Cl_2 solution. The emission and excitation wavelengths for the excitation and emission spectra, respectively, are indicated on the subplot legends.

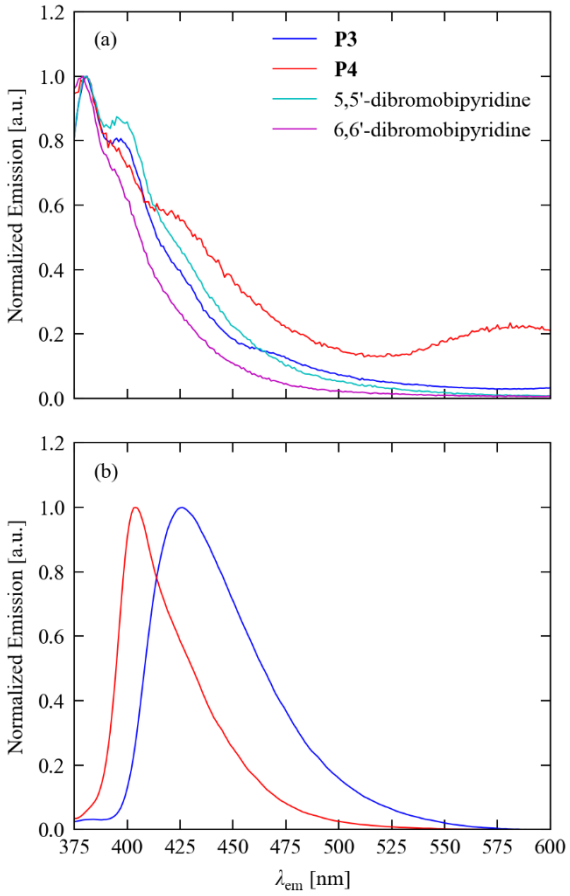

Figure S5 Emission spectra of the polymers **P3** and **P4** in 1 × 10^{-5} M CH_2Cl_2 solution (a) and in the solid state (b). The solution spectra of the 5,5'- and 6,6'-dibromobipyridine are shown in (a) for comparison. Excitation wavelengths λ_{ex}: (a) **P3** - 350 nm, **P4** - 340 nm, 5,5'-dibromobipyridine - 350 nm, 6,6'-dibromobipyridine - 340 nm; (b) **P3** - 350 nm, **P4** - 370 nm.

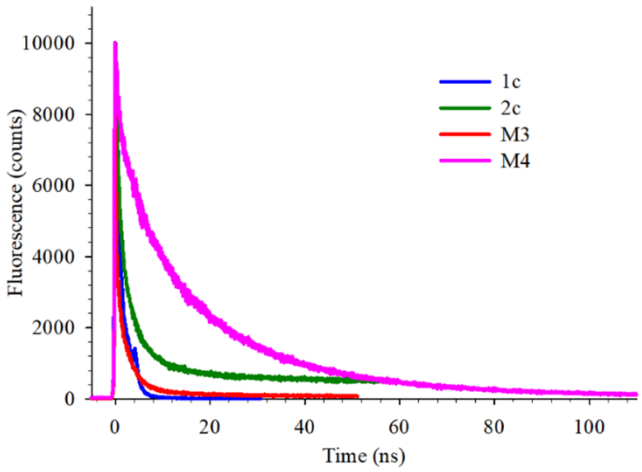

Figure S6 Room temperature fluorescence decay transients of **1c**/**2c** and **M3**/**M4** in CH_2Cl_2 (1 × 10^{-5} M). This is the same data as Figure 5 in the text shown to a longer decay time.

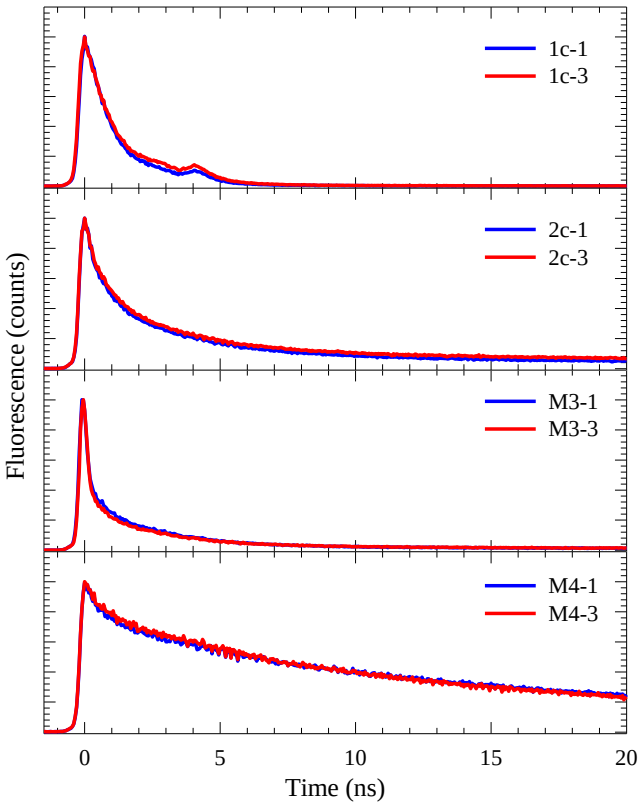

Figure S7 Fluorescence decay transients of **1c**, **2c**, **M3** and **M4** measured at room temperature in CH_2Cl_2 at two different concentrations (1: 1×10^{-5} M and 3: 3×10^{-5} M).

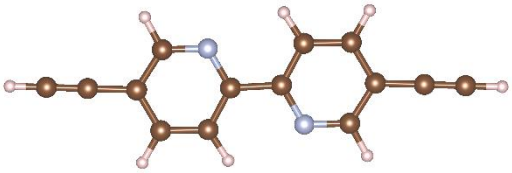

Figure S8 Optimised structure of **1b**.

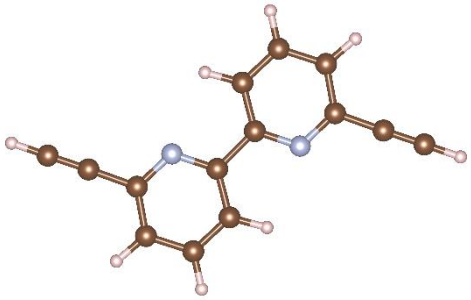

Figure S9 Optimised structure of **2b**.

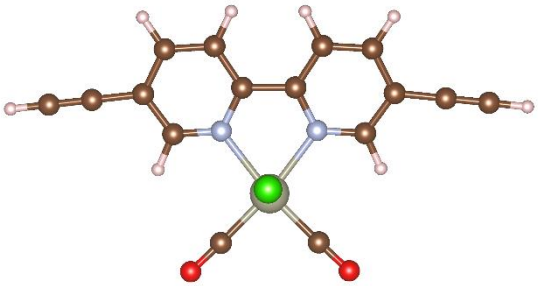

Figure S10 Optimised structure of **1c**.

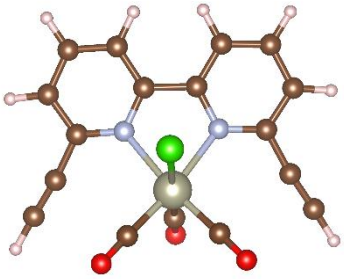

Figure S11 Optimised structure of **2c**.

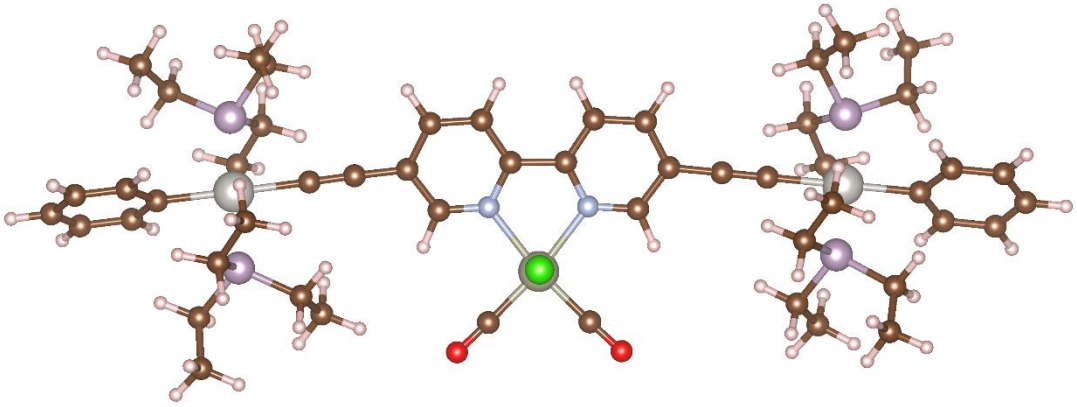

Figure S12 Optimised structure of **M3**.

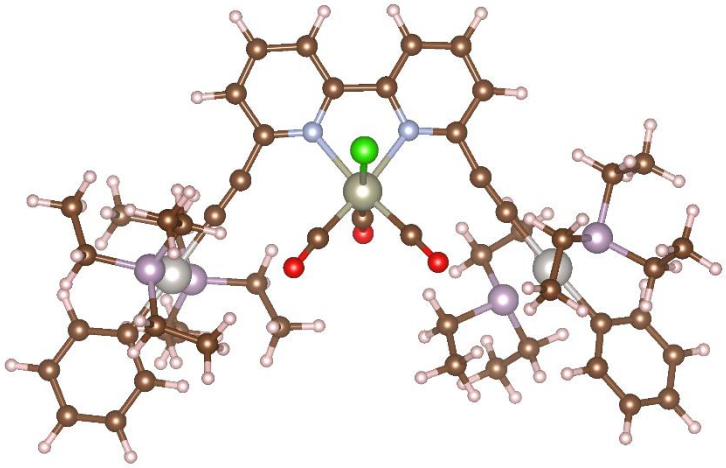

Figure S13 Optimized structure of **M4**.

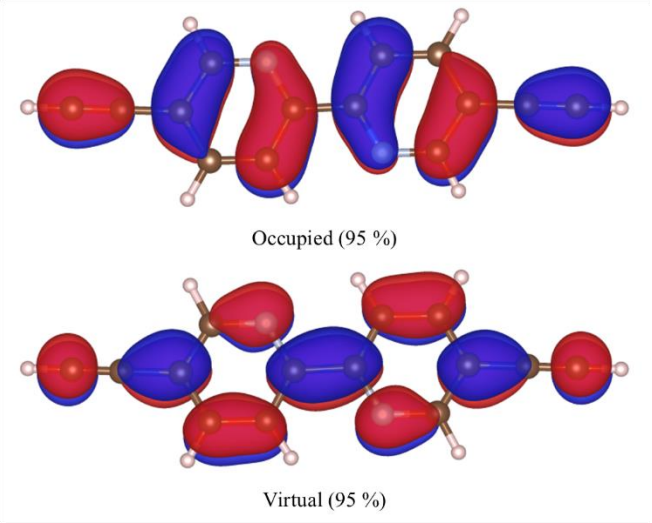

Figure S14 Natural transition orbitals (NTOs) for singlet excited state #5 in in the simulated spectrum of **1b** (λ = 290 nm, f = 1.294), showing the occupied particle and virtual hole states associated with the electronic transition. The isosurface is drawn to a value of 2.5×10^{-2} e bohr^{-3}.

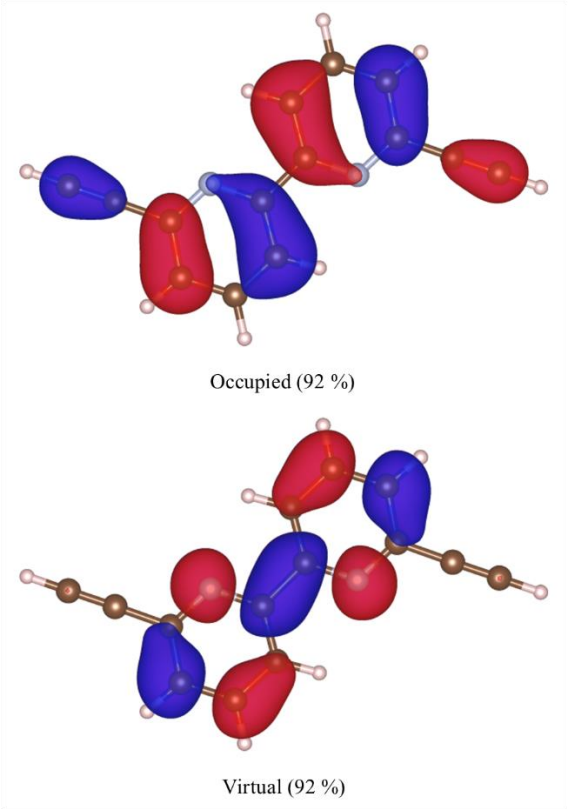

Figure S15 Natural transition orbitals (NTOs) for singlet excited state #9 in in the simulated spectrum of **2b** (λ = 262 nm, f = 0.566), showing the occupied particle and virtual hole states associated with the electronic transition. The isosurface is drawn to a value of 2.5×10^{-2} e bohr^{-3}.

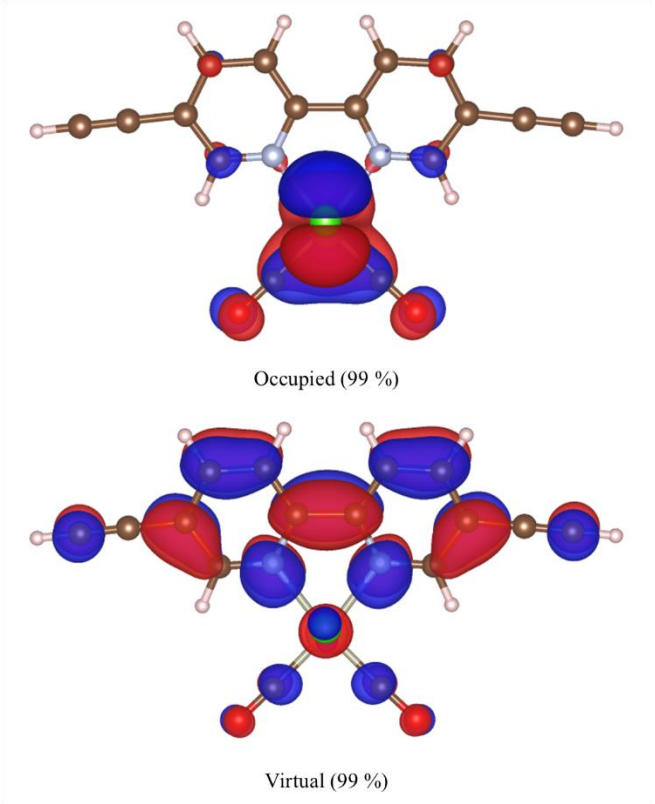

Figure S16 Natural transition orbitals (NTOs) for singlet excited state #6 in in the simulated spectrum of **1c** (λ = 355 nm, f = 0.078), showing the occupied particle and virtual hole states associated with the electronic transition. The isosurface is drawn to a value of 2.5×10^{-2} e bohr^{-3}.

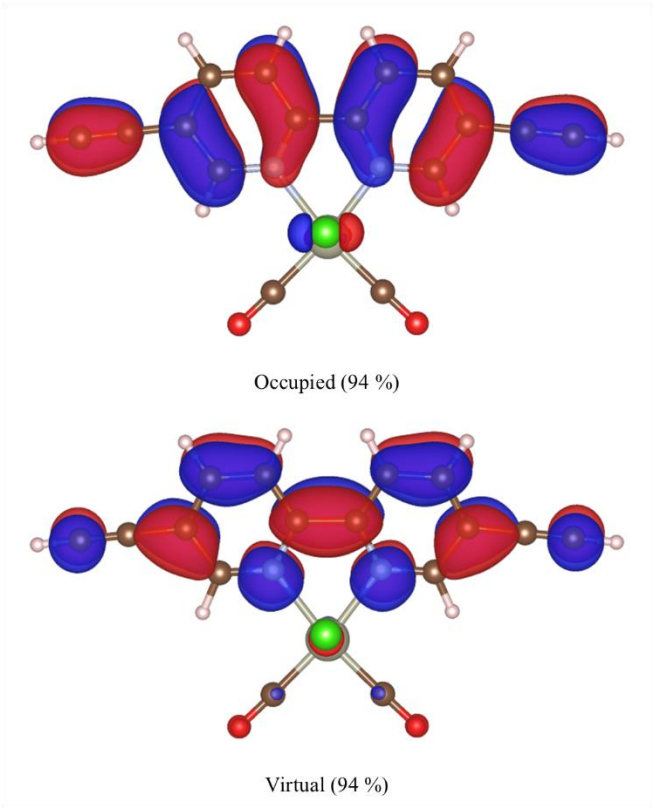

Figure S17 Natural transition orbitals (NTOs) for singlet excited state #11 in in the simulated spectrum of **1c** (λ = 305 nm, f = 0.937), showing the occupied particle and virtual hole states associated with the electronic transition. The isosurface is drawn to a value of 2.5×10^{-2} e bohr^{-3}.

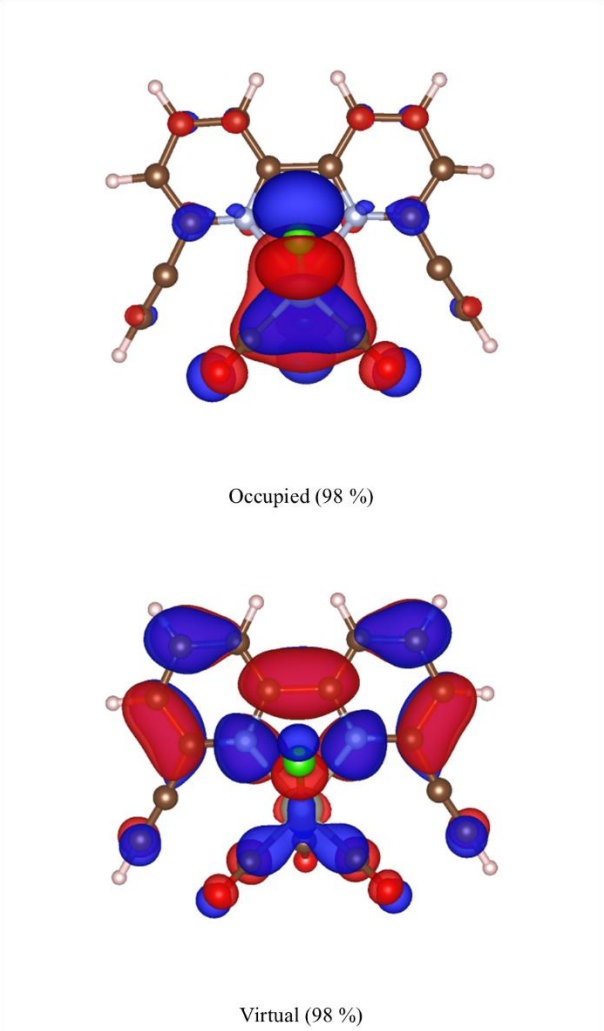

Figure S18 Natural transition orbitals (NTOs) for singlet excited state #7 in in the simulated spectrum of **2c** (λ = 345 nm, f = 0.066), showing the occupied particle and virtual hole states associated with the electronic transition. The isosurface is drawn to a value of 2.5×10^{-2} e bohr^{-3}.

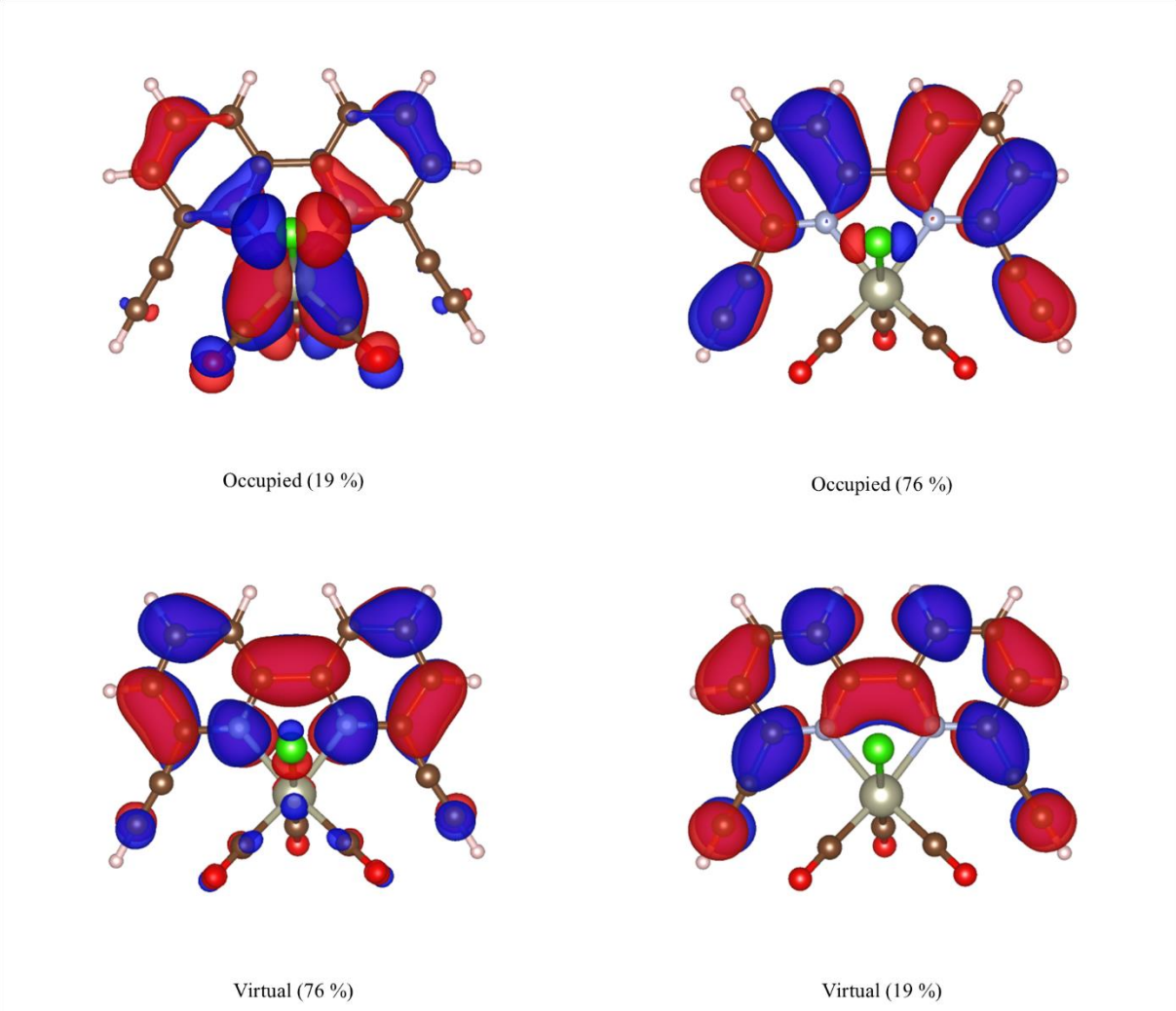

Figure S19 Natural transition orbitals (NTOs) for singlet excited state #14 in in the simulated spectrum of **2c** (λ = 295 nm, f = 0.256), showing the occupied particle and virtual hole states associated with the electronic transition. The isosurface is drawn to a value of 2.5×10^{-2} e bohr^{-3}.

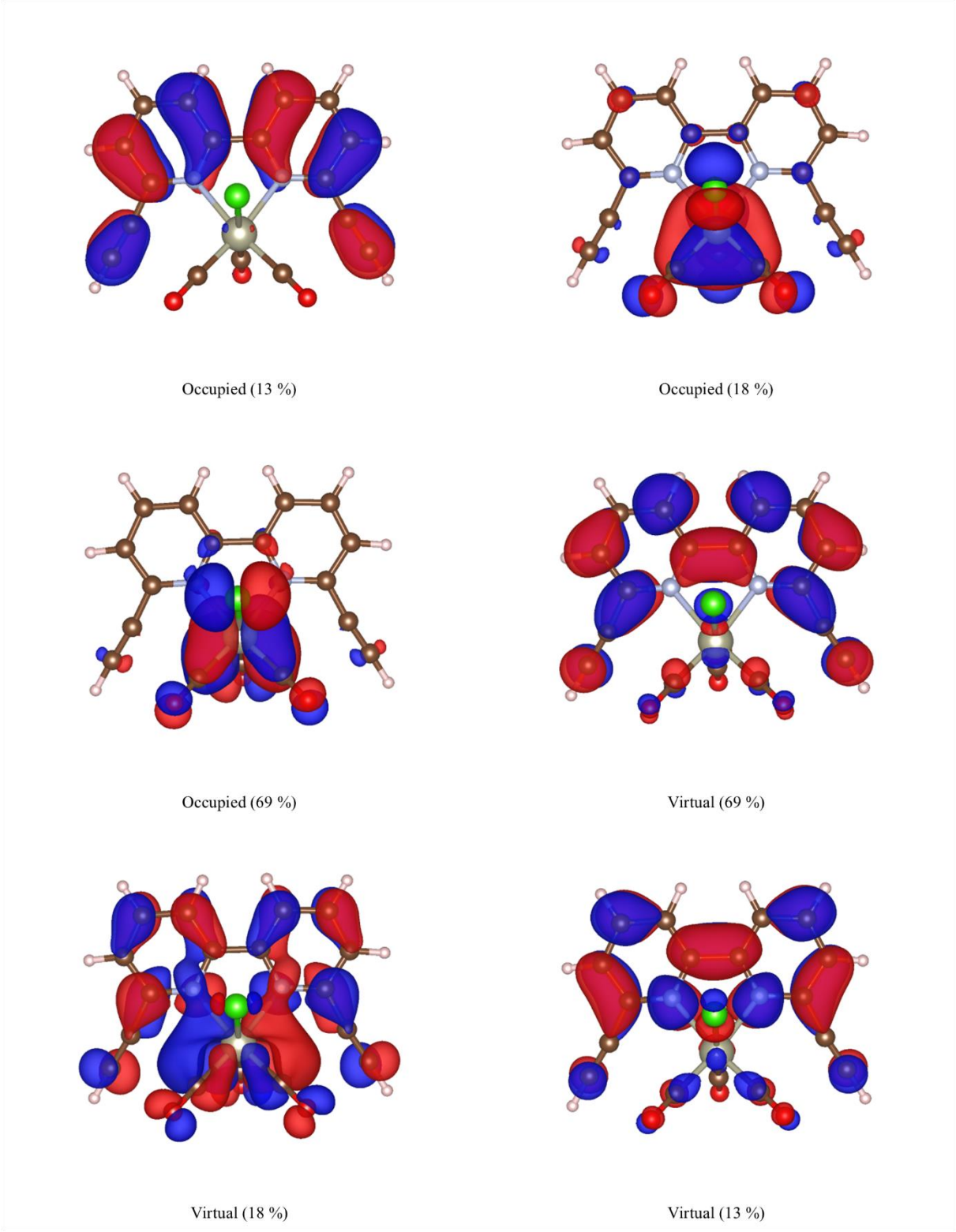

Figure S20 Natural transition orbitals (NTOs) for singlet excited state #20 in in the simulated spectrum of **2c** (λ = 284 nm, f = 0.073), showing the occupied particle and virtual hole states associated with the electronic transition. The isosurface is drawn to a value of 2.5×10^{-2} e bohr^{-3}.

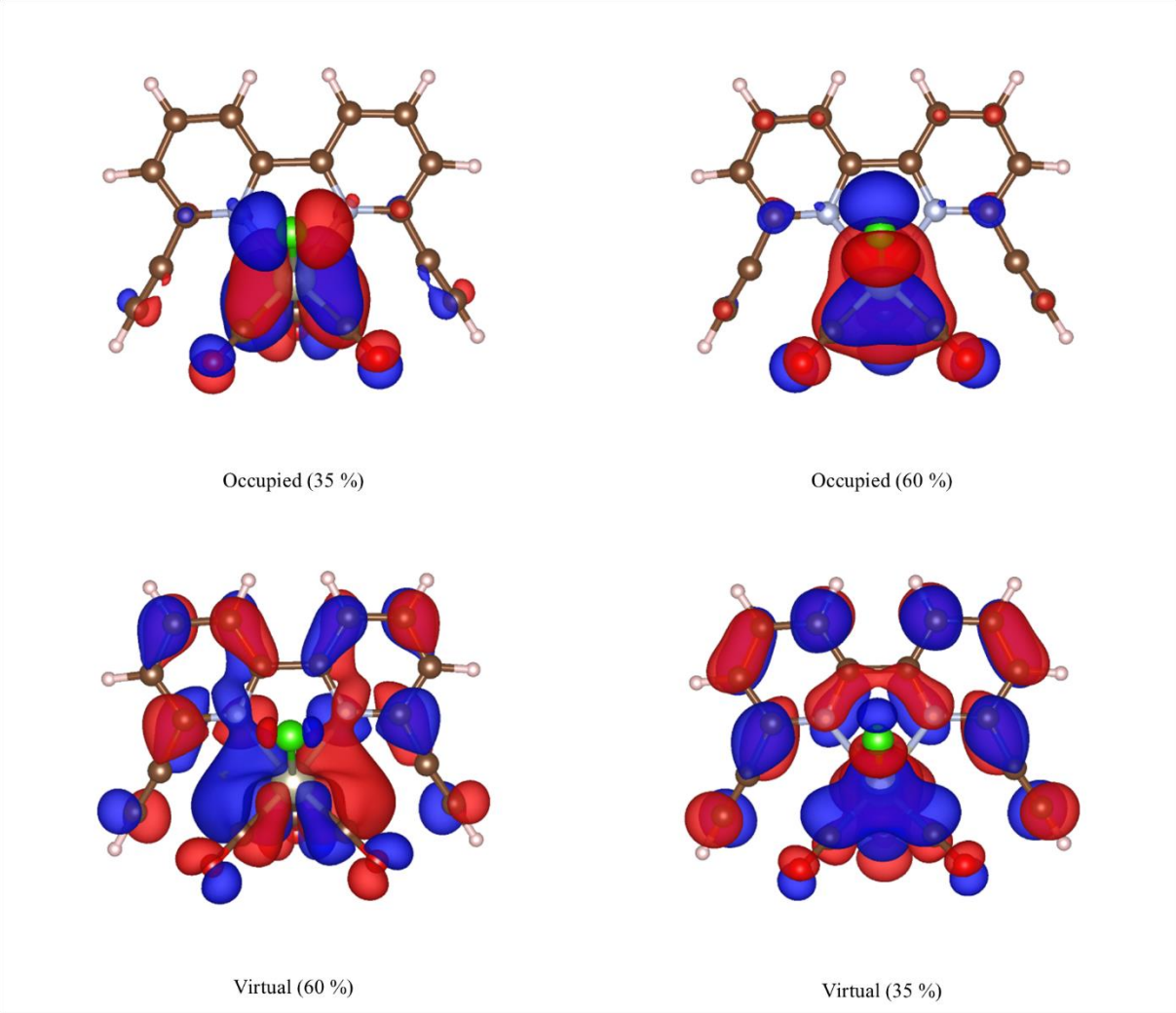

Figure S21 Natural transition orbitals (NTOs) for singlet excited state #22 in in the simulated spectrum of **2c** (λ = 280 nm, f = 0.090), showing the occupied particle and virtual hole states associated with the electronic transition. The isosurface is drawn to a value of 2.5×10^{-2} e bohr^{-3}.

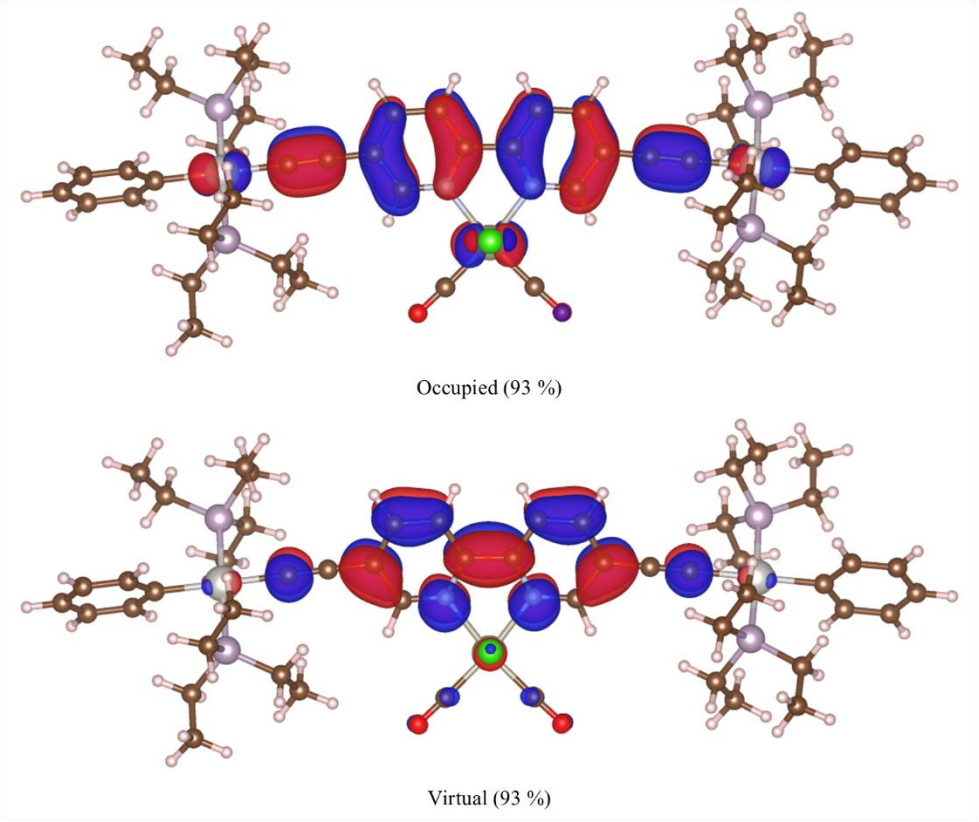

Figure S22 Natural transition orbitals (NTOs) for singlet excited state #3 in in the simulated spectrum of **M3** (λ = 363 nm, f = 1.635), showing the occupied particle and virtual hole states associated with the electronic transition. The isosurface is drawn to a value of 2.5×10^{-2} e bohr^{-3}.

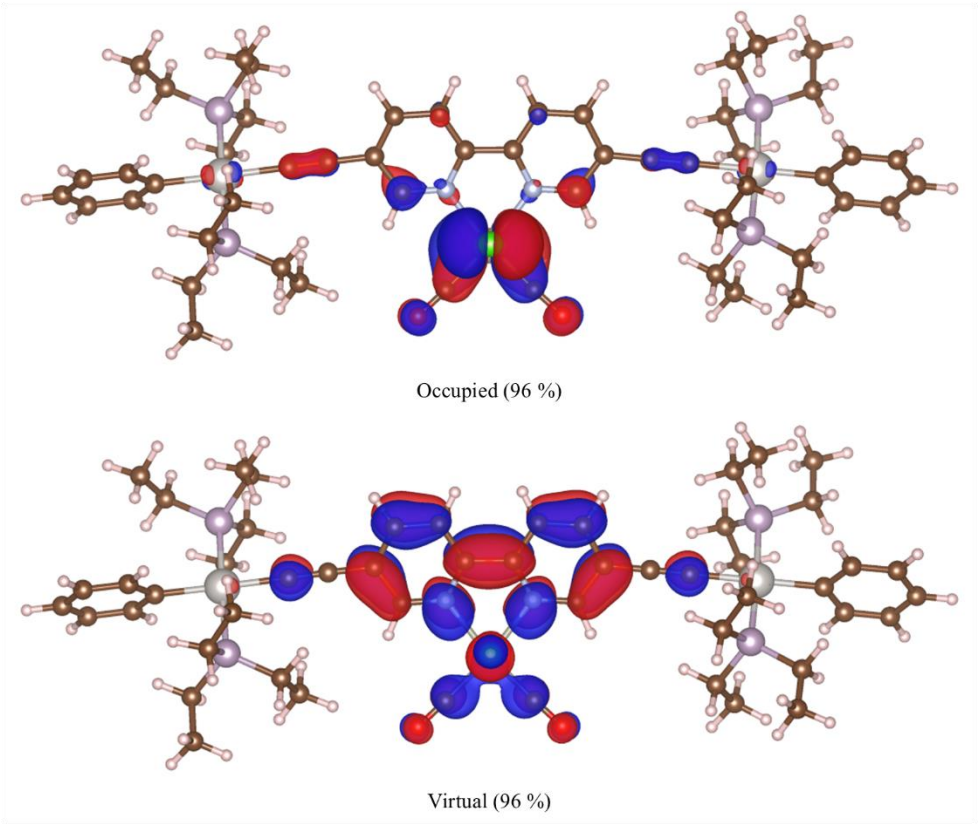

Figure S23 Natural transition orbitals (NTOs) for singlet excited state #9 in in the simulated spectrum of **M3** (λ = 335 nm, f = 0.356), showing the occupied particle and virtual hole states associated with the electronic transition. The isosurface is drawn to a value of 2.5×10^{-2} e bohr^{-3}.

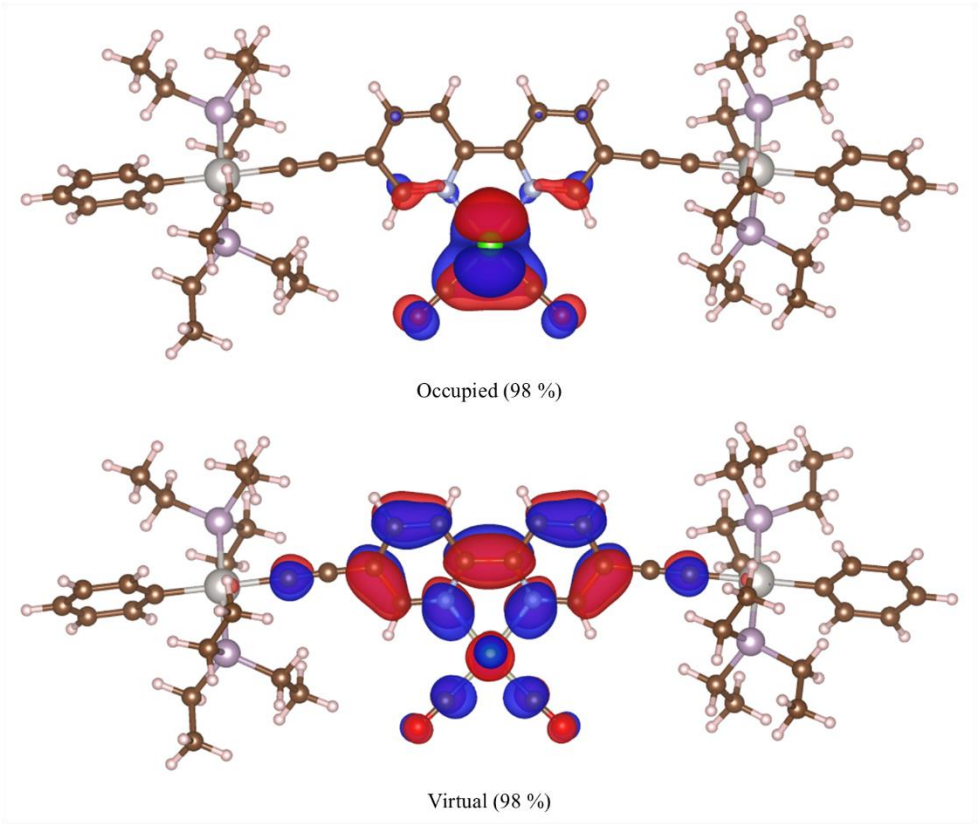

Figure S24 Natural transition orbitals (NTOs) for singlet excited state #11 in in the simulated spectrum of **M3** (λ = 327 nm, f = 0.063), showing the occupied particle and virtual hole states associated with the electronic transition. The isosurface is drawn to a value of 2.5×10^{-2} e bohr^{-3}.

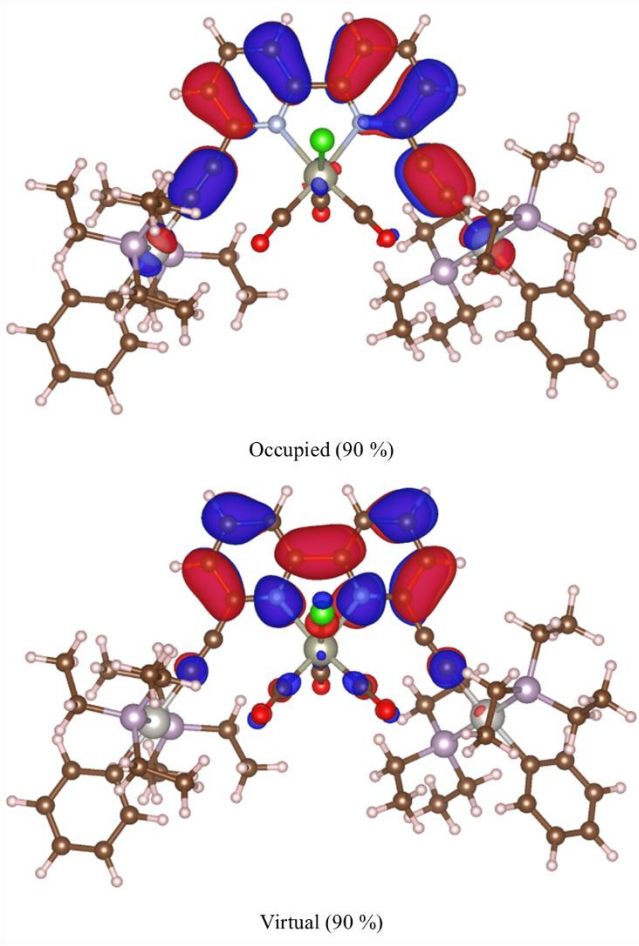

Figure S25 Natural transition orbitals (NTOs) for singlet excited state #11 in in the simulated spectrum of **M4** (λ = 331 nm, f = 0.595), showing the occupied particle and virtual hole states associated with the electronic transition. The isosurface is drawn to a value of 2.5×10^{-2} e bohr^{-3}.

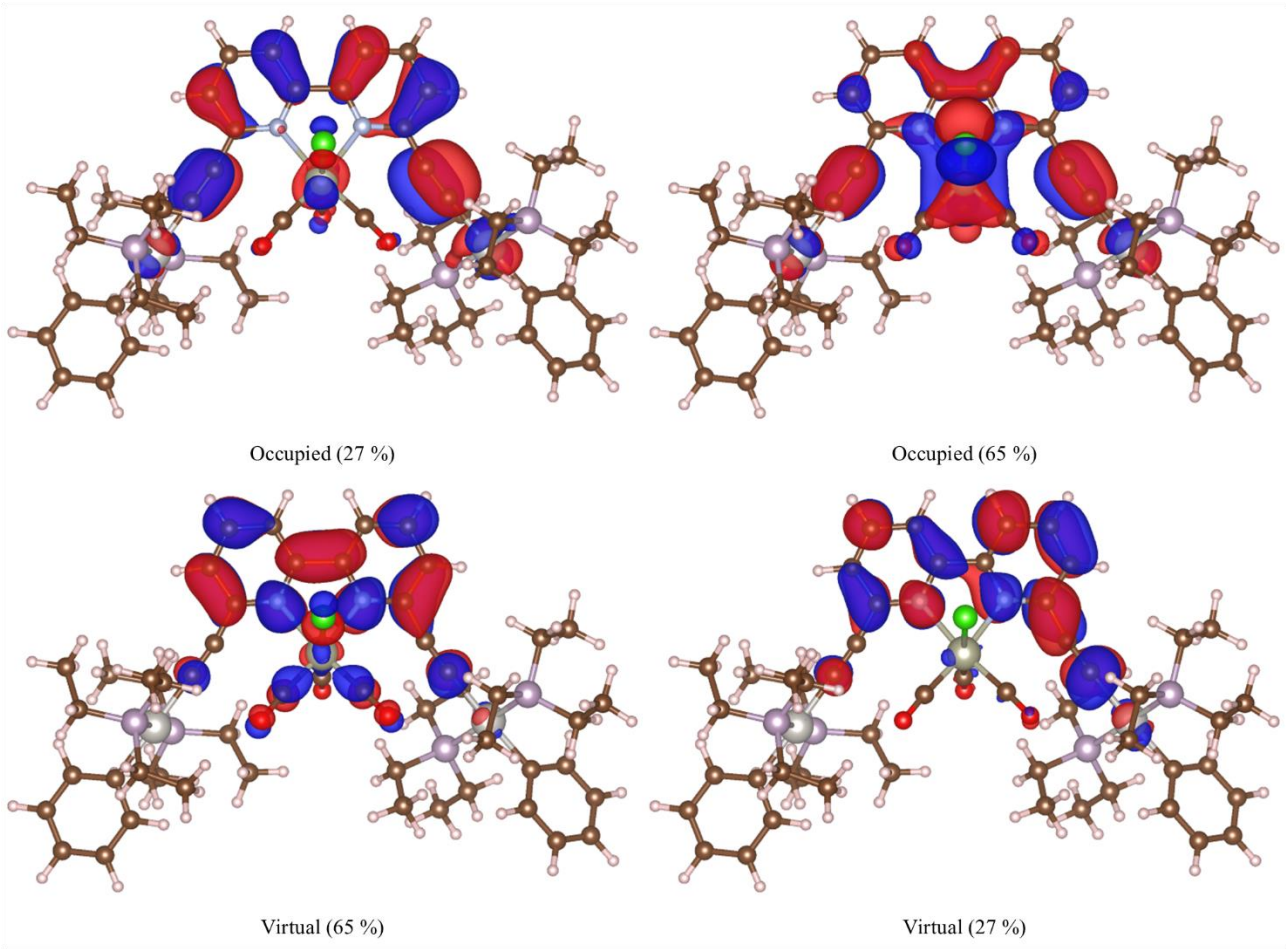

Figure S26 Natural transition orbitals (NTOs) for singlet excited state #22 in in the simulated spectrum of **M4** (λ = 284 nm, f = 0.368), showing the occupied particle and virtual hole states associated with the electronic transition. The isosurface is drawn to a value of 2.5×10^{-2} e bohr^{-3}.

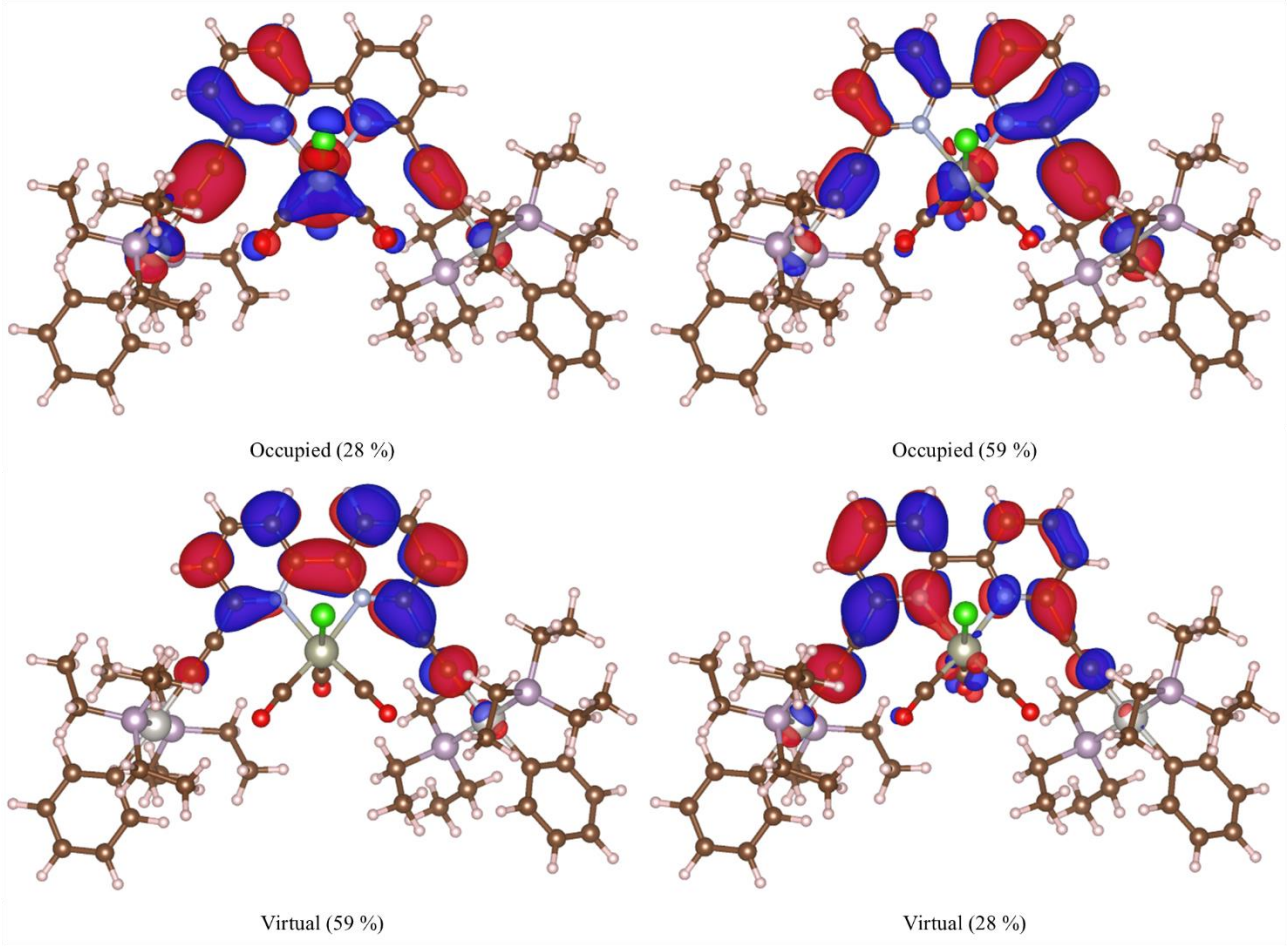

Figure S27 Natural transition orbitals (NTOs) for singlet excited state #26 in in the simulated spectrum of **M4** (λ = 281 nm, f = 0.063), showing the occupied particle and virtual hole states associated with the electronic transition. The isosurface is drawn to a value of 2.5×10^{-2} e bohr^{-3}.

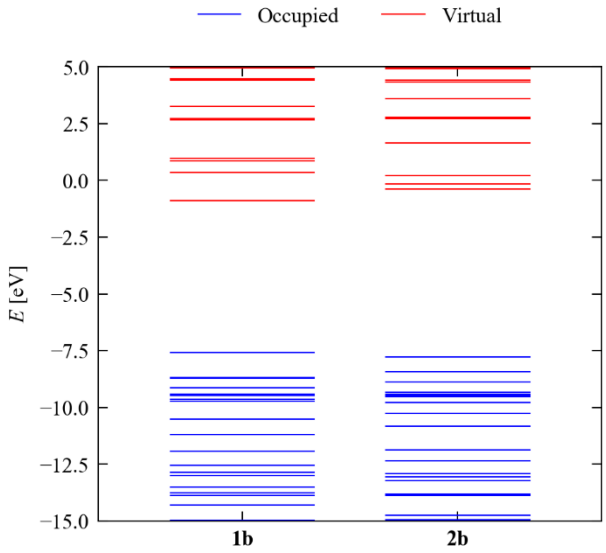

Figure S28 Spectra of the orbital energies of **1b** and **2b**. Occupied and virtual orbitals are colored blue and red respectively.

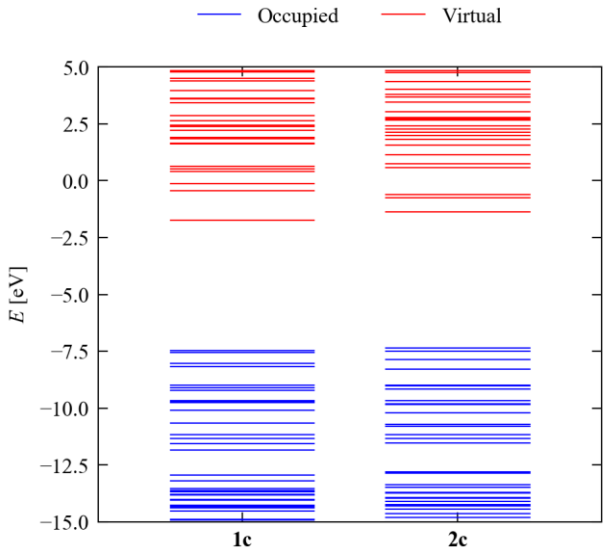

Figure S29 Spectra of the orbital energies of **1c** and **2c**. Occupied and virtual orbitals are colored blue and red respectively.

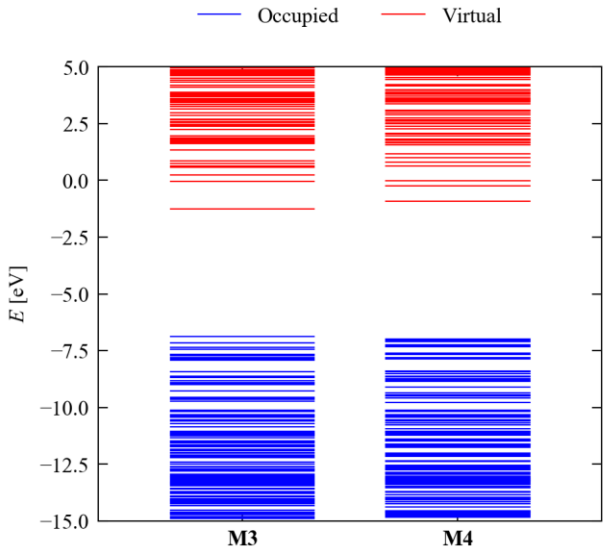

Figure S30 Spectra of the orbital energies of **M3** and **M4**. Occupied and virtual orbitals are colored blue and red respectively.

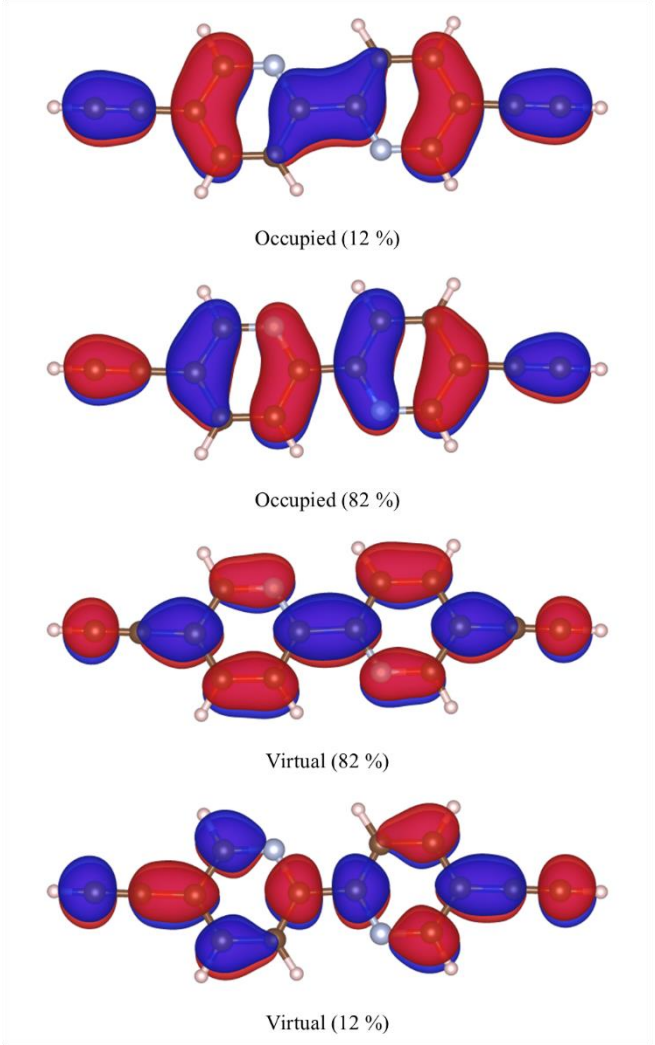

Figure S31 Natural transition orbitals (NTOs) for triplet excited state #1 in in the simulated spectrum of **1b** (λ = 474 nm), showing the occupied particle and virtual hole states associated with the electronic transition. The isosurface is drawn to a value of 2.5×10^{-2} *e* bohr^{-3}.

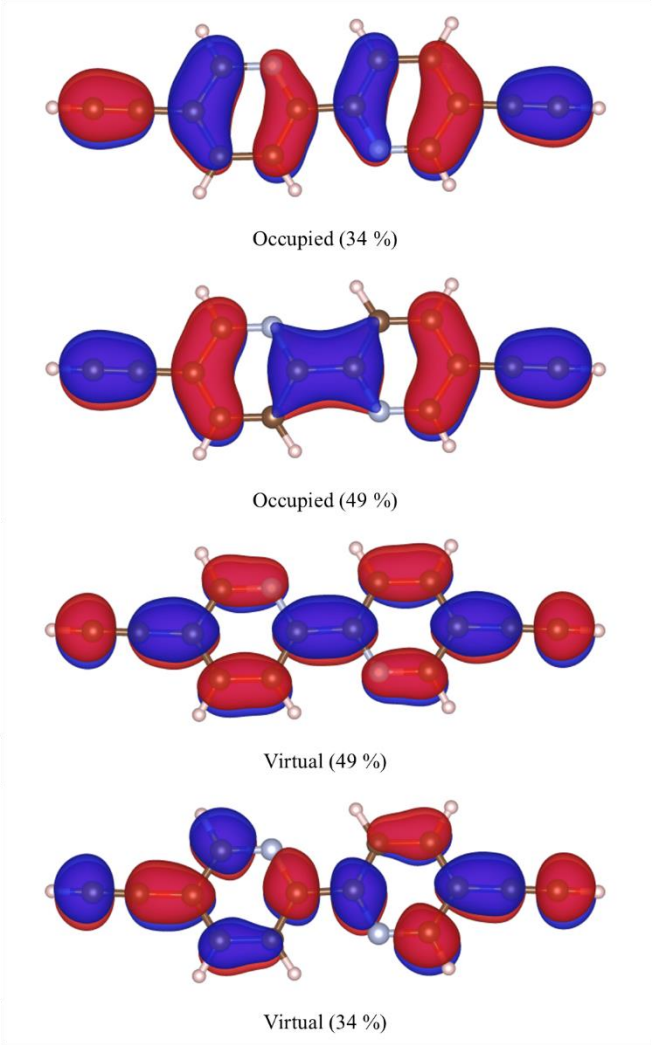

Figure S32 Natural transition orbitals (NTOs) for triplet excited state #2 in in the simulated spectrum of **1b** (λ = 364 nm), showing the occupied particle and virtual hole states associated with the electronic transition. The isosurface is drawn to a value of 2.5×10^{-2} *e* bohr^{-3}.

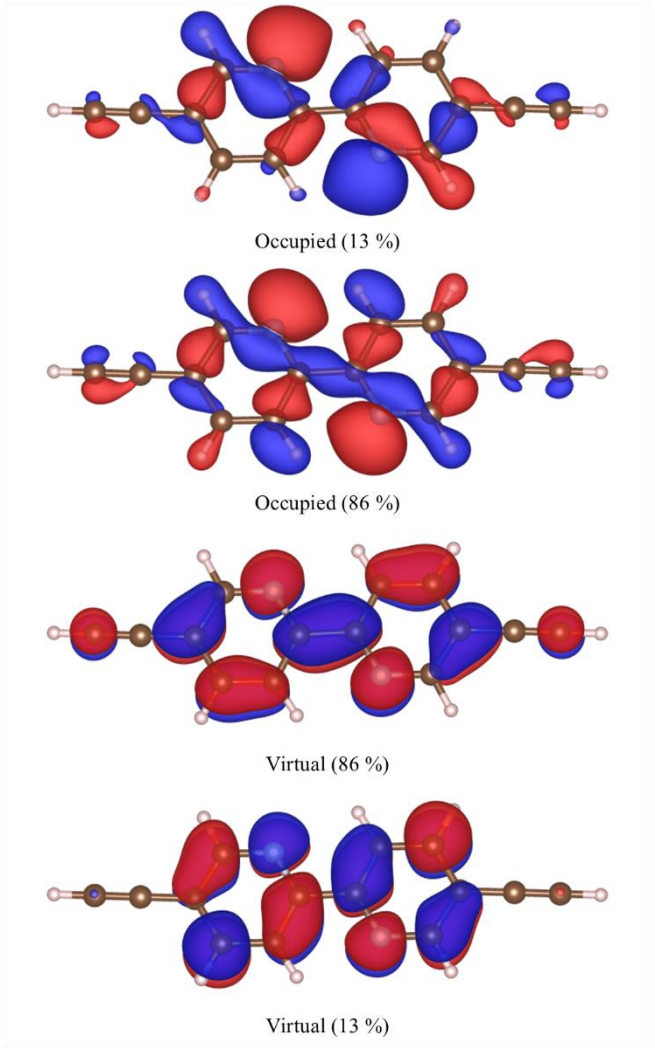

Figure S33 Natural transition orbitals (NTOs) for triplet excited state #3 in in the simulated spectrum of **1b** (λ = 305 nm), showing the occupied particle and virtual hole states associated with the electronic transition. The isosurface is drawn to a value of 2.5×10^{-2} *e* bohr^{-3}.

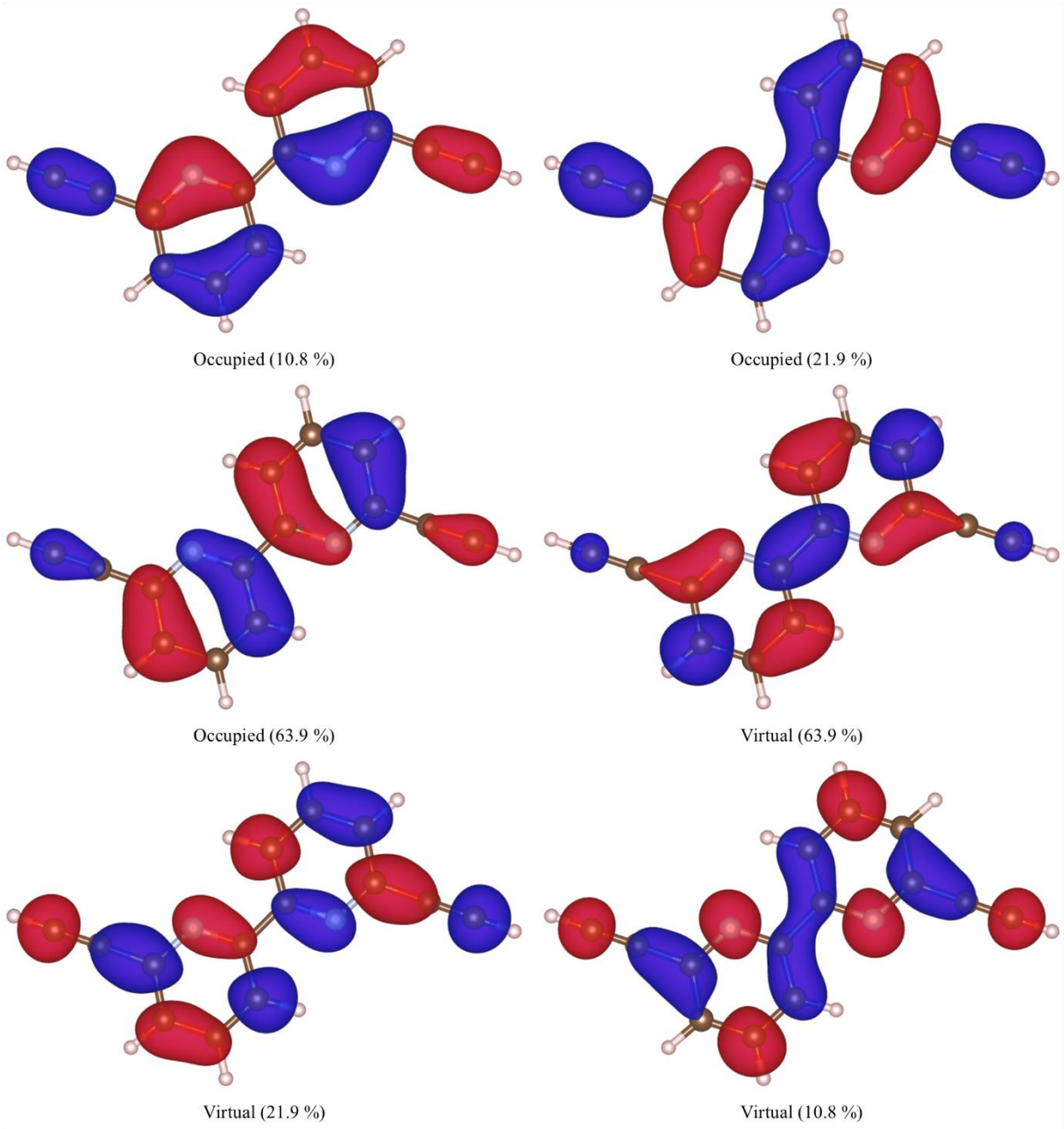

Figure S34 Natural transition orbitals (NTOs) for triplet excited state #1 in in the simulated spectrum of **2b** (λ = 426 nm), showing the occupied particle and virtual hole states associated with the electronic transition. The isosurface is drawn to a value of 2.5×10^{-2} *e* bohr^{-3}.

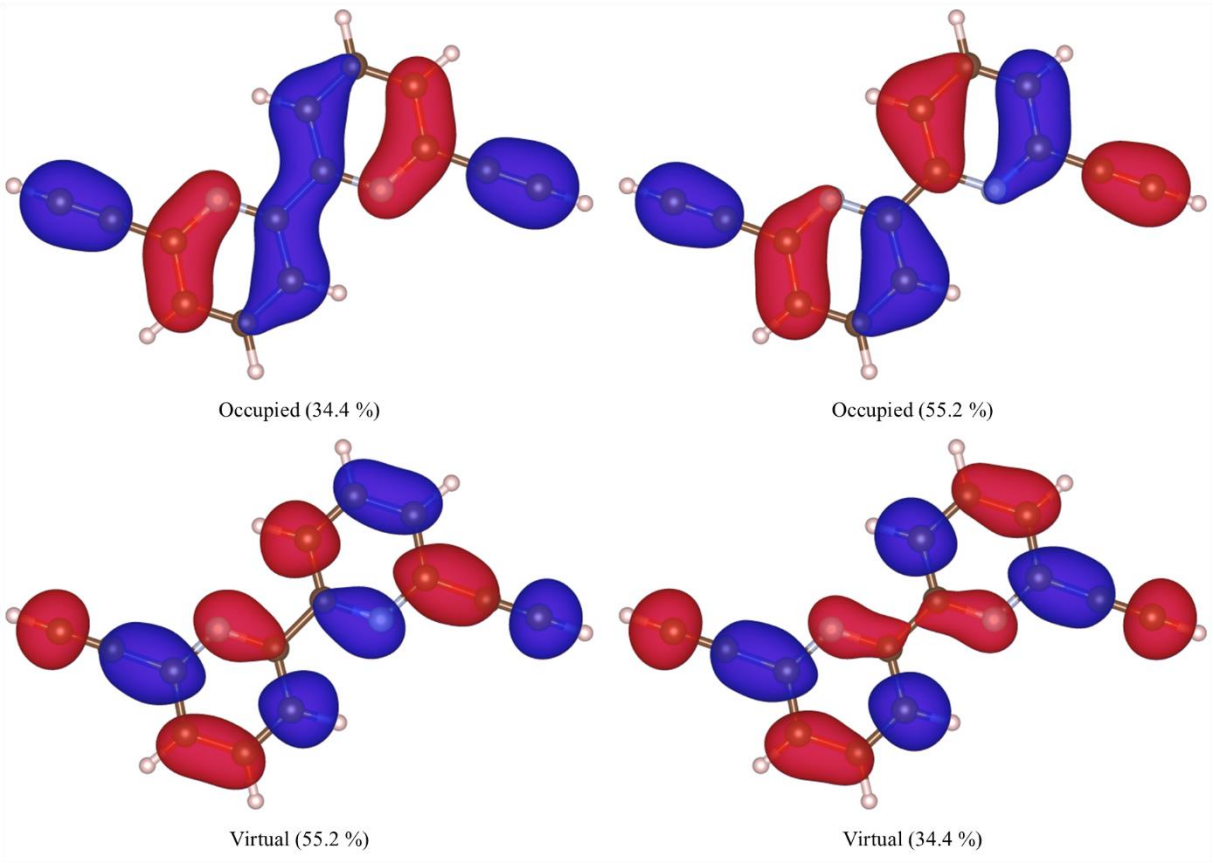

Figure S35 Natural transition orbitals (NTOs) for triplet excited state #2 in in the simulated spectrum of **2b** (λ = 374 nm), showing the occupied particle and virtual hole states associated with the electronic transition. The isosurface is drawn to a value of 2.5×10^{-2} *e* bohr^{-3}.

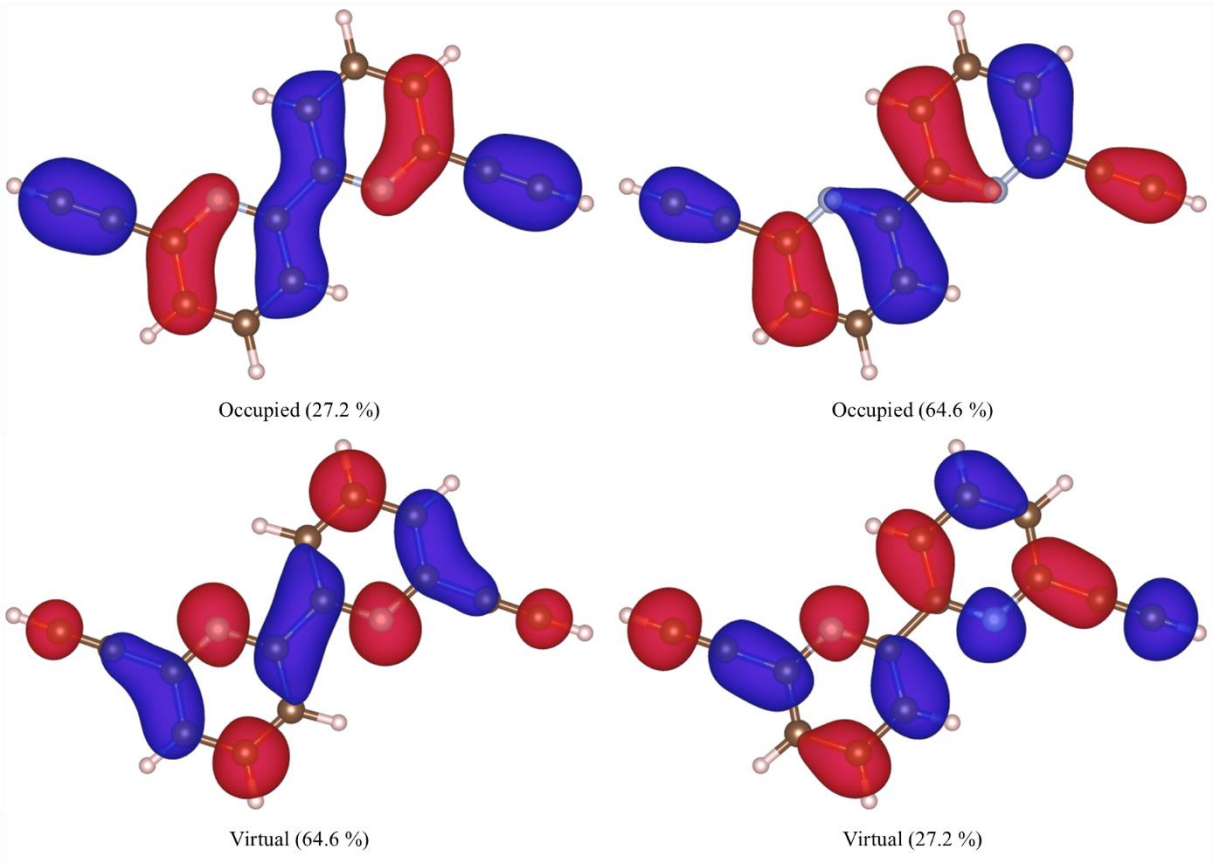

Figure S36 Natural transition orbitals (NTOs) for triplet excited state #3 in in the simulated spectrum of **2b** (λ = 320 nm), showing the occupied particle and virtual hole states associated with the electronic transition. The isosurface is drawn to a value of 2.5×10^{-2} *e* bohr^{-3}.

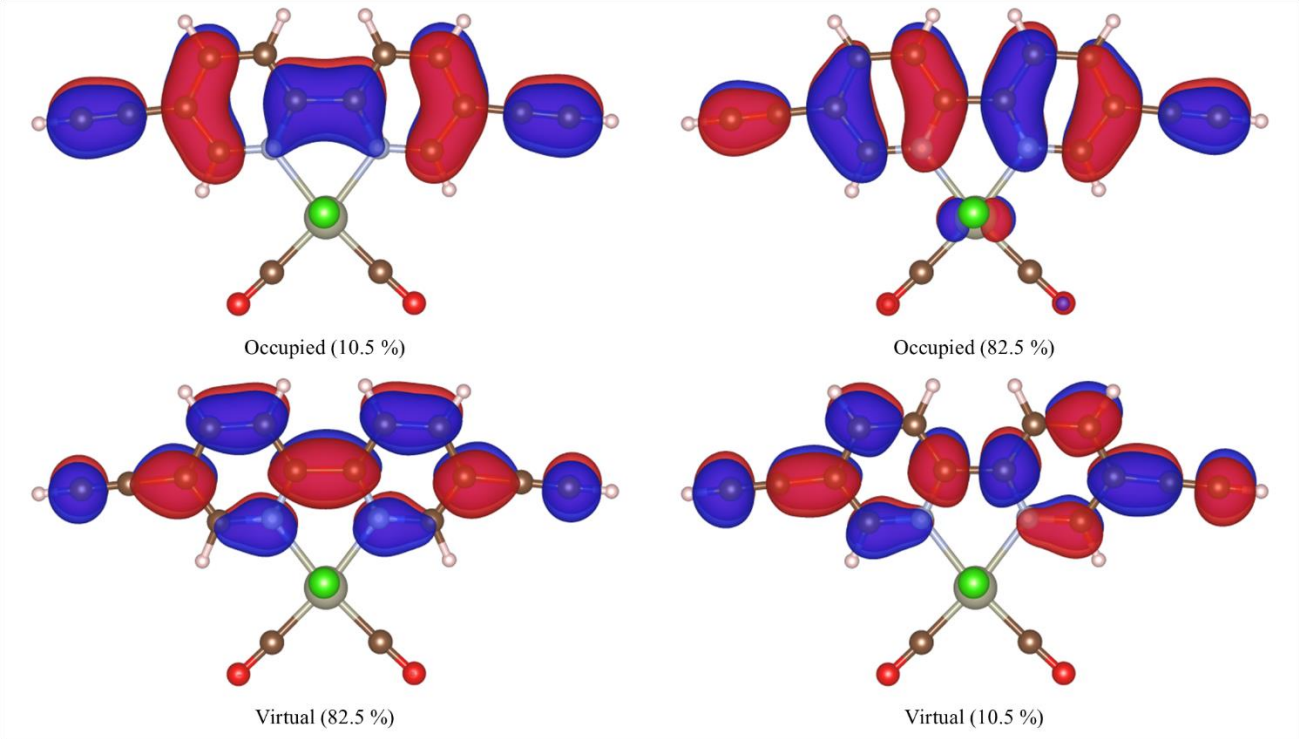

Figure S37 Natural transition orbitals (NTOs) for triplet excited state #1 in in the simulated spectrum of **1c** (λ = 492 nm), showing the occupied particle and virtual hole states associated with the electronic transition. The isosurface is drawn to a value of 2.5×10^{-2} *e* bohr^{-3}.

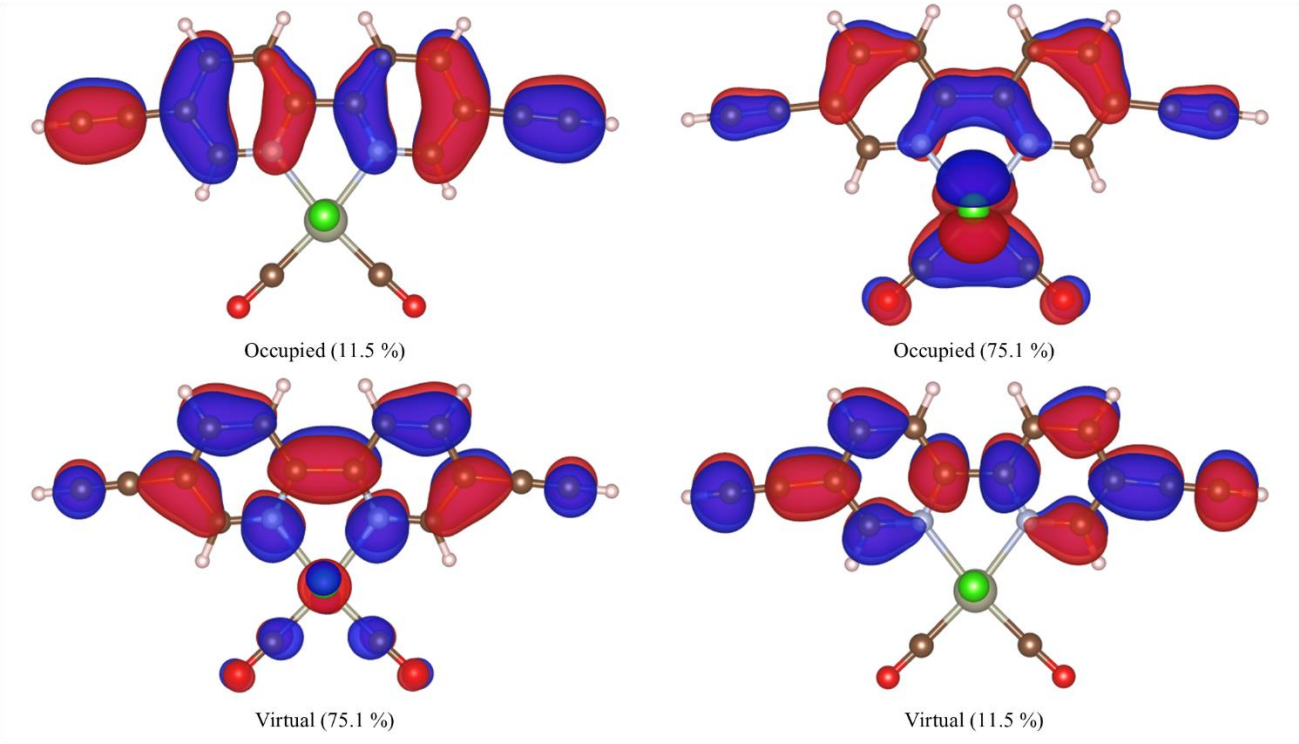

Figure S38 Natural transition orbitals (NTOs) for triplet excited state #2 in in the simulated spectrum of **1c** (λ = 391 nm), showing the occupied particle and virtual hole states associated with the electronic transition. The isosurface is drawn to a value of 2.5×10^{-2} *e* bohr^{-3}.

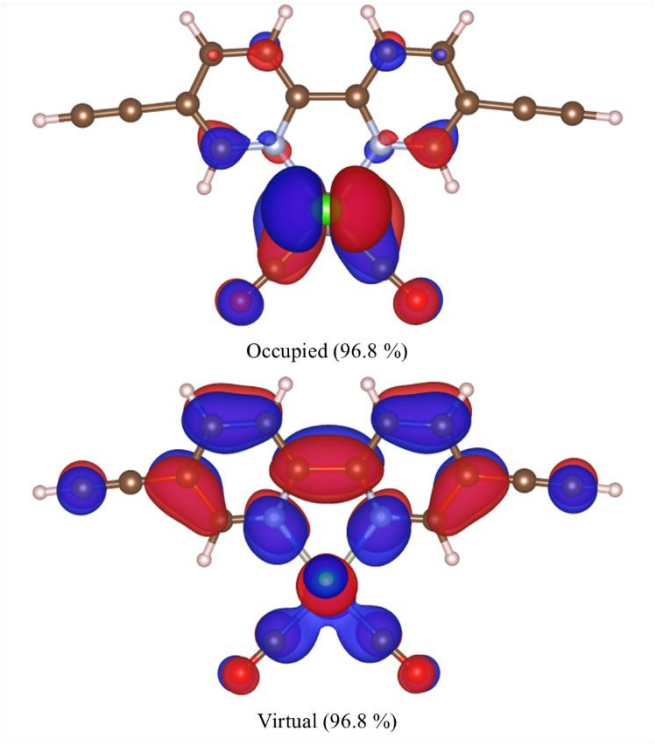

Figure S39 Natural transition orbitals (NTOs) for triplet excited state #3 in in the simulated spectrum of **1c** (λ = 377 nm), showing the occupied particle and virtual hole states associated with the electronic transition. The isosurface is drawn to a value of 2.5×10^{-2} *e* bohr^{-3}.

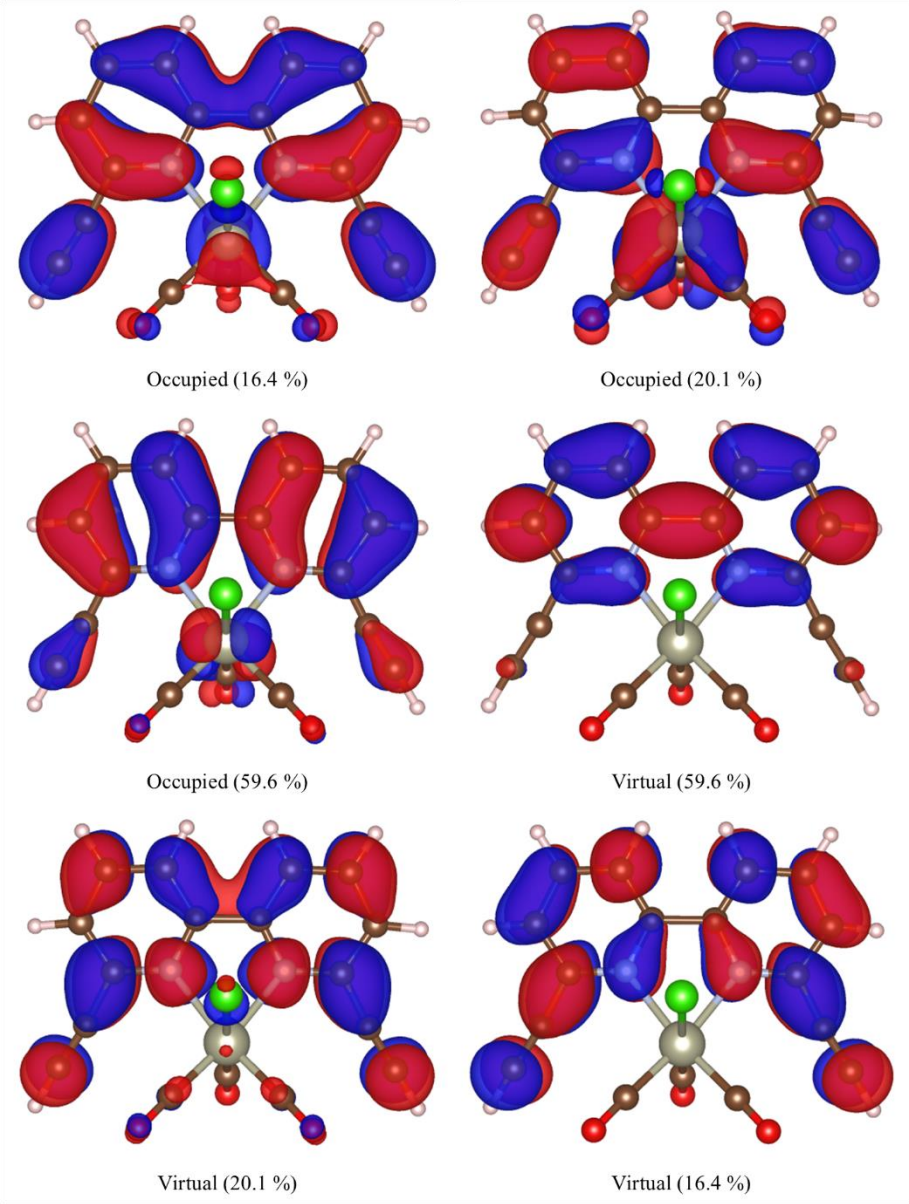

Figure S40 Natural transition orbitals (NTOs) for triplet excited state #1 in in the simulated spectrum of **2c** (λ = 443 nm), showing the occupied particle and virtual hole states associated with the electronic transition. The isosurface is drawn to a value of 2.5×10^{-2} *e* bohr^{-3}.

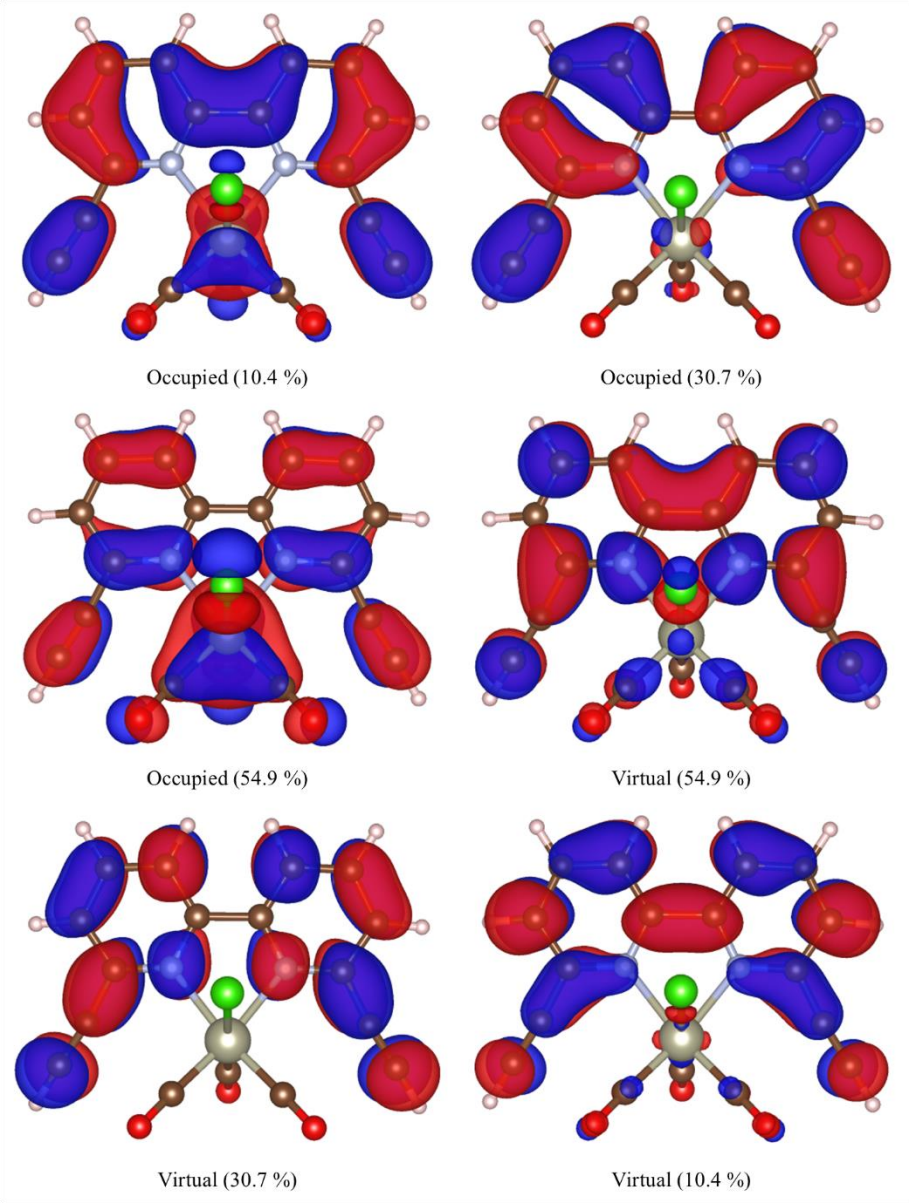

Figure S41 Natural transition orbitals (NTOs) for triplet excited state #2 in in the simulated spectrum of **2c** (λ = 402 nm), showing the occupied particle and virtual hole states associated with the electronic transition. The isosurface is drawn to a value of 2.5×10^{-2} *e* bohr^{-3}.

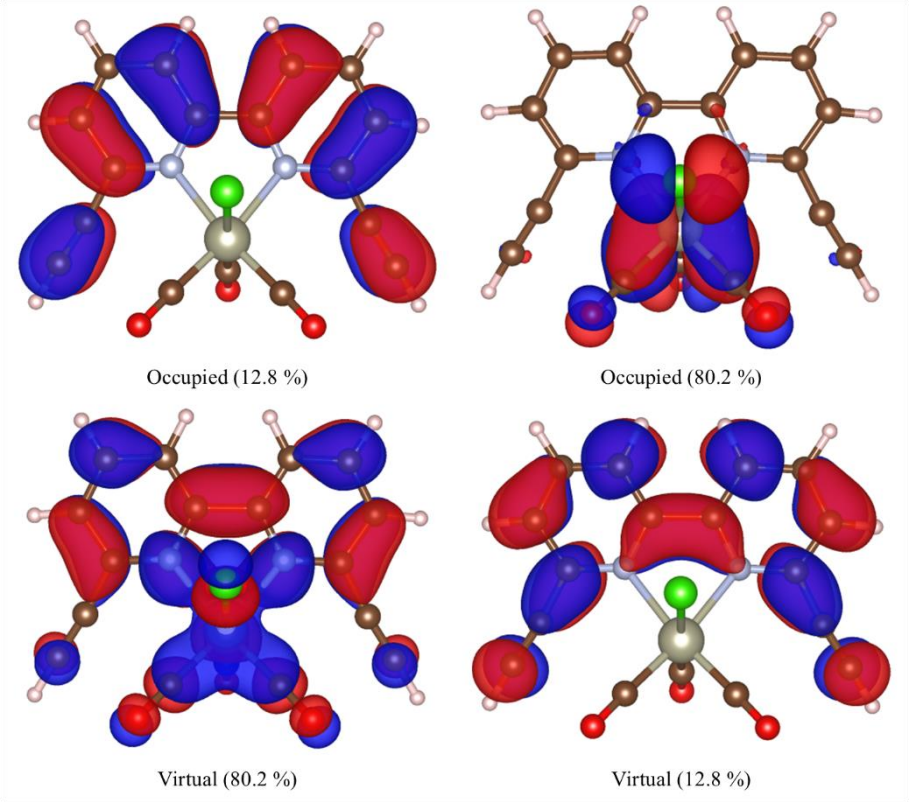

Figure S42 Natural transition orbitals (NTOs) for triplet excited state #3 in in the simulated spectrum of **2c** (λ = 374 nm), showing the occupied particle and virtual hole states associated with the electronic transition. The isosurface is drawn to a value of 2.5×10^{-2} *e* bohr^{-3}.

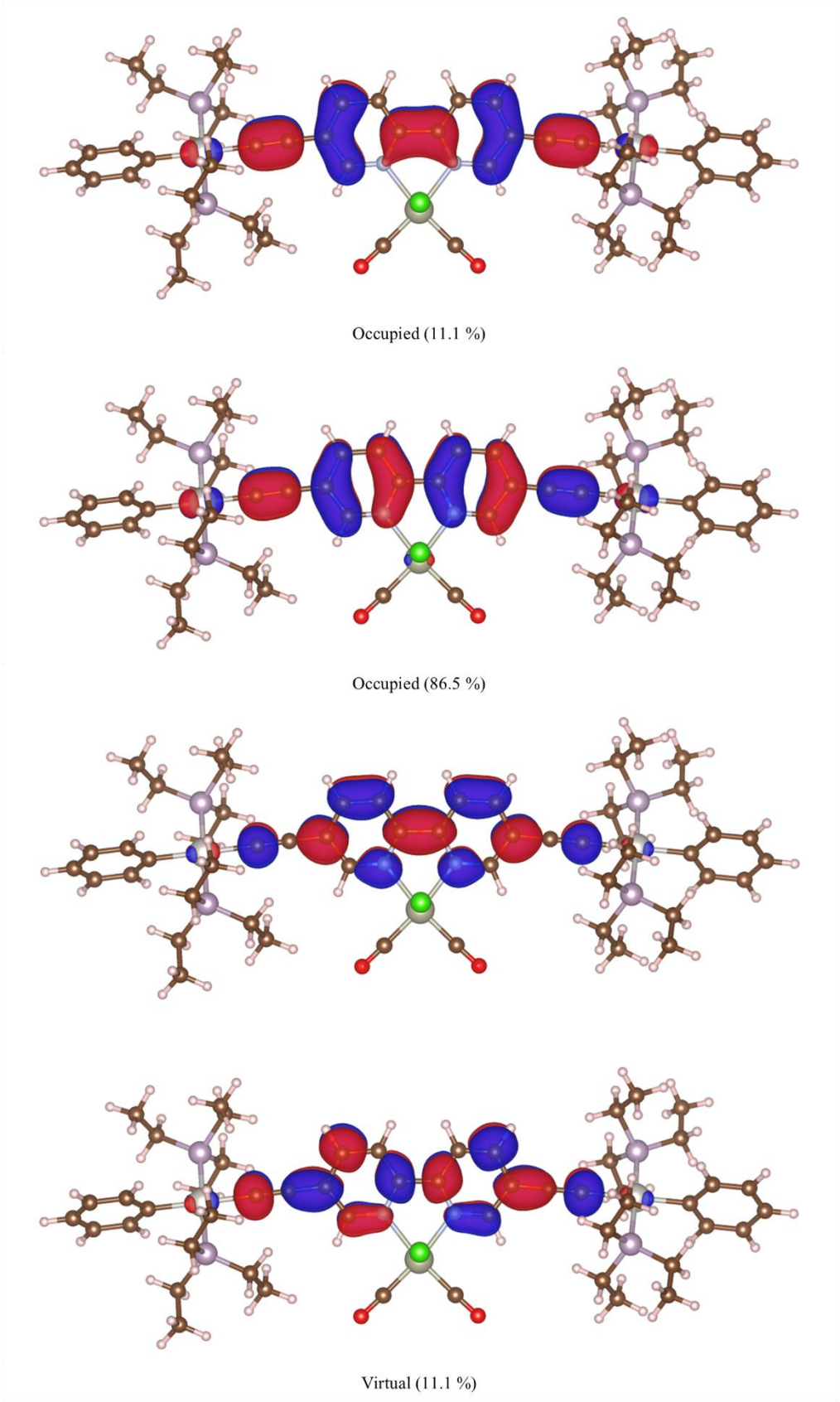

Figure S43 Natural transition orbitals (NTOs) for triplet excited state #1 in in the simulated spectrum of **M3** (λ = 550 nm), showing the occupied particle and virtual hole states associated with the electronic transition. The isosurface is drawn to a value of 2.5×10^{-2} *e* bohr^{-3}.

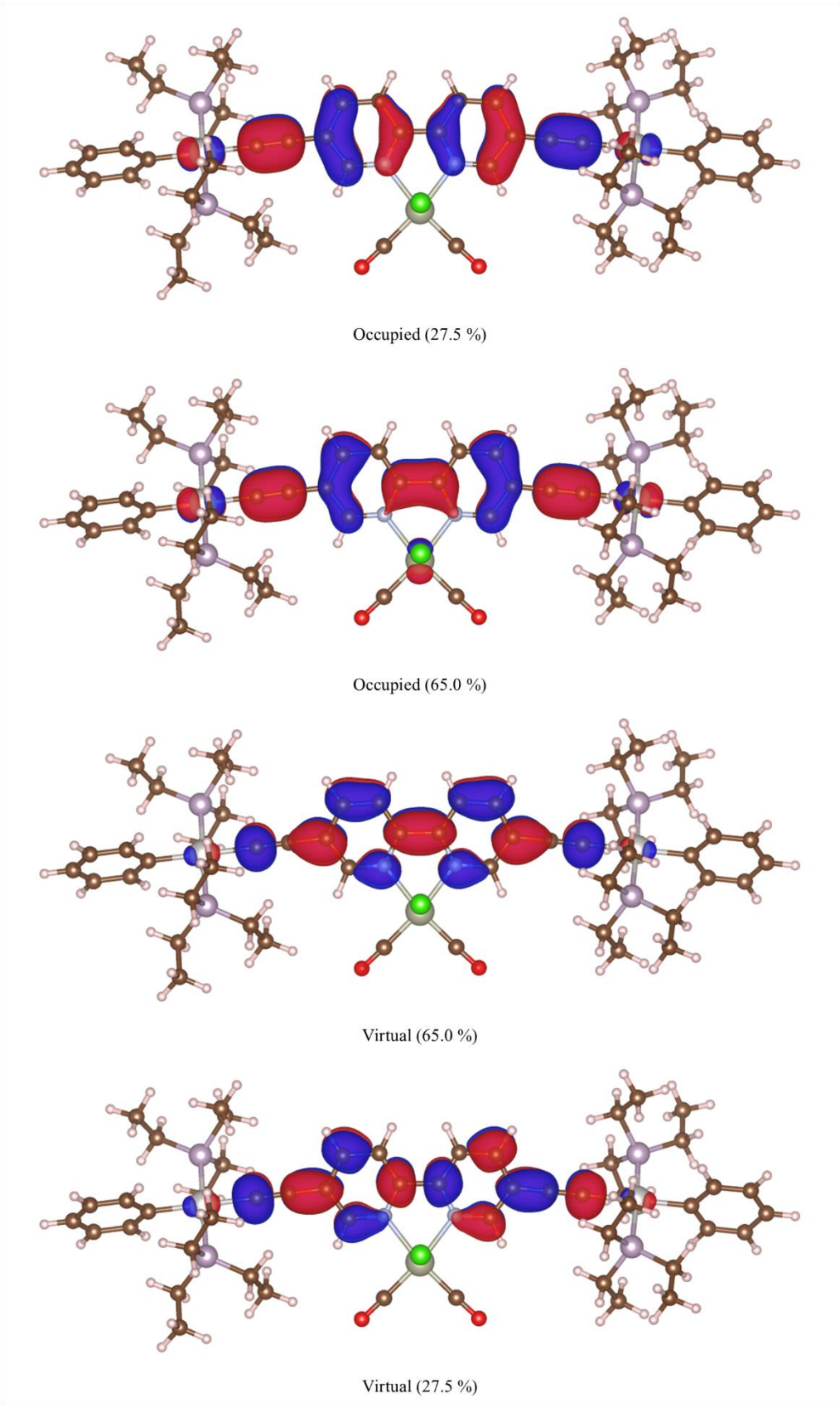

Figure S44 Natural transition orbitals (NTOs) for triplet excited state #2 in in the simulated spectrum of **M3** (λ = 417 nm), showing the occupied particle and virtual hole states associated with the electronic transition. The isosurface is drawn to a value of 2.5×10^{-2} *e* $bohr^{-3}$.

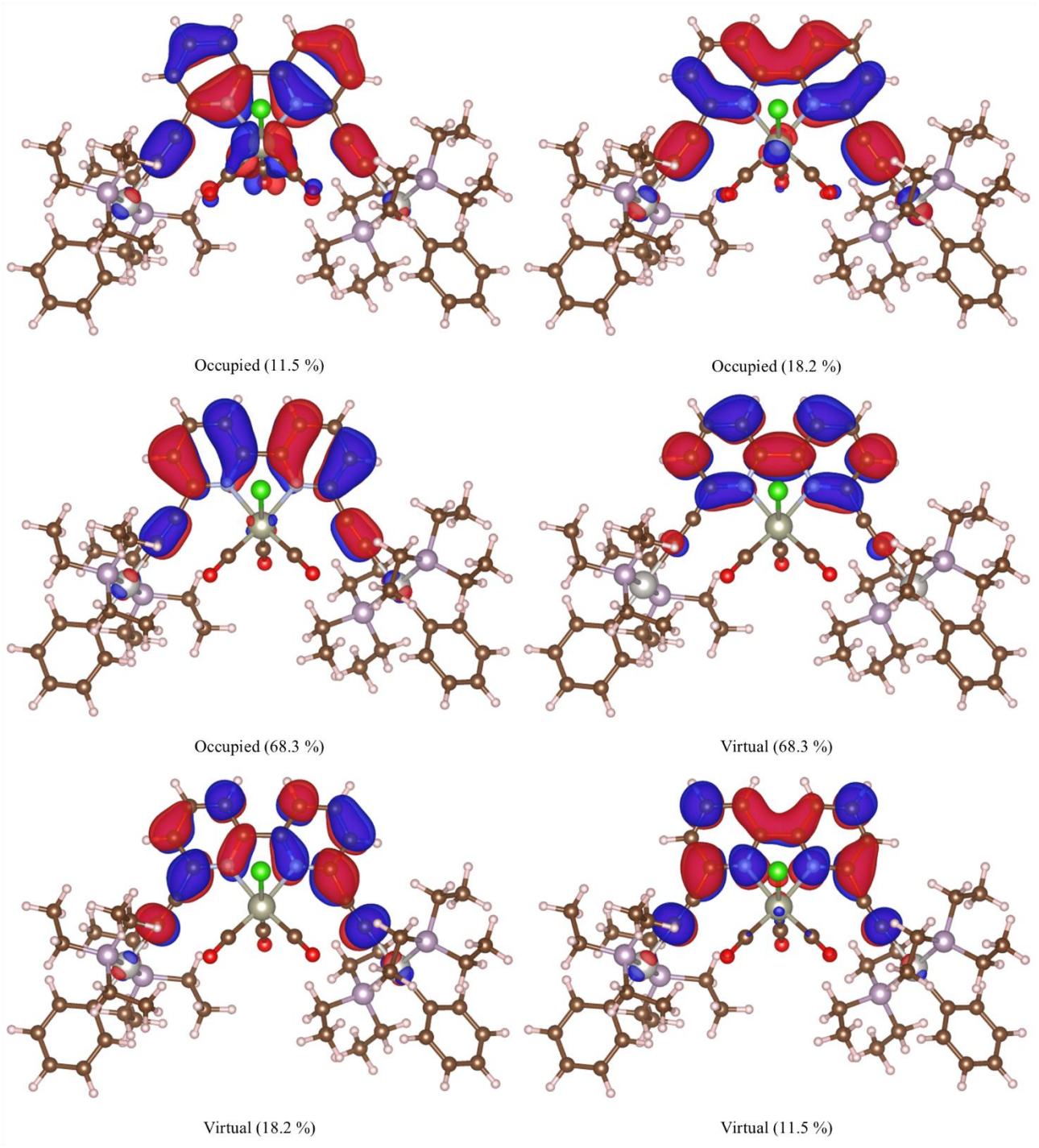

Figure S45 Natural transition orbitals (NTOs) for triplet excited state #1 in in the simulated spectrum of **M4** (λ = 466 nm), showing the occupied particle and virtual hole states associated with the electronic transition. The isosurface is drawn to a value of 2.5×10^{-2} *e* bohr^{-3}.

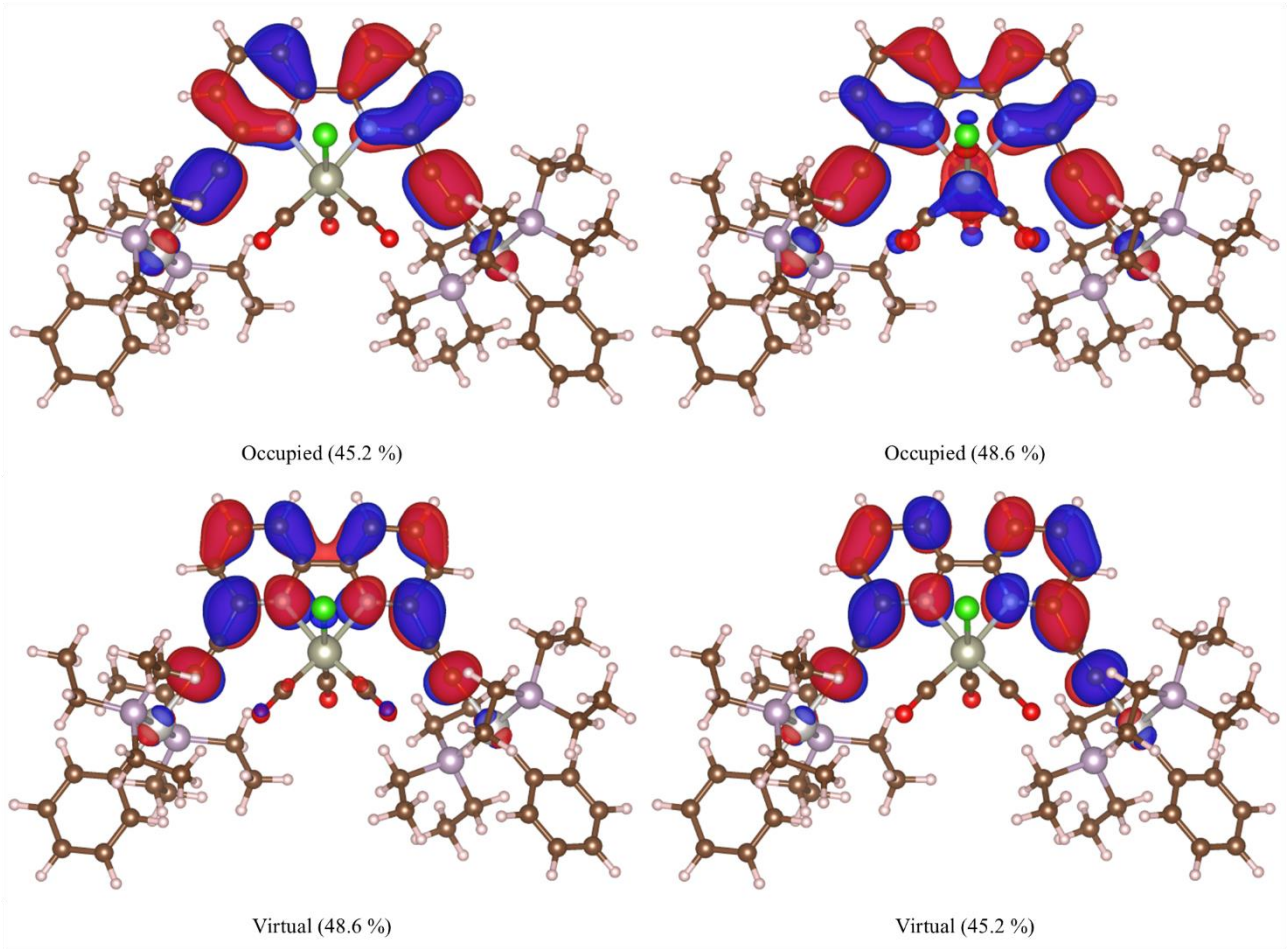

Figure S46 Natural transition orbitals (NTOs) for triplet excited state #2 in in the simulated spectrum of **M4** (λ = 423 nm), showing the occupied particle and virtual hole states associated with the electronic transition. The isosurface is drawn to a value of 2.5×10^{-2} *e* bohr^{-3}.

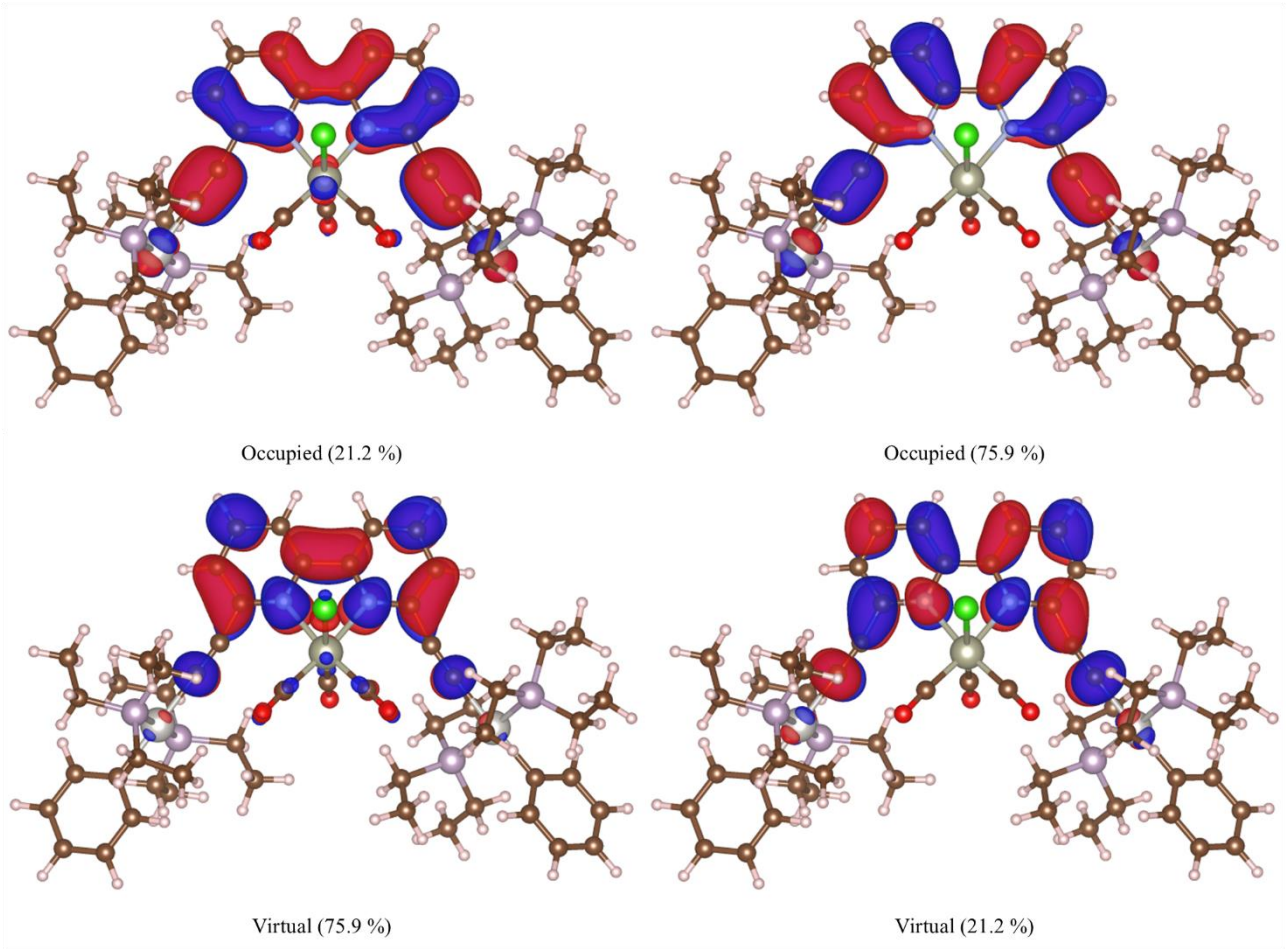

Figure S47 Natural transition orbitals (NTOs) for triplet excited state #3 in in the simulated spectrum of **M4** (λ = 409 nm), showing the occupied particle and virtual hole states associated with the electronic transition. The isosurface is drawn to a value of 2.5×10^{-2} *e* bohr^{-3}.